THE APPLICATION OF ACTIVE CONTROL IN RAILWAY PANTOGRAPHS

by

HUAYU DUAN

A thesis submitted to
The University of Birmingham
For the degree of
DOCTOR OF PHILOSOPHY

School of Engineering
The University of Birmingham
January 2023

UNIVERSITY OF
BIRMINGHAM

University of Birmingham Research Archive

e-theses repository

This unpublished thesis/dissertation is copyright of the author and/or third parties. The intellectual property rights of the author or third parties in respect of this work are as defined by The Copyright Designs and Patents Act 1988 or as modified by any successor legislation.

Any use made of information contained in this thesis/dissertation must be in accordance with that legislation and must be properly acknowledged. Further distribution or reproduction in any format is prohibited without the permission of the copyright holder.

ABSTRACT

Pantographs are essential elements of modern electric trains, coupling the train to the overhead electric lines in order to deliver a continuous supply of electrical energy to the vehicle. Undesired contact can cause excessive wear and poor train operation performance. In the worst case, this can eventually lead to dewirement incidents that can damage both the train and the overhead lines.

Pantographs in operation today, are essentially *passive* devices. However, *active* pantograph design has the potential to significantly improve the robustness of the pantograph–catenary interaction, in order to deliver a continuous power transmission for electric trains. However, it is found that the model-based controllers of current active pantograph research are not properly validated, whereas those that are tested in the laboratory are not designed based on the model. This thesis proposes a new and complete design and test approach for active pantographs following the typical model-based control design process.

A validated pantograph–catenary model and simulation framework are first developed, based on which a new (real-time-capable) disturbance-observer-based catenary model is proposed to improve the accuracy of active pantograph validation in simulation. It is advised that the proposed model should replace the classic time-varying lumped-mass catenary model in active pantograph validation.

A variety of control laws, ranging from the classic control methods to the state-of-the-art sliding mode control, are applied to the active pantograph design. The goal of designing a closed-loop pantograph system is to control the contact force by providing the measured contact force (i.e.,

output feedback), so as to make the contact force closer to the desired magnitude and thus reduce fluctuations. The active pantographs designed based on the linearised pantograph–catenary model have been demonstrated to be effective in reducing contact force fluctuation when validating with accurate catenary models.

Through the model-based active pantograph design approach, a novel frame-actuated active pantograph prototype (controlled by pneumatic pressure) is designed and tested with a hardware-in-the-loop experiment. The designed active pantograph in the laboratory can reduce the contact force fluctuation as expected at the design and simulation stages. It is recommended that more refined modelling approaches would be beneficial in delivering better control performance in the active pantograph.

ACKNOWLEDGEMENTS

I would like to express my deepest gratitude to thank my supervisors, Prof. Roger Dixon and Dr. Edward Stewart for their invaluable supervision, continuous support, and patience over the past four years. Their knowledge and experience have inspired and encouraged me in all the time of my study and daily life. Of course, without their dedicated involvement in every step throughout the process, this Ph.D. would have never been completed.

I would also like to thank Dr. Tingyu Xin, Dr. Paul Weston, Mr. Adnan Zentani and Mr. Sina Sharifi, for their generous support and guidance on this research. Special thanks to Prof. Yisheng Zhong at Tsinghua University for his inspiration and encouragement. I am also grateful to Prof. Felix Schmid for helping me with the Ph.D. application. I am deeply grateful to the examiners, Prof. Stephen Duncan and Dr. Yongjing Wang, for taking the time to read and examine my thesis. Your feedback and suggestions have been invaluable in improving the quality of my work. Thank you to all the academics who helped me throughout my student life.

I would also like to thank all friends and colleagues in BCRRE. It has been an amazing experience studying and working with you all.

Finally, but most importantly, I would like to thank my family for their great love, encouragement and understanding. I could not have reached this point without them.

TABLE OF CONTENTS

LIST OF FIGURES I

LIST OF TABLES V

LIST OF ABBREVIATIONS VII

CHAPTER 1 INTRODUCTION 1

1.1 Background 1

1.2 Motivation 5

1.3 Research hypothesis and objectives 6

1.4 Thesis contribution 7

1.5 Thesis structure 8

CHAPTER 2 LITERATURE REVIEW 10

2.1 Introduction 10

2.2 Pantograph–catenary modelling and simulation 11

2.2.1 Pantograph modelling 11

2.2.2 Catenary modelling 14

2.2.3 Contact (interaction) models 19

2.2.4 Summary of pantograph–catenary modelling 20

2.3 Active pantographs 25

2.4 Pantograph test rigs and hardware-in-the-loop (HIL) experiments 31

2.5 Summary and Conclusion 35

CHAPTER 3 PANTOGRAPH–CATENARY MODELLING AND SIMULATION 37

3.1 Introduction 37

3.2 Lumped-mass pantograph model 37

3.3 Finite Element-based catenary model 39

3.3.1 Wires 40

3.3.2 Wire suspensions 41

3.3.3 Droppers 42

3.3.4 Catenary geometry 42

3.3.5 Time integration 43

3.3.6 Summary of catenary modelling 44
3.4 Interaction method (contact model) 46
3.5 Simulation framework and workflow 46
3.5.1 Static simulation 47
3.5.2 dynamic simulation 52
3.6 Simulation validation 54
3.6.1 Static result 55
3.6.2 Dynamic result: double pantograph 57
3.6.3 Dynamic result: single pantograph 63
3.7 Summary and Conclusion 66

CHAPTER 4 DISTURBANCE-OBSERVER-BASED CATENARY MODEL FOR ACTIVE PANTOGRAPH VALIDATION 68
4.1 Introduction 68
4.2 Linear and classic time-varying lumped-mass catenary models 69
4.2.1 Linear catenary model for active pantograph design 69
4.2.2 Parameterisation of the linear catenary model 71
4.2.3 Classic time-varying catenary model for active pantograph validation 73
4.3 DO-based lumped-mass model 77
4.4 Evaluation of DO-based catenary in active pantograph validation 82
4.5 Summary and conclusion 87

CHAPTER 5 ACTIVE PANTOGRAPH DESIGN AND VALIDATION IN SIMULATION 89
5.1 Introduction 89
5.2 Loop shaping and phase-lead or lag compensator 90
5.3 Linear Quadratic Regulator 95
5.4 H-infinity optimal control 100
5.5 Disturbance rejection and disturbance-observer-based control 106
5.5.1 Introduction 106
5.5.2 Disturbance observer based sliding mode control 107
5.5.3 Controller validation 111
5.6 Summary and conclusions 114

CHAPTER 6 PANTOGRAPH–CATENARY HARDWARE-IN-THE-LOOP EXPERIMENT 116
6.1 Introduction 116
6.2 Test rig introduction 118
6.3 Pantograph identification by Frequency Response Function 121
6.4 The DO-based virtual catenary design 127
6.5 HIL design and validation 130
6.6 Active pantograph in HIL 137
6.7 Summary and conclusion 145

CHAPTER 7 CONCLUSIONS 147
7.1 Summary of the findings 147
7.2 Discussions and recommendations for future work 150

LIST OF REFERENCES 152

APPENDIX A THE FINITE ELEMENT MODELLING PROCEDURE FOR THE CATENARY WIRES 161

APPENDIX B ANALYSIS OF PANTOGRAPH–CATENARY SIMULATION PARAMETERS 165
B.1 FE meshing size 165
B.2 Steady arm stiffness 167
B.3 Simulation step size 169
B.4 Number of simulated spans and measured spans 170

APPENDIX C PUBLISHED PAPERS 176

LIST OF FIGURES

Figure 1.1.1. Pantograph working on the roof of a train 2

Figure 1.1.2. Cantilever hit by a pantograph (RAIB, 2013) 4

Figure 1.3.1. Model-based design process 7

Figure 2.2.1. Sideview of a typical pantograph 12

Figure 2.2.2. Pantograph lumped-mass models, from left to right: two-mass; three-mass; four-mass; five-mass 13

Figure 2.2.3. A typical catenary system 15

Figure 2.3.1. Block diagrams of typical active controls, top: feedback; bottom: feedforward 26

Figure 2.3.2. Placement of active actuators, from left to right: on the lower frame; in parallel with the head suspension; on the pantograph head directly 28

Figure 2.3.3. The models used in model-based active pantograph design and validation at different stages 30

Figure 2.4.1. Pantograph test bench built at Deutsche Bahn, Germany (Deml et al., 2001) 32

Figure 2.4.2. Pantograph HIL test rigs, from left to right: test rig in Chengdu, China (Zhang et al., 2002); test rig in Milan, Italy (Collina et al., 2004); test rig in Vienna, Austria (Schirrer et al., 2017) 34

Figure 3.2.1. Three-mass lumped-mass pantograph model 38

Figure 3.3.1. A typical pantograph–catenary system 40

Figure 3.5.1. Modelling of the detailed pantograph–catenary system 47

Figure 3.5.2. Workflow of assembling the components and finding initial conditions 48

Figure 3.5.3. Vertical displacement of the contact wire at steady state 50

Figure 3.5.4. Vertical displacement of the messenger wire at steady state 50

Figure 3.5.5. Vertical displacement of the contact wire under 95 N contact force 51

Figure 3.5.6. Overall dynamic simulation framework..... 53

Figure 3.5.7. Catenary dynamic simulation workflow 53

Figure 3.6.1. Static elasticity along a span when the imposed force is 169 N 56

Figure 3.6.2. Frequency response of the designed filter..... 59

Figure 3.6.3. Contact force for the leading pantograph..... 60

Figure 3.6.4. Contact force for the trailing pantograph..... 61

Figure 3.6.5. Contact wire displacement for the leading pantograph..... 61

Figure 3.6.6. Contact wire displacement for the trailing pantograph 62

Figure 3.6.7. Contact wire uplift at the 6th mast 62

Figure 3.6.8. Contact force for the single-pantograph case..... 64

Figure 3.6.9. Contact wire displacement for the single-pantograph case..... 64

Figure 3.6.10. Contact wire uplift at the 6th mast for the single-pantograph case..... 65

Figure 4.2.1. Linear pantograph–catenary model..... 70

Figure 4.2.2. Relative displacement of contact wire with FE and estimated catenary models 73

Figure 4.2.3. Static elasticity along a span when the imposed force is 95 N 74

Figure 4.2.4. Height variation of the FE catenary model (pre-sag)..... 75

Figure 4.2.5. Spatially varying offset force against the gradient change 76

Figure 4.2.6. Contact force result of the classic model 77

Figure 4.3.1. Obtained disturbance signal 80

Figure 4.3.2. Workflow of DO-based catenary development..... 81

Figure 4.3.3. Contact force result of the DO model 81

Figure 4.4.1. Block diagram for the pantograph–catenary closed-loop system 83

Figure 4.4.2. Step response of the closed-loop system..... 84

Figure 4.4.3. Control output - PID active pantograph with catenary models 85

Figure 4.4.4. Control input - PID active pantograph with catenary models 85

Figure 5.2.1. Disturbance rejection performance of passive and active pantographs 93

Figure 5.2.2. Control output - phase-lag active pantograph with catenary models 94

Figure 5.2.3. Control input - phase-lag active pantograph with catenary models 94

Figure 5.3.1. Structure of LQR plus output integral 97

Figure 5.3.2. Control output - LQR-integral active pantograph with catenary models 98

Figure 5.3.3. Control input - LQR-integral active pantograph with catenary models 99

Figure 5.3.4. Contact wire displacement comparison between real and observed states 100

Figure 5.4.1. Augmented closed-loop plant for H-infinity design 101

Figure 5.4.2. Frequency-dependent weight for the output y 103

Figure 5.4.3. Control output - H-infinity active pantograph with catenary models 104

Figure 5.4.4. Control input - H-infinity active pantograph with catenary models 104

Figure 5.4.5. Disturbance response comparison between open loop and closed loop 105

Figure 5.5.1. Control output - DO-SMC active pantograph with catenary models 113

Figure 5.5.2. Control input - DO-SMC active pantograph with catenary models 113

Figure 6.1.1. Overview of the active pantograph HIL test system 118

Figure 6.2.1. The three entities of the test rig 119

Figure 6.2.2. Collapsed pantograph under the test rig frame 119

Figure 6.2.3. The pantograph in normal contact with the test rig frame 120

Figure 6.3.1. FRF input and output under 10 Hz contact bar movement 122

Figure 6.3.2. Nominal pantograph working height 123

Figure 6.3.3. FRF of the physical pantograph (force-to-head-acceleration) 124

Figure 6.3.4. Error costs of the optimised results with the 100 initial parameter sets 127

Figure 6.3.5. Comparison between optimised and reference results 127

Figure 6.4.1. Contact force in the simulation with the identified pantograph model 128

Figure 6.4.2. Contact wire displacement with the identified pantograph model 129

Figure 6.4.3. Contact wire relative displacement with FE and estimated catenary models ... 130

Figure 6.4.4. Estimated lumped disturbance 130

Figure 6.5.1. HIL control command flow 131

Figure 6.5.2. HIL validation: without-a-pantograph 134

Figure 6.5.3. Without-a-pantograph displacement result 135

Figure 6.5.4. HIL validation: with-a-pantograph 136

Figure 6.5.5. With-a-pantograph displacement result 136

Figure 6.5.6. With-a-pantograph contact force result 137

Figure 6.6.1. Schematic of flow of compressed air 138

Figure 6.6.2. Flow of compressed air 138

Figure 6.6.3. The open-loop system 140

Figure 6.6.4. Data for plant identification 141

Figure 6.6.5. Distribution of model error 141

Figure 6.6.6. Frequency response of the estimated model 142

Figure 6.6.7. Disturbance rejection performance of the closed-loop system 143

Figure 6.6.8. Contact force of the active pantograph in HIL 144

Figure 6.6.9. Contact force spectrum of the active pantograph in HIL 144

Figure A.1. Euler–Bernoulli beam element 161

Figure B.1.1. Contact force results with the two meshing sizes 166

Figure B.2.1. Static stiffness results with the three steady arm stiffnesses 167

Figure B.2.2. Contact force results with the three steady arm stiffnesses 168

Figure B.3.1. Contact force results with the three simulation step sizes 170

Figure B.4.1. Contact force results with 8-, 10- and 12-span cases 172

Figure B.4.2. Contact force results measured from 3rd and 7th span cases (spectrum)..... 173

Figure B.4.3. The time history of the uplift of a steady arm 174

LIST OF TABLES

Table 2.2.1. Summary of modelling methods applied in simulation codes.....22

Table 2.3.1. Summary of active pantograph designs from the literature.....28

Table 3.2.1. Parameters of the three-mass model.....38

Table 3.3.1. Parameters of the wires 45

Table 3.3.2. Parameters of the droppers, suspensions and catenary geometry.....45

Table 3.5.1. Dropper force at steady state 49

Table 3.5.2. Steady states of the pantograph model for ensuring a 95 N contact force 52

Table 3.6.1. Static result validation against EN 50318:2018 57

Table 3.6.2. Dynamic result validation against EN 50318:2018.....63

Table 3.6.3. Single-pantograph dynamic result compared with the benchmark 66

Table 4.2.1. Constraint and result of parameter identification for a running condition 73

Table 4.2.2. Numerical result of the classic model 77

Table 4.3.1. Numerical result of the DO model 82

Table 4.4.1. Dynamic result of the DO model.....84

Table 4.4.2. Accuracy comparison between the two catenary models.....85

Table 4.4.3. Numerical results of the PID active pantograph.....86

Table 5.2.1. Numerical results of the phase-lag active pantograph.....95

Table 5.3.1. Numerical results of the LQR-integral active pantograph 99

Table 5.4.1. Numerical results of the H-infinity active pantograph.....105

Table 5.5.1. Numerical results of the DO-SMC active pantograph 113

Table 6.3.1. Ranges of sampled initial parameters and results 126

Table 6.4.1. Parameterisation constraint and result for the HIL virtual catenary.....129

Table 6.5.1. Summary of HIL parameters 133

Table 6.6.1. Metrics of the contact force with the active pantograph 145

Table B.1.1. Numerical results with the two meshing sizes 166

Table B.2.1. Numerical results with the three steady arm stiffnesses 169

Table B.3.1. Numerical results with the three simulation step sizes 170

Table B.4.1. Contact force results with 8-, 10- and 12-span cases 172

Table B.4.2. Contact force results measured from 3rd and 7th span cases 173

LIST OF ABBREVIATIONS

ARX	Autoregressive with Extra Input model
cRIO	NI-CompactRIO
DO	Disturbance observer
DO-SMC	Disturbance-observer-based sliding mode control
EN	European Norm
FDM	Finite difference method
FE	Finite element
FEM	Finite element method
FIFO	First-in-first-out
FRF	Frequency response function
HIL	Hardware-in-the-loop
LQR	Linear quadratic regulator
PID	Proportional–integral–derivative
SMC	Sliding mode control
UoB	University of Birmingham
VSC	Variable structure control

CHAPTER 1 INTRODUCTION

1.1 Background

The railway plays a vital role in public service, and it often becomes the economic lifeline of a region. Compared to other modes of transport, the railway is characterised by high cargo capacity and safety. People tend to travel by train not only for intercity trips but also for daily commuting. Besides the need for capacity, there are increasing demands on transport in terms of reliability and sustainability (RSSB, 2012). Therefore, electric trains have been widely developed because of their high energy efficiency and capability to use renewable energy sources.

The proportion of electrified railways has been gradually increasing around the world. From 2000 to 2022, the share of electrified lines improved from 29% to 41% worldwide, while in Europe and Great Britain this number went up from 47% to 54% and from 30% to 38%, respectively (UIC, 2022). One of the positive outcomes in the railway sector is that between 2005 and 2015, CO_2 emissions per passenger-kilometre decreased by 27.8%, and CO_2 per freight tonne-kilometre decreased by 19.0% (UIC and IEA, 2017).

Running an electric train relies on collecting current from the power supply conductor. Basically, there are two primary forms of current transmission in the railway: collecting from the third rail by shoegear or from the overhead line (also known as catenary) by pantograph. Compared to that from the third rail, energy transmission from overhead lines through pantographs has a more stable vehicle–conductor interaction behaviour, which is essential to high-speed services that are supplied by AC voltage (Rahman et al., 2020). Also, the third rail needs more maintenance, especially under unfavourable weather conditions. In addition, the

third rail may be hazardous for people who are unaware of the danger of trespassing on the railway. Consequently, in Britain, around two-thirds of the electrified routes are equipped with overhead lines (Butcher, 2017). On these routes, such as that shown in Figure 2.2.3, pantographs play a vital role in the operation of electric train services.



Figure 1.1.1. Pantograph working on the roof of a train

The high quality of the current collection for an electric train is realised via uninterrupted mechanical contact between conductors. The contact between the pantograph head and the contact wire is supposed to be continuous, which is achieved by a steady flow of compressed air supplied to pneumatic system that holds up pantograph. However, the pantograph–catenary contact forms a coupled oscillation system when the train moves.

From the perspective of the cross-section along the track, the pantograph–catenary contact point fluctuates vertically due to changes of the contact wire conditions (such as wire height and impact of wave reflection), which leads to a variation in the contact force.

A positive contact force ensures that contact is maintained, between pantograph and catenary. If the contact force reduces to zero this results in a loss of contact (i.e., the physical

disconnection between the pantograph and the catenary) which disrupts the supply of power to the train. This loss of contact may also result in electrical arcing, which can cause damage to the pantograph (e.g., rapid wear of the carbon strip) and overhead line equipment. In some cases the train may have to reduce its speed or come to a halt, which can cause delays for passengers and disrupt the train schedule.

If the contact force is too high, it can cause the pantograph to press too hard against the overhead contact wire, leading to increased friction and wear on both surfaces. This can cause damage to the pantograph, such as deformation or cracks in the carbon strips. Similarly, the repeated high-pressure contact between the pantograph and the catenary wire may cause the wire to deform, expand, contract.

Therefore, managing the contact force between the pantograph and catenary is important to ensure that the surfaces of both components are not subjected to excessive wear and tear, which can result in equipment failure and increased maintenance costs. Over the financial years 2007/08–2011/12, the total delay minute compensation on the British mainline due to electrification issues was £75.4M, ranking 5th out of the total of 12 asset types (Bemment et al., 2018). For example, one such critical incident happened in Cambridgeshire on 5th January 2012 where a pantograph dewired (due to the misalignment of the pantograph and the catenary) and hit the cantilever (the structure for suspending the overhead lines), as shown in Figure 1.1.2. The pantograph then fell down from the vehicle roof and approximately 150 metres of catenary was damaged. This suspended operation of the railway line for the rest of that day (RAIB, 2013).



Figure 1.1.2. Cantilever hit by a pantograph (RAIB, 2013)

A report (Evans et al., 1990) indicated that the dewirement of pantographs typically occurs 80 times per year in Britain. Events like this, where pantographs can pull down a section of wire are generally caused by misalignment of the pantograph and/or the overhead line equipment. The average direct cost of each incident was estimated to be £20,000 and the total cost of a serious incident can be up to £250,000. Although the magnitude of pantograph–catenary contact force is not considered to be the main reason for the pantograph dewirement, it has been identified in the report as a contributing factor in determining the possibility of dewirement, considering the long-term impact of extreme values of contact force on the structure of the catenary.

With an increase in train running speed, the pantograph–catenary interaction becomes more critical and vulnerable (Ambrósio et al., 2012b). In the industrial technical criteria for the pantograph–catenary interaction (BSI, 2012), the upper allowance of the contact force for high-speed trains is higher than for slow lines, and therefore a more frequent maintenance routine for the overhead line equipment and pantographs is needed to ensure mechanical abrasion can be managed in a timely fashion. Researchers have also pointed out that the pantograph–catenary

interaction becomes one of the technical bottlenecks to expanding the high-speed train network (Yang et al., 2017).

1.2 Motivation

A pantograph typically relies upon an open-loop mechanism to perform its daily functions. A 'passive' pantograph is usually driven by compressed air with a constant pressure, which cannot effectively absorb the system's internal (e.g., the variation of catenary property) or external (e.g., wind) changes and interference. As it is known that the pantograph–catenary system poses hazards to railway operation, application of control engineering has been considered to achieve automatic control in pantographs, as so-called 'active pantographs'. By designing and constructing closed-loop control methods and actuation devices, the pantograph system is designed to react to the disturbances robustly, which can not only enhance the dynamic interaction between overhead lines and pantographs, but also solve railway interoperability issues.

However, despite the work by researchers to investigate active pantographs, it is found that many active pantographs are validated with simple lumped-mass catenary models, which were challenged on whether they could deliver authentic results. For those validated with accurate catenary models, most of them use proportional–integral–derivative (PID) controller but are not tuned based on a mathematical model of the pantograph–catenary system. Furthermore, only a very limited number of active pantograph prototypes have been built in the laboratory, and none of their controllers were designed model-based. It is surmised that the model-based controllers of current active pantograph research are not properly validated, whereas those that are tested in the laboratory are not designed based on the model. Therefore, it is worthwhile to study the

application of active control in railway pantographs through a complete model-based design process.

1.3 Research hypothesis and objectives

This thesis is conducted in response to the following research hypothesis: Pantograph–catenary mechanical contact performance can be improved using active control strategies applied to pantographs through model-based design workflow.

To apply an active control strategy to a system based on its model, there is a multi-step process in practice. Nonlinear and sometimes complex dynamics models are often constructed to represent closely the behaviour of real-world systems. These models are usually then simplified and linearised in order to allow the application of control design methods (most of which rely on a linear model). The performance of the closed-loop controller is designed and tuned on the linear model until satisfactory performance is obtained. The performance of the controller is then evaluated on the complex simulation model and on a real system in a laboratory environment prior to testing in the real situation.

The thesis will start with a literature review. A detailed pantograph–catenary model and its simulation framework will be constructed, which will serve as a source of truth for the pantograph–catenary interaction behaviour. In order to design and validate model-based active pantographs in simulation, the detailed catenary model to be studied will be transformed into a linear and a nonlinear lumped-mass models. Based on the lumped-mass models, the active pantograph will then be designed and tested in simulation with a variety of control methods, ranging from classical to state-of-the-art advanced control laws, although some of them might be not feasible considering the capability of physical closed-loop designs. One of the control

approaches will be implemented on a physical pantograph whose control effectiveness will be demonstrated by interaction with a virtual catenary by means of a hardware-in-the-loop experiment.

The model-based design process for the development of active pantographs (and the related chapter in this thesis) is depicted in Figure 1.3.1.

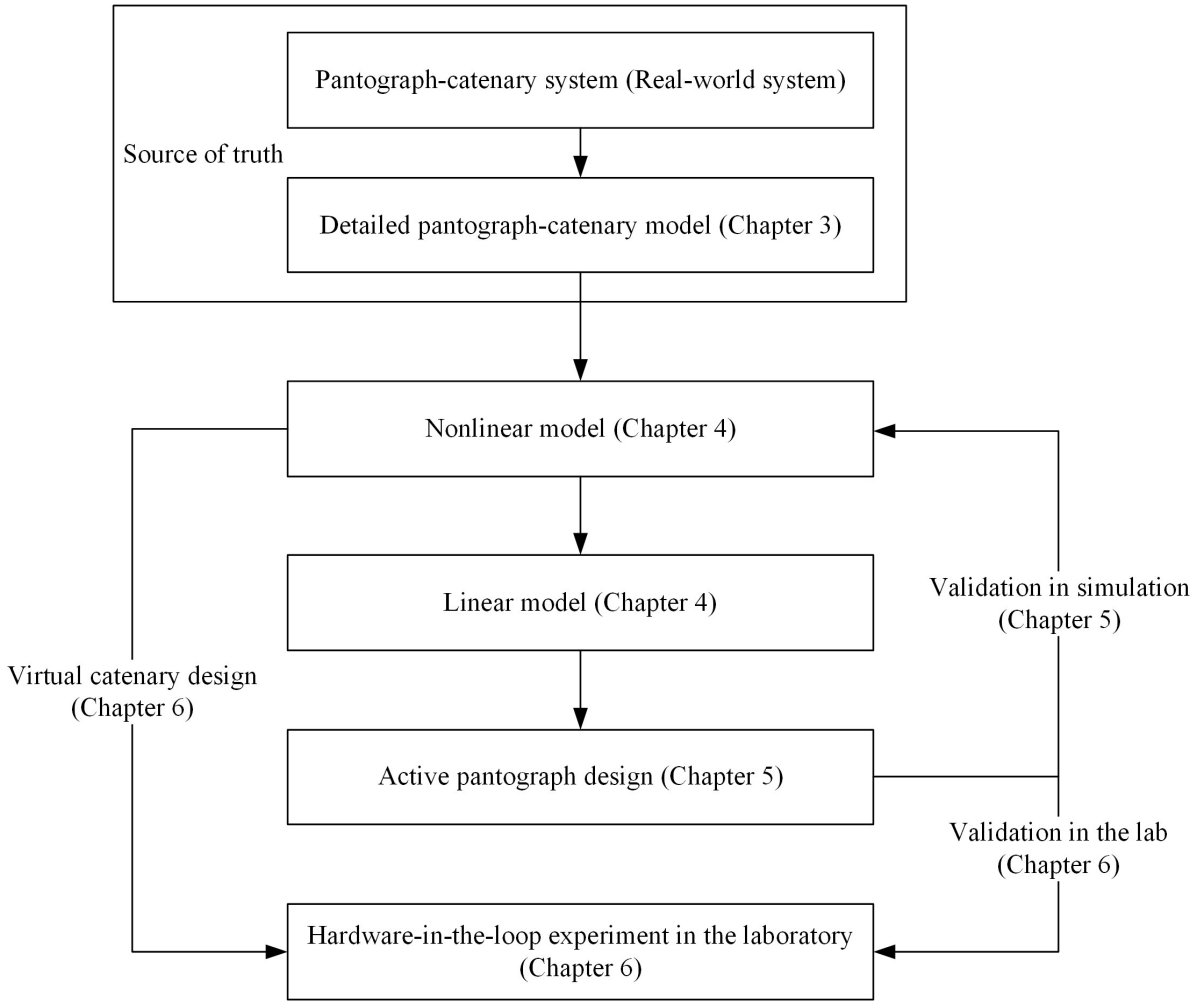


Figure 1.3.1. Model-based design process

1.4 Thesis contribution

This thesis proposes a new and complete design and test approach for active pantograph. The approach follows the typical model-based control design process, which includes system

modelling, controller design, and validation (Gevers et al., 2003, Hou and Wang, 2013). It is suggested that this approach could be employed by researchers and engineers for active pantograph designs.

To improve the veracity of the active pantograph validation in simulation, a novel disturbance-observer-based catenary model is proposed. This model is shown to be an accurate and real-time capable approach for passive and active pantograph simulations.

Based on the mathematical model of pantograph–catenary system, a variety of control laws are applied to the design of active pantograph. It is demonstrated that the model-based active pantograph is effective in reducing the fluctuations in contact force when validating with accurate catenary models in simulation.

Through the model-based design process, a novel frame-actuated active pantograph is designed and tested with a hardware-in-the-loop environment in the laboratory. The prototype has been demonstrated to be effective in reducing contact force fluctuation as expected at the design stage.

1.5 Thesis structure

Chapter 1 outlines the background, motivation, hypothesis, objective and contribution of this thesis.

Chapter 2 reviews the literature regarding pantograph–catenary modelling and simulation, active pantograph design and validation, and pantograph hardware-in-the-loop studies.

In Chapter 3, a pantograph–catenary model and a framework for simulating pantograph–catenary interaction behaviour are developed. The simulation is validated against the EN

standard and a benchmark study. The model and result will serve as a source of truth for the pantograph–catenary interaction and will be used for the catenary control model development.

In Chapter 4, a novel disturbance-observer-based catenary model used for the active pantograph validation is proposed. The simulation results with a passive pantograph and an active pantograph are compared with the source of truth.

In Chapter 5, model-based active pantographs are designed with a variety of control methods ranging from classical to state-of-the-art control methods. The active pantographs are validated with the accurate catenary models in simulation.

In Chapter 6, a hardware-in-the-loop pantograph test rig is developed and introduced. A frame-actuated active pantograph is designed based on the system model and tested with the test rig.

Chapter 7 summarises the findings of the thesis and further recommendations are given.

CHAPTER 2 LITERATURE REVIEW

2.1 Introduction

Although some model-free control techniques have been developed over the last two decades (Fliess and Join, 2013), model-based control methodologies are generally applied for active control of a system. In model-based control theory, plant modelling is crucial for the designed system to achieve the desired performance (Hou and Wang, 2013). Once the plant model is available, controllers can be designed according to the requirements of the application. The requirements can be related to various performance metrics including zero-pole location, step or frequency response, performance-effort cost balance and disturbance rejection ability. As most control design methods rely on a linear plant, the controller is usually designed on a linearised model that is simplified from a real-world system. Eventually, the controller needs to be validated in the real-world situation. However, testing in the real world is risky and costly, so prior to testing in the real situation, the performance of the controller is usually evaluated on a more complex simulation model and in a laboratory environment.

To apply active control in railway pantographs through model-based control design workflow, the literature review is structured as follows to identify the research gaps. In Chapter 2.2, the modelling methods for the pantograph–catenary system are reviewed and compared with each other. In Chapter 2.3, the existing active pantograph studies are reviewed. Their applied control laws (including model-based and non-model-based) and validation situations are summarised and discussed. In Chapter 2.4, the existing hardware-in-the-loop pantograph test rigs are reviewed and the designed physical active pantograph prototypes in the laboratory are discussed.

It is worth mentioning that, in some literature, primarily related to process control in chemistry engineering, model-based control design refers explicitly to a particular area of control techniques, such as Internal Model Control and Model Predictive Control (Bosley et al., 1992, Brosilow and Joseph, 2002). However, in either case, these techniques also rely on plant modelling for controller design and thus broadly belong to the model-based control family.

2.2 Pantograph–catenary modelling and simulation

2.2.1 Pantograph modelling

As current collection plays a critical role in electric train operation, the dynamics of the pantograph–catenary system has been studied since the 1960s after the modern pantograph was invented (Faiveley, 1960). A photo of a physical pantograph is presented in Figure 2.2.1. The pantograph is designed to exert as constant as possible a force on the contact wire. In the early years, some pantograph–catenary studies fixed the contact forces to omit modelling of the pantograph (Andrews, 1964). Alternatively, simple lumped-mass pantograph models are used to interact with the catenary model by constraining the two entities at the contact point. The lumped-mass model used here is built by simplifying the pantograph into two mass blocks, containing the pantograph head mass and the pantograph body mass. As most of the research at this time was focused on the catenary system (Abbott, 1967) and contact force fluctuations (Gilbert and Davies, 1966), rather than pantograph design, the accuracy of the pantograph model was not particularly critical.



Figure 2.2.1. Sideview of a typical pantograph

The structure of physical pantographs can also be regarded to consist of three parts: the head, upper arm and support frame with the lower arm. Therefore, researchers naturally started to model the pantograph as a three-mass lumped-mass model, which is now widely used to study pantograph–catenary interaction and designs of the pantograph and catenary. Another weakness of a two-mass model arises because the model is inadequate to represent an asymmetric pantograph, while in a three-mass model, the elbow transmission behaviour between the arms can be approximately represented (Eppinger et al., 1988). Furthermore, as the pantograph head typically contains two contact strips, researchers have also proposed four- and five-mass pantograph models. A four-mass model can be developed by separating the head mass into two equal mass blocks representing the two contact strips (Kumaniecka and Prącik, 2003). A five-mass model adds two more mass blocks for the strips on the top of the pantograph head support mass (Schaub and Simeon, 2001).

These multi-mass pantograph models (can be seen in Figure 2.2.2) are developed to study pantograph–catenary interaction, but the parameters of the masses in the models below the head mass have no direct physical relationship to the physical pantograph and are generally identified experimentally (Antunes et al., 2012). Hence, a lumped-mass model can be regarded as a pure mathematical model. The properties of a lumped-mass model are usually obtained by matching

the frequency response function that is acquired from a physical pantograph (Pombo et al., 2012, Ambrósio et al., 2013), for its particular movement in an experiment. Therefore, a linear pantograph model can only be valid within a given working range where the model is identified (Poetsch et al., 1997). If the pantograph's operational condition (e.g., height) is significantly changed, the nonlinear elements of the pantograph will make the results of the linear model deviate from the original parameters.

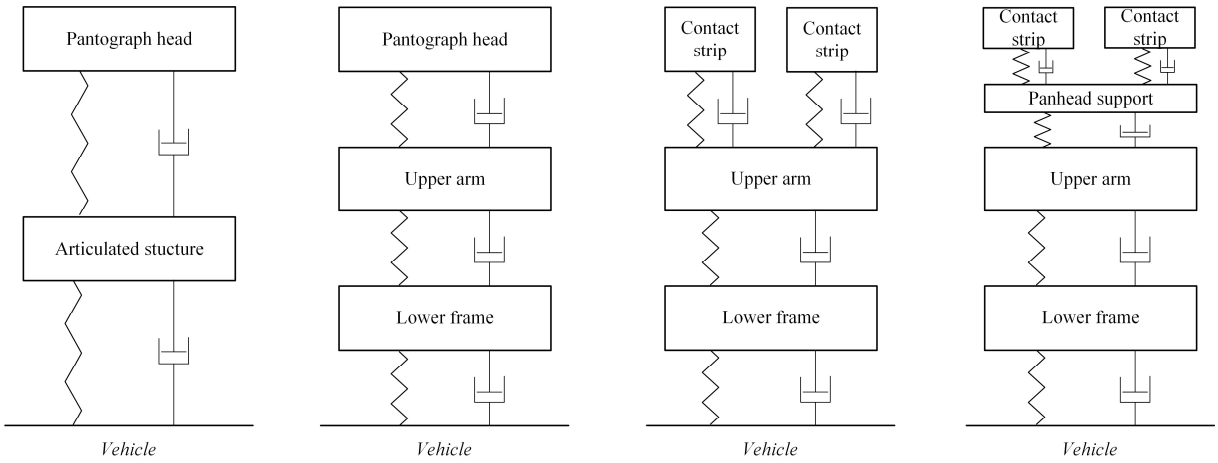


Figure 2.2.2. Pantograph lumped-mass models, from left to right: two-mass; three-mass; four-mass; five-mass

Considering the above limitations of linear pantograph lumped-mass models, nonlinear multibody pantograph models have been developed, which have the ability to describe pantograph dynamics over an extensive range of motion. A multibody model can be developed based on the pantograph datasheet provided by the manufacturer (Zdziebko et al., 2019) or based on experimental tests (Eppinger et al., 1988). As the parameters all have physical meanings, a multibody model offers an insight into the pantograph's dynamic behaviour for the study of pantograph optimisation (Bucca et al., 2012, Massat et al., 2014). A multibody model can also interact with other external interference on the pantograph, such as aerodynamics (Pombo et al., 2009), vehicle–rail effect (Ambrósio et al., 2012b) and track geometry (Antunes

et al., 2019). Moreover, a multibody model can be linearised into a lumped-mass model for linear controller design (Song et al., 2017b).

In addition, the motion of each current collector can be separately modelled through modal analysis in order to understand the rotation of the contact strips. The rotation is usually associated with high-frequency (more than 30 Hz) behaviour and is related to the mechanical wear problem (Collina and Bruni, 2002). A more complicated pantograph model can be obtained through the comprehensive framework proposed by Maier et al. (2018). The model is built from the measurement data of a physical pantograph, and has the features of local linearity and global nonlinearity. There are also a few studies using neural network techniques to develop nonlinear differential models of pantographs (Khan et al., 2020, Nisar et al., 2021); of course, these do not have physical meaning.

Due to the advantage of linearity, a linear lumped-mass model is still the most commonly used pantograph representation in pantograph–catenary system simulations. This type of model appears extensively in the research on pantograph–catenary interaction behaviour (Bruni et al., 2018), pantograph optimisation (Zhou and Zhang, 2011, Lee et al., 2012, Ambrósio et al., 2013, Su et al., 2022) and active pantograph design which will be focused on in Chapter 2.3.

2.2.2 Catenary modelling

Research on catenaries has also been widely carried out by researchers to improve pantograph–catenary dynamics. Modelling the catenary can help engineers and researchers to understand its structure and properties and these models also provide the opportunity of linking with pantograph models. Early research on catenary systems was mainly based on solving differential equations to find the steady state and motion of the structure (Levy et al., 1968, Scott and Rothman, 1974). The increase in computing power has given computers the ability

to solve dynamic problems of large complex systems. There are currently three main approaches to modelling catenary systems (Kia et al., 2010): modal-based, finite element- or finite difference-based, and time-varying lumped-mass models. Based on these three approaches, other innovative catenary models have also been developed (Abdullah et al., 2010, Cazzani et al., 2017, Duan et al., 2022, Gil et al., 2022), which can generally provide acceptable accuracy but with much less complexity, compared to the finite element model. A typical catenary system is shown in Figure 2.2.3.



Figure 2.2.3. A typical catenary system

Modal analysis is the process of using modal information to develop a mathematical model for a dynamic system. The modal information contains the system's inherent dynamic properties that can be obtained by solving the partial differential equation of the system dynamics (of a finite element catenary model, for example) or exciting the system experimentally. The model can then be developed by superimposing the acquired information at frequencies of interest (Fu and He, 2001). In catenary modelling, modal analysis decomposes the impact of the contact force on the catenary deformation, as shown in Eqn. 2.2.1, where w is the wire displacement, A is the Rayleigh–Ritz coefficient and L is the length of a catenary span. One of the advantages

of a modal model is that the number of modes can be reduced as desired (Gregori et al., 2019). The reduction is effective in ensuring computational efficiency in simulation. By doing so, real-time simulation of the catenary might be possible.

$$w(x,t) = \sum_{i}^{n} A_i(t)\sin(\frac{i\pi x}{L}) \tag{2.2.1}$$

The finite element method (FEM) and finite difference model (FDM) are widely used to solve structural analysis and dynamic simulation problems. They both subdivide a complicated system into smaller parts. By assembling the properties of small elements, the characteristics of the whole system can be approximately presented. Both methods apply the idea of discretisation to solve partial differential equations. For example, in the problem of modelling catenary wires, the partial differential equation is shown in Eqn. 2.2.2, where the variables ρ, A, w, T, E, I, c and F respectively denote the density of the wire, the cross-sectional area of the wire, the vertical deflection of the wire, the tensile force of the wire, the Young's modulus of the wire, the second moment of area of the wire, the damping coefficient and the external force.

$$\rho A\frac{d^2w}{dt^2} = T\frac{d^2w}{dx^2} - EI\frac{d^4w}{dx^4} - c\frac{dw}{dt} + F(x,t) \tag{2.2.2}$$

As the FEM introduces a weighting shape function that relates to physical properties, it is supposed to be more accurate, at computational cost (Mulder, 1996). In recent years, the FEM has been the dominating approach to solving catenary modelling problems for pantograph–catenary simulation (Bruni et al., 2018), partly due to the high recognition of the FEM in the field of solid and structural mechanics and the development of its commercial software. The FEM-based catenary modelling approach offers a high degree of flexibility in catenary modelling and allows for understanding the dynamics of all parts (Poetsch et al., 1997).

Therefore, some studies have been conducted on the catenary components, such as the dropper type (Bruni et al., 2012), length (Su et al., 2022) and spacing (Gregori et al., 2018); wire tension (Su et al., 2022), density (Zhang et al., 2019a) and height (Gregori et al., 2018); gradient (Hayes et al., 2021); and overlap section (Gregori et al., 2020).

Comparing the modal-based with FE-based catenary models, FEM provides a more accurate solution for nonlinear systems (the slackening of droppers results in nonlinearity in the catenary, for example). However, FEM requires more computational resources and is more complex to implement. On the other hand, modal-based models are simpler and faster to compute, making them useful when computational resources are limited. The choice between the two approaches depends on the specific requirements of the problem and the available resources. A combination of both approaches could also be used to balance accuracy and computational efficiency. A numerical comparison between the two methods in simulating the pantograph–catenary interaction can be found in (Kia et al., 2010).

Relatively simple mass–damper–spring catenary models (called time-varying lumped-mass catenary models in this thesis) are also used, mainly in the study of active pantographs. The essence of this type of model is to use spatially varying stiffness to represent the perturbation in system dynamics, as shown in Eqn. 2.2.3, where m, c and $k(t)$ are the coefficients of the mass–damper–spring model, L is the length of one span, and k_{max} and k_{min} are the largest and smallest stiffness in a span.

$$m\ddot{x} = c * \dot{x} + k(t) * x + F(x,t) \tag{2.2.3}$$

with

$$k(t) = k_0\left(1 + \alpha\cos\left(\frac{2\pi V}{L}t\right)\right)$$

$$k_0 = \frac{k_{max} + k_{min}}{2}$$

$$\alpha = \frac{k_{max} - k_{min}}{k_{max} + k_{min}}$$

The time-varying stiffness can also be explicitly obtained offline by applying a force on the contact wire at each small step either in the FE model (Bruni et al., 2015) or a physical overhead line section (Balestrino et al., 2000). However, the stiffness lookup table is generally obtained based on the assumption that the vehicle is stationary under the catenary. As it is known that the actual dynamic behaviour depends on the running condition, the accuracy of time-varying lumped-mass models varies with speed (Wu and Brennan, 1997, Lopez-Garcia et al., 2007). Another critical weakness of these models is that they cannot reproduce either the phenomenon of wire wave propagation and reflection by the droppers and suspensions or the geometry of the catenary under gravity loading, which have been seen as the largest contributors to contact force variations (Vo Van et al., 2017), especially for the multi-pantograph case (Bruni et al., 2018). Therefore, the veracity of time-varying lumped-mass catenary models has been questioned (Allotta et al., 2008, Sanchez-Rebollo et al., 2013, Duan et al., 2022). Nevertheless, as time-varying lumped-mass models can be easily linearised, they are dominantly applied in active pantograph design and sometimes validation.

To summarise the catenary modelling methods in the literature, the modal-based method regards the catenary system (i.e., the displacement of contact wire) as a mathematical representation that contains the frequency response information; the FEM discretises the system and provides thousands of degrees of freedom; and a time-varying lumped-mass model uses spatially varying stiffness to represent the catenary structural variation. Among them, FE models are widely acknowledged to offer the best accuracy but can result in computational

difficulty because of their complexity. In addition, FE models can be used to develop modal and time-varying lumped-mass models, both of which can achieve fast simulation by storing information offline in advance. Besides that, as time-varying lumped-mass catenary models can be easily linearised, they are often preferred in active pantograph designs, but their veracity is of concern because they are incapable of reproducing the wave propagation in wires.

2.2.3 Contact (interaction) models

The efficiency of current transmission and mechanical abrasion depend on the quality of the pantograph–catenary contact (Nåvik et al., 2017), which implies that a proper model for the interaction between the pantograph head and contact wire is essential for analysing the contact quality in a simulation. There are two widely used approaches to the interaction model: penalty contact and rigid (constrained) contact.

In the penalty method, contact forces are calculated based on the relative kinetic states of the two contacting objects. A common and straightforward way of applying the penalty method is placing a virtual spring to connect the pantograph head and contact wire; thus, the elastic force of the spring can be regarded as the contact force. A widely accepted value for the stiffness of the virtual spring in pantograph–catenary simulations is 50,000 N/m (Bruni et al., 2015). Some more complicated penalty models have also been used, which might be preferred if the internal damping (Collina and Bruni, 2002, Rauter et al., 2007) or friction force (Flores et al., 2011) needs to be considered. It has been concluded that the penalty method is capable of describing all relevant features of the pantograph–catenary interface (Ambrósio et al., 2012b), and the advantage of using the penalty method is its convenience for generating contact forces and identifying contact losses (Seo et al., 2005).

Compared to the penalty method, with the rigid (constrained) method, the pantograph and catenary are assumed to be not separated from each other (thus, it is difficult to identify the contact loss). The method imposes constraints on the relative motion at the contact point on the pantograph head and the contact wire. These constraints are formulated in terms of algebraic equations, by which the kinetic conditions of the pantograph head and contact wire constraint at the contact point are enforced. Rather than calculating from a spring (or more complicated ones) as in the penalty method, the contact force in the rigid contact method is obtained by considering the reaction force of the kinematic constraint (Seo et al., 2005).

Both methods appear in pantograph–catenary interaction studies. The rigid contact method does not need to introduce a physical contact model that has to be validated in generating the contact force. However, if integrated with an FE catenary model, a rigid contact model requires a complicated procedure to account for the kinetic states due to contact wire discretisation, which may also result in computational effort and numerical problems (Collina and Bruni, 2002).

2.2.4 Summary of pantograph–catenary modelling

In this section, the methods used for modelling for the pantograph, catenary and their interaction in pantograph–catenary studies are listed and summarised. In Table 2.2.1, previously reviewed papers as well as relevant simulation studies, as far as the author knows, are listed (in alphabetical order by institution) to present the modelling methods used. For the sake of brevity, only one of the papers that use similar simulation code with similar modelling methods is listed as a representative. As active pantograph design and validation are the main interest of this thesis, whether the simulation code (framework) is related to active pantographs is also identified. In addition, hardware-in-the-loop work is also included, marked as ‘physical’ for the pantograph and ‘HIL’ for the interaction sections.

It is clear from the table that most of the simulation frameworks chose a lumped mass as the model for the pantograph. A multibody pantograph model might only be used for simulations that do not need controller designs (but may be used for controller validations).

The FEM is the primary approach for catenary modelling to imitate the interaction between the pantograph and catenary. A simplified time-varying lumped-mass catenary model is only used for active pantograph study due to the complexity of FE models, although some studies use FE models for further controller validation. There are some active pantograph studies that do not use a lumped-mass catenary model, which is because their controllers were designed using pantograph models in isolation. For research conducting experiments on pantographs using hardware-in-the-loop, modal-based models are a popular method for modelling the catenary.

It is interesting and notable that in studies using lumped-mass catenary models, the choice of catenary mass value is very inconsistent. In some studies it is assumed to be negligible (Poetsch et al., 1997, Wu and Brennan, 1997, Rachid, 2011, Karaköse and Gençoğlu, 2012, Lin et al., 2015, Lu et al., 2017, Zhu et al., 2019, Song and Li, 2020) , and in others it is related to the physical mass (Balestrino et al., 2000, Pisano and Usai, 2008, Kia et al., 2010, Sanchez-Rebollo et al., 2013, Ko et al., 2016) which ranges from 30 to 195 kg. Similarly, there are also different choices for the parameter of damping coefficient. A new parameterisation approach will be proposed in this thesis in Chapter 4.2.2.

The majority of studies using an FE catenary model chose the penalty method as the interaction model. For studies using a time-varying lumped-mass catenary model (for active pantograph designs), if it is still validated with a time-varying lumped-mass catenary, most studies have chosen rigid contact, but if it is validated with an FE model, penalty contact is also used for both design and validation.

Table 2.2.1. Summary of modelling methods applied in simulation codes

Reference	Institution	Pantograph	Catenary	Interaction	Active pantograph involved?
(Zdziebko et al., 2019)	AGH University of Science and Technology	Multibody (validation only)	FEM (validation only)	Rigid	Yes
(Zhu et al., 2019)	Beihang University	Lumped mass	Lumped mass	Rigid	Yes
(Zhang et al., 2019a)	Beijing Jiaotong University	Lumped mass	FEM	Penalty	No
(Song and Li, 2020)	Chongqing University	Lumped mass	Lumped mass	Rigid	Yes
(Finner et al., 2015)	Deutsche Bahn	Lumped mass, multibody	FDM	Rigid	No
(Poetsch et al., 1997)	Deutsche Bahn	Lumped mass	Lumped mass	Rigid	Yes
(Kia et al., 2010)	ESIEE Amiens	Lumped mass	Lumped mass, modal, FEM	Penalty	No
(Lin et al., 2015)	Feng Chia University	Lumped mass	Lumped mass	Rigid	Yes
(Karaköse and Gençoğlu, 2012)	Firat University	Lumped mass	Lumped mass	Rigid	Yes
(Ambrósio et al., 2015)	IST Technical University of Lisbon	Lumped mass, multibody	FEM	Penalty	No
(Cho, 2015)	Korea Railroad Research Institute	Lumped mass	FEM	Penalty, rigid	No
(Jönsson et al., 2015)	KTH Royal Institute of Technology	Lumped mass	FEM	Penalty	No
(Song et al., 2020)	Norwegian	Lumped mass	FEM	Penalty	No

	University of Science and Technology				
(Collina et al., 2015)	Politecnico di Milano	Lumped mass	FEM	Penalty	No
(Diana et al., 1998)	Politecnico di Milano	Lumped mass	Modal (validation only)	Rigid	Yes
(Facchinetti and Mauri, 2009)	Politecnico di Milano	Physical	Modal (validation only)	HIL	Yes
(Sanchez-Rebollo et al., 2013)	Pontifical Comillas University	Lumped mass	Lumped mass (validation), FEM (validation)	Penalty	Yes
(Sánchez-Rebollo et al., 2015)	Pontifical Comillas University	Lumped mass	FEM	Penalty	No
(Ikeda, 2015)	Railway Technical Research Institute	Lumped mass	FEM	Penalty	No
(Ko et al., 2016)	Railway Technical Research Institute	Lumped mass	Lumped mass	Rigid	Yes
(Massat et al., 2006)	SNCF	Lumped mass	FEM, modal	Penalty, Rigid	No
(Massat et al., 2015)	SNCF	Lumped mass, multibody	FEM, modal	Penalty	No
(Lu et al., 2017)	Southwest Jiaotong University	Lumped mass	Lumped mass (design), FEM (validation)	Rigid	Yes
(Song et al., 2017b)	Southwest Jiaotong University	Multibody (validation only)	FEM (validation only)	Penalty	Yes
(Zhang et al., 2002)	Southwest Jiaotong University	Physical	Modal	HIL	No

(Zhang et al., 2006)	Southwest Jiaotong University	Lumped mass, multibody	FEM	Penalty	No
(Zhou et al., 2015)	Southwest Jiaotong University	Lumped mass	Modal	Penalty	No
(Wu and Brennan, 1997)	Tongji University	Lumped mass	Lumped mass	Rigid	Yes
(Pisano and Usai, 2008)	Universitá di Cagliari–Piazza d'Armi	Lumped mass	Lumped mass	Rigid	Yes
(Tur et al., 2015)	Universitat Politècnica de València	Lumped mass	FEM	Penalty	No
(Thompson and Davis, 1990)	University of Adelaide	Lumped mass	No validation with catenary models	Rigid	Yes
(Duan et al., 2022)	University of Birmingham	Lumped mass	Lumped mass (design and validation), FEM (validation)	Penalty	Yes
(Kulkarni et al., 2017)	University of Illinois at Chicago	Multibody	FEM	Penalty, Rigid	No
(Rachid, 2011)	University of Picardie Jules Verne	Lumped mass	Lumped mass	Rigid	Yes
(Balestrino et al., 2000)	University of Pisa	Lumped mass	Lumped mass	Penalty	Yes
(Pappalardo et al., 2015a)	University of Salerno	Lumped mass (design), multibody (validation)	FEM (validation only)	Rigid	Yes
(Hayes et al., 2021)	University of Sheffield	Lumped mass	FEM	Penalty	No

2.3 Active pantographs

As the speed of trains increases, the industry and researchers have begun to question whether the current pantograph design or mechanism can still ensure continuous current transmission from overhead line to vehicle (Manabe, 1992, Scott and Cook, 1996). Besides the increase in speed, low noise and high reliability are also required in modern public transit. Even if a pantograph–catenary system is well-maintained, it is still vulnerable to unexpected interference (Poetsch et al., 1997). To improve the robustness of the pantograph–catenary interaction in dealing with environmental change; to solve interoperability issues; and to ensure a more consistent force during routine running, one of the solutions is the application of feedback control on the pantograph.

When the vehicle is stationary, the pantograph is in contact with the catenary and maintains a constant contact force through its static upward pneumatic force. At this point, the pantograph–catenary system is not affected by any disturbance (ideally) and thus maintains its steady state. When the vehicle starts to move, an intuitive change is that the pantograph–catenary contact point follows the geometry of the contact wire, and the contact force cannot be maintained at the desired value. If the pantograph and catenary are considered as an integrated system, these changes within the system can be considered as an internal perturbation on top of its nominal state. In addition, external disturbances (such as strong wind (Song et al., 2017a)) to the system may also be of concern.

To attenuate the effect of system disturbances (including the impact of catenary geometry, external interference, etc.), an active controller and responding actuator can be used. There are two main approaches to designing control systems to reject disturbances: feedforward and feedback, as shown in Figure 2.3.1. Feedforward control relies on knowledge of the disturbance

to be controlled. This is often applied in situations where system disturbances have real physical meanings and can be measured or estimated (Liu et al., 2019). For feedback control, the controller needs the measured value of the system output. In order to attenuate the effect of disturbances, the system modifies the control input according to the actual output value. The efficacy of the two control methods depends on the loop response speed and, according to (Elliott and Sutton, 1996), when the system delay is very small, feedback control may outperform feedforward control. However, the choice between them, or combining the two, depends more on the knowledge of the disturbance in practice. For a pantograph–catenary system, because the sources of disturbance are diverse, complex and correlated, it is unrealistic to measure all sources through sensors, so using feedback control for active pantograph design is more feasible.

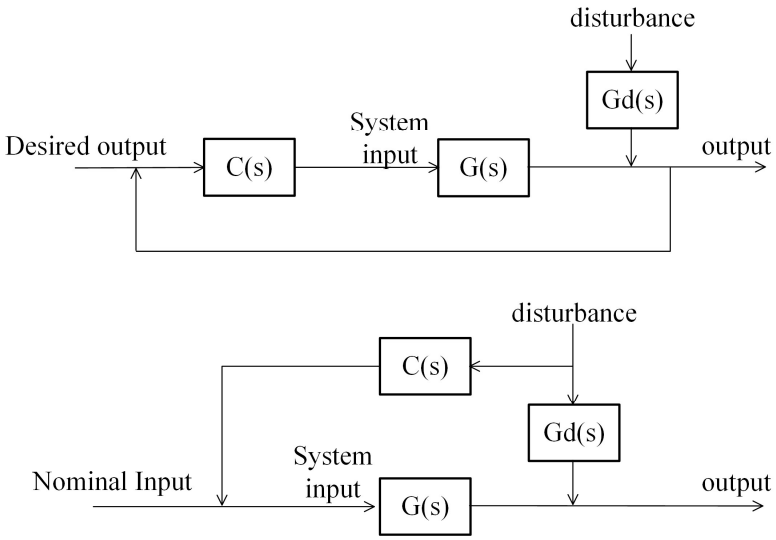


Figure 2.3.1. Block diagrams of typical active controls, top: feedback; bottom: feedforward

The general target of active pantograph control is to improve the pantograph–catenary dynamics. Many indicators can be used to reflect the condition of pantograph–catenary interaction, including contact force, catenary uplift (Pombo and Ambrósio, 2012), the possibility of contact loss (Zhou et al., 2011) and wire stress (Seo et al., 2006). However, it is noted that the contact

force is the most common one that can be used to understand the internal physical variations of a coupled system (Scott and Cook, 1996). Regarding the contact force data, their standard deviation is a measure of the amount of variation, which can reflect the contact force fluctuation along a catenary section. Also important are the maximum and minimum values, which can help identify point wear, loss of contact and other local effects (Nåvik et al., 2017).

To realise feedback control, the pantograph–catenary contact force needs to be measured. The two common approaches are placing load cells between the collector and its suspension and fitting fibre optic sensors under the carbon strip (Bruni et al., 2018). Some prototypes have been tested on main lines (Collina and Bruni, 2002, Paik et al., 2012, Schröder et al., 2013, Finner et al., 2015, Nåvik et al., 2017). The methods for measuring or estimating contact forces have also been used in experiments with active pantograph study (Collina et al., 2005, Allotta et al., 2008, Facchinetti and Mauri, 2009).

Research on active pantographs based on feedback can be classified in three ways: the position of the actuator on the pantograph where the control force is applied, the method of designing the controller, and the validation conditions of the closed-loop system.

The control force can be applied on the articulated frame, in parallel with the head suspension or on the pantograph head directly, as shown in Figure 2.3.2. The control force on the frame acts possibly in the same way as the pantograph is subjected to its original pneumatic force, and the other two methods require installation on the pantograph head. The difficulty of these three approaches ranges from easy to difficult, but their control bandwidth ranges from narrow to wide (Poetsch et al., 1997) (Bruni et al., 2018).

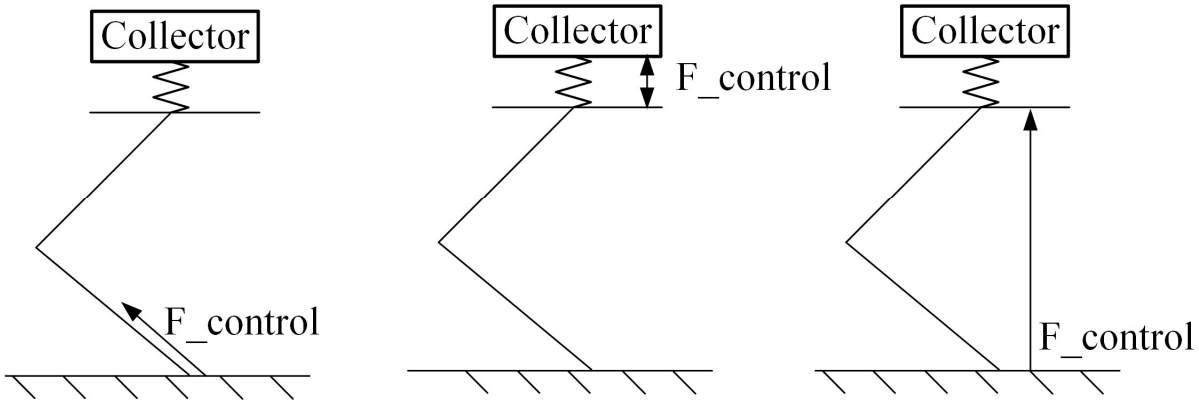


Figure 2.3.2. Placement of active actuators, from left to right: on the lower frame; in parallel with the head suspension; on the pantograph head directly

The methods for controlling active pantographs fall broadly into two categories: classical control and advanced (modern) control. There are many correlations between the two approaches but, generally, classical control theory is usually designed using transfer functions and the frequency domain, while advanced control theory uses state-space representations, which offers an insight into systems for complex problems (Wiberg, 1971). Considering the control problem of the pantograph–catenary system, many control methods have been used to make the system more resistant to disturbances, thus making the contact force fluctuation smaller. The active pantograph control methods found in the literature are summarised in Table 2.3.1.

Table 2.3.1. Summary of active pantograph designs from the literature

Reference	Actuated place	Main control design method	Validation stage
(Thompson and Davis, 1990)	Frame	Linear–quadratic regulator	1
(O'Connor et al., 1997)	Frame	Linear–quadratic regulator	1
(Wu and Brennan, 1997)	Frame	Linear–quadratic regulator	1
(Balestrino et al., 2000)	Frame and head	Proportional-integral	1

(Lin et al., 2007, Lin et al., 2015)	Head	Linear–quadratic regulator	1
(Pisano and Usai, 2008)	Frame and head	Sliding mode control	1
(Gaing and Chang, 2009)	Frame	PID + particle swarm optimisation (non-model-based)	1
(Walters, 2010)	Frame	Fuzzy control	1
(Rachid, 2011)	Frame	Linear matrix inequality	1
(Ko et al., 2016)	Frame	Linear–quadratic regulator	1
(Abdullah et al., 2010)	Frame	Proportional control + trial and error (non-model-based)	2
(Sanchez-Rebollo et al., 2013)	Frame	PID + Pareto front optimisation (non-model-based)	1 and 2
(Pappalardo et al., 2015b)	Head suspension	Derivative control + iterative optimisation (non-model-based)	2
(Song et al., 2017b)	Frame and head	Proportional-derivative control + trial and error (non-model-based)	2
(Lu et al., 2017, Zhang et al., 2019b, Lu et al., 2018, Lu et al., 2021)	Frame	H-infinity	2
(Duan et al., 2022)	Frame	Proportional–integral–derivative	1 and 2
(Collina et al., 2005)	Head suspension	Proportional control, high order controller + trial and error (non-model-based)	2 and 3 (but with an incomplete pantograph)
(Allotta et al., 2008)	Frame	Proportional-derivative control + trial and error (non-model-based)	3
(Facchinetti and Mauri, 2009)	Head suspension	Proportional control (non-model-based)	3

A controller is usually designed on a linearised system model (Brosilow and Joseph, 2002). Once an active pantograph controller is designed based on a linear model, it needs to be validated to some extent. Active pantograph validation can be classified into four stages: 1) with a pantograph model plus time-varying lumped-mass catenary model, 2) with a pantograph model plus detailed (such as FE) catenary model, 3) with a physical pantograph plus catenary model (HIL) and 4) with a physical pantograph and catenary (test run). The models used in active pantograph controller design and validation at different stages are summarised in Figure 2.3.3.

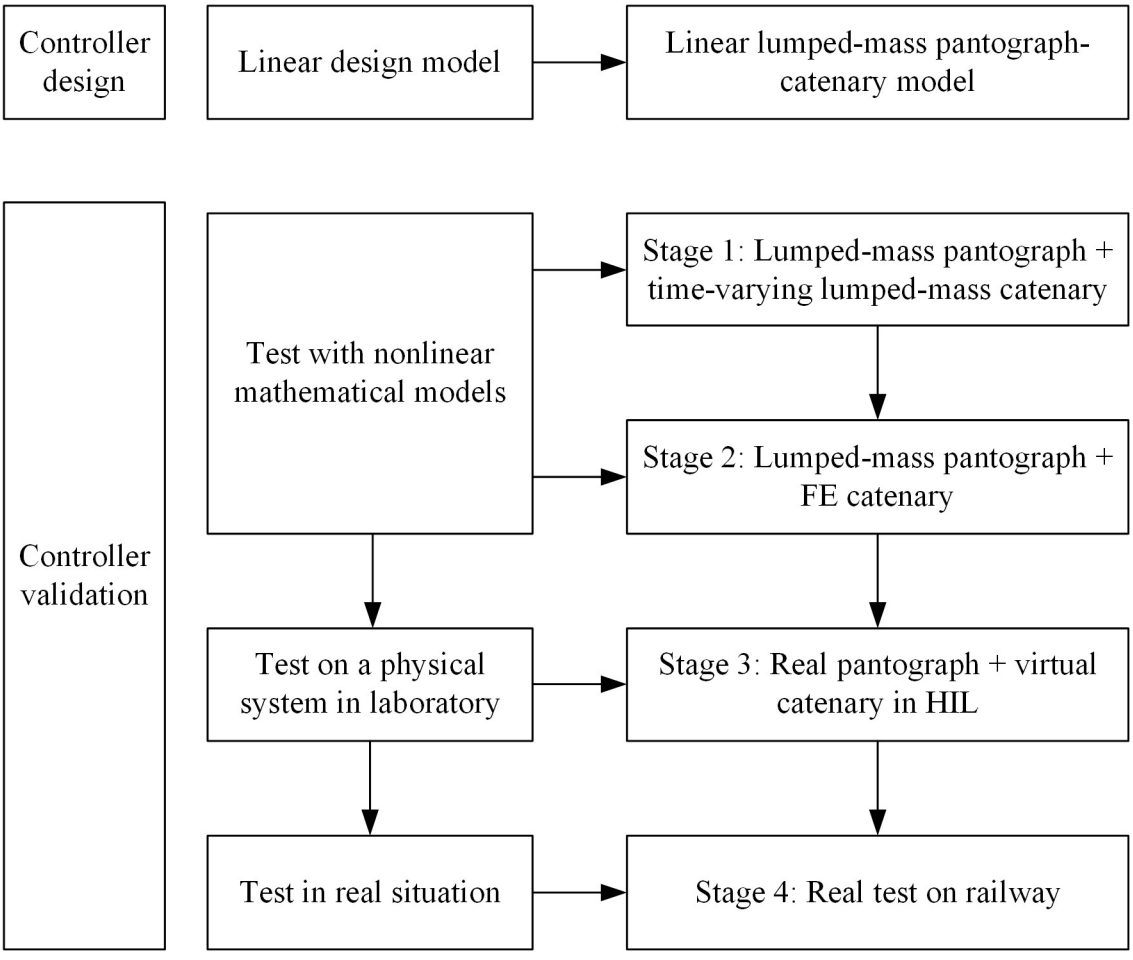


Figure 2.3.3. The models used in model-based active pantograph design and validation at different stages

As shown in Table 2.3.1, many advanced control methods (including model-based and non-model-based) for pantograph–catenary systems have been developed at stage 1, and the results have been excellent. However, few model-based active pantograph studies have been validated with FE catenary models at stage 2. In those studies validated with both time-varying lumped-mass and FE catenary models, it was found that a controller validated with a simple catenary model may produce an over-optimistic result as time-varying lumped-mass catenary models often fail to exhibit high-frequency contact force components (Sanchez-Rebollo et al., 2013, Duan et al., 2022).

Similarly, a model-based controller may not be effective in an experiment with a physical pantograph. Therefore, it can be found, at stage 3, that the controller parameterisation for an active pantograph is not based on its mathematical model but through trial and error in the experiment (Collina et al., 2005, Allotta et al., 2008, Facchinetti and Mauri, 2009). Although the controller designs in these works are not model-based, they have been tested and have demonstrated effective results in reducing contact force variation. As the above two applications at stage 3 involve a laboratory experiment, they will be discussed in Chapter 2.4.

Furthermore, to the author's knowledge, there are two records of active pantograph test runs. It was developed by Deutsche Bahn in Germany (Baldauf et al., 2005) and Brecknell Willis in the Unitied Kingdom (Railtechnologymagazine, 2016). However, the design and testing details are not available in the published literature.

2.4 Pantograph test rigs and hardware-in-the-loop (HIL) experiments

Although simulation can provide a good picture of the dynamics of a pantograph–catenary system, simplification of the pantograph into numerical models might be critical in active

pantograph validation and implementation. Therefore, controller testing on physical pantographs in the laboratory is a key step of validation. Not only for active pantographs, pantograph research and design usually need to be tested in the laboratory before being installed on a vehicle for test runs.

The main idea of pantograph test rigs is to apply an actual pantograph to interact with a force applied by actuators driven from a virtual catenary program. This allows the pantographs to be activated and their static and dynamic characteristics to be tested. A test rig built in Germany, as shown in Figure 2.4.1, aimed to optimise the design of pantographs (Deml et al., 2001) and to identify the parameters of linear pantograph models (Conway, 2016). The vertical movement of the pantograph is excited by a hydraulic actuator. The movement of the actuator follows pre-defined profiles that can reproduce the pantograph–catenary contact point displacement. The displacement information can be obtained from either line tests or numerical simulations so that the dynamics of the pantograph can be excited properly.



Figure 2.4.1. Pantograph test bench built at Deutsche Bahn, Germany (Deml et al., 2001)

One of the drawbacks of using a pre-defined movement profile is that because the pantograph displacement depends upon the operating conditions, such as the uplift force applied, it should

change with a change of pantograph condition or design. Hence, closed-loop HIL pantograph test rigs have been extensively developed and used by a number of researchers.

HIL (also called 'hybrid') experiment is increasingly being used for system design and analysis where part of a system can be modelled in software (Isermann et al., 1999). The behaviour of the virtual model can be represented by an auxiliary equipment that interacts with the physical system to be tested. The real-time data of the physical system's behaviour can be measured by sensors and used to excite the virtual part in simulation. The use of HIL systems can help to significantly reduce the risk and cost of experiment.

In a closed-loop test rig, the contact force between the contact element and the pantograph head is sent back to the virtual catenary in the host PC or microprocessor. The catenary model can then respond to the contact force and generate the height command to the test rig, and thus the contact point emulator can behave following displacement of the 'catenary'. Three closed-loop pantograph test rigs found in recent papers (Zhang et al., 2002, Collina et al., 2004, Schirrer et al., 2017) are presented in Figure 2.4.2. In the first two test rigs, the virtual catenary models are designed based on modal analysis. To improve the accuracy of the modal-based model in HIL, the catenary dropper's nonlinear model (Resta et al., 2008) and an Extended Kalman Filter are further included (Facchinetti and Mauri, 2009). A different virtual catenary approach is applied in the last newly built test rig, where the catenary model is described in a method called pantograph-fixed coordinates, proposed by Ritzberger et al. (2015).

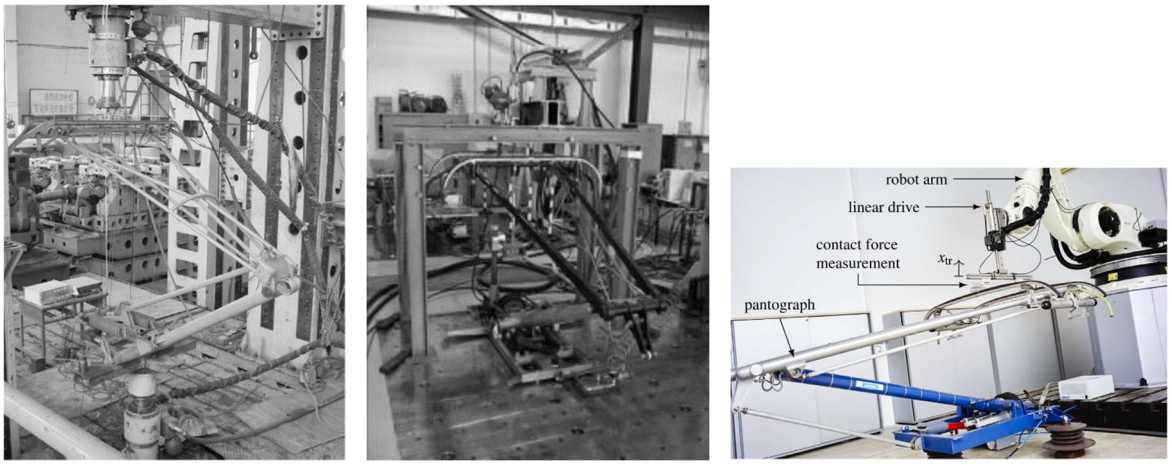


**Figure 2.4.2. Pantograph HIL test rigs,
from left to right: test rig in Chengdu, China (Zhang et al., 2002); test rig in Milan, Italy (Collina et al., 2004); test rig in Vienna, Austria (Schirrer et al., 2017)**

Besides these contact point emulation test rigs, there are also some spinning test rigs that have been used for the study of lateral impact, mechanical wear, stagger effect, etc. (Park et al., 2003, Bruni et al., 2004, Wei et al., 2013, Stoten et al., 2016).

The University of Birmingham (UoB) pantograph test rig, which was developed in 2017, will be introduced in detail in Chapter 6.2.

As mentioned previously, for results to be believable by real-world practitioners (industry) an active pantograph needs to be validated with a test rig, but few studies have done so. Three works have used proportional (Collina et al., 2005, Facchinetti and Mauri, 2009) and proportional-derivative (Allotta et al., 2008) controllers for active pantographs and tested them with test rigs. Collina et al. (2005) tested active controllers on a pantograph head collector instead of a full-size physical pantograph with an imposed pre-defined motion of excitation. As the articulated pantograph structure was neglected, this study cannot be regarded as a test on a physical pantograph.

Allotta et al. (2008) used a hydraulic actuator in parallel with a pneumatic uplift force (placed on the frame), and the active pantograph was tested with imposed sinusoidal displacement. The

results showed that the active pantograph is effective in reducing force fluctuation when tested with low-frequency (< 2 Hz) sinusoidal profiles.

Facchinetti and Mauri (2009) placed an electric actuator inside the joint between the pan head and the head frame in parallel with the collector suspensions. The active pantograph was tested in a closed-loop test rig where a modal-based virtual catenary model was installed. The active pantograph experiment was shown to be effective in attenuating low-frequency (< 4 Hz) contact force variation.

Although the above active pantograph prototypes have been tested with test rigs, there are two research gaps that can be further explored. First, as only the pantograph head-actuated configuration has been tested in a closed-loop HIL test rig, it is worthwhile to develop and test a frame-actuated active pantograph in a closed-loop test rig. Due to the inherent difficulty in high-frequency control of objects, the limitation of the control bandwidth for frame-actuated systems is not as significant. This highlights the advantage of its ease of installation in the implementation of active pantograph. Second, the active pantograph controllers tested with test rigs have not been designed based on a pantograph–catenary system model. A model-based active pantograph prototype should be explored, which might be beneficial in delivering better controller performance.

2.5 Summary and Conclusion

The literature review has revealed that, research into active pantographs has attracted many scholars in both railway and control fields. Most studies start with simulation, which requires detailed models for the pantograph–catenary system. In recent years, on the one hand, the combination of a lumped-mass pantograph and an FE-based catenary has dominated in the

modelling focusing on pantograph–catenary dynamics. On the other hand, a simple lumped-mass catenary model is preferred among active pantograph studies due to its linear property.

The simplified lumped-mass catenary model has led to many active pantographs being developed, but it is found that the controller validated with the lumped-mass catenary with time-varying parameters tends to produce over-optimistic results. Therefore, great caution is needed when a simple lumped–mass catenary is used for the pantograph–catenary simulation. This finding will be confirmed and discussed in Chapter 4 in this thesis, and a new disturbance-observer-based catenary model will be designed to replace the role of the traditional lumped-mass catenary model for active pantograph validation in simulation. The new model is also real-time capable and can be used in the design of pantograph HIL experiment.

It was also found that not many active pantograph studies have been validated with accurate catenary models (such as FE catenary). Even so, most of them use PID controllers but are not tuned based on a mathematical model of the pantograph–catenary system. Therefore, in this thesis, a variety of control laws will be applied to the design of an active pantograph based on the model, and they will be tested (with the validated) with accurate catenary models to explore the effectiveness of the model-based active pantograph (Chapter 5).

After designing active pantographs in simulation, the next step should be performing HIL tests in a laboratory condition. However, only a very limited number of validation works regarding physical active pantographs have been done, and none of their controllers were designed model-based. Therefore, a model-based active pantograph prototype will be developed in the laboratory and tested with an HIL environment (Chapter 6). Moreover, as the frame-actuated active pantograph has not been tested in the HIL environment in the previous studies, the model-based active pantograph will be designed to be actuated from the pantograph frame.

CHAPTER 3 PANTOGRAPH–CATENARY MODELLING AND SIMULATION

3.1 Introduction

Modelling the pantograph–catenary system is essential to model-based active pantograph designs. An accurate pantograph–catenary system model not only offers a source of truth when testing the active controller in simulation but also provides the underpinning information for the development of the simplified models for active control design and validation.

In this chapter, a detailed mathematical pantograph–catenary model is developed. The three subsystems, pantograph, catenary system and interaction between them, are modelled in Chapters 3.2, 3.3 and 3.4, respectively. The resulting model is constructed in Matlab-Simulink where the static and dynamic simulation functions and workflows are presented in Chapter 3.5. The results based on the developed pantograph–catenary simulation framework are validated against the EN standard and a pantograph–catenary simulation benchmark study in Chapter 3.6.

3.2 Lumped-mass pantograph model

In Chapter 2.2.1, it was found that lumped-mass models are widely accepted for most simulation-based pantograph–catenary studies. The lumped-mass model is a mathematical abstraction rather than a physical representation of a pantograph, so the parameters generally need to be identified experimentally rather than based on the physical datasheets of components (Ambrósio et al., 2013).

Identification of the parameters of a real pantograph will be discussed later, in Chapter 6.3. Here, to validate the simulation framework developed in this work, the three-mass lumped-mass pantograph model proposed in EN 50318:2018 (BSI, 2018) is used. In the three-mass model, the pantograph is simplified into three lumped components: the frame and lower arm, upper arm and pantograph head, as shown in Figure 3.2.1. The parameters of the referenced three-mass model (BSI, 2018) are listed in Table 3.2.1.

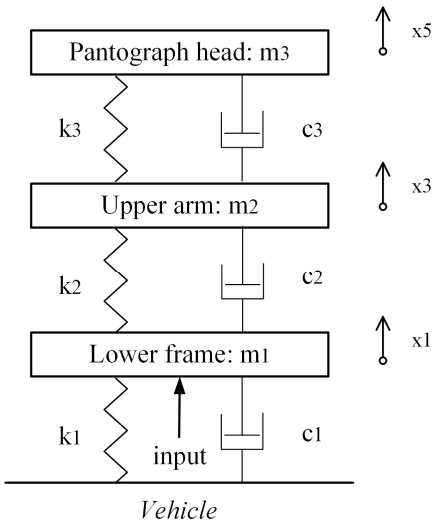


Figure 3.2.1. Three-mass lumped-mass pantograph model

Table 3.2.1. Parameters of the three-mass model

	Mass (kg)		Spring (N/m)		Damper (Ns/m)	
Lower frame	m1	6.0	k1	160	c1	100
Upper arm	m2	9.0	k2	15500	c2	0.1
Head	m3	7.5	k3	7000	c3	45

Expressing the kinetic relationships between the three mass blocks in a compact way, the model's representation in state space is given in Eqn. 3.2.1, where m_1, m_2 and m_3 are the mass of the lower frame, upper arm and pantograph head; k_1, k_2 and k_3 are the spring coefficients;

c_1, c_2 and c_3 are the damper coefficients; x_1, x_3 and x_5 are the mass displacements and x_2, x_4 and x_6 are the mass velocities. The system input u is the pneumatic uplift force on the pantograph. As gravitational acceleration does not affect the system dynamics, due to being a steady-state offset, it is omitted in the simulation and design process.

$$\dot{x} = Ax + Bu \tag{3.2.1}$$

where

$$x = [x_1 \quad x_2 \quad x_3 \quad x_4 \quad x_5 \quad x_6]^T$$

$$A = \begin{bmatrix} 0 & 1 & 0 & 0 & 0 & 0 \\ -\frac{(k_1+k_2)}{m_1} & -\frac{(c_1+c_2)}{m_1} & \frac{k_2}{m_1} & \frac{c_2}{m_1} & 0 & 0 \\ 0 & 0 & 0 & 1 & 0 & 0 \\ \frac{k_2}{m_2} & \frac{c_2}{m_2} & -\frac{(k_2+k_3)}{m_2} & -\frac{(c_2+c_3)}{m_2} & \frac{k_3}{m_2} & \frac{c_3}{m_2} \\ 0 & 0 & 0 & 0 & 0 & 1 \\ 0 & 0 & \frac{k_3}{m_3} & \frac{c_3}{m_3} & -\frac{k_3}{m_3} & -\frac{c_3}{m_3} \end{bmatrix}$$

$$B = \begin{bmatrix} 0 & \frac{1}{m_1} & 0 & 0 & 0 & 0 \end{bmatrix}^T$$

3.3 Finite Element-based catenary model

As discussed in Chapter 2.2.2, the finite element method (FEM) is the dominant approach to catenary modelling in research focusing on reproduction of the pantograph–catenary interaction dynamics. As shown in Figure 3.3.1, the catenary system consists of many components, such as wires, droppers, steady arms (cantilever) and masts (supports). The modelling of these parts will be discussed separately in the following subsections. Note that, in this thesis, the 'simple AC' catenary structure described in EN 50318:2018 is considered. The catenary shown in

Figure 3.3.1 is a ‘simple AC’ type where the droppers near the mast position are lifted by the messenger wires rather than stitch wires.



Figure 3.3.1. A typical pantograph–catenary system

3.3.1 Wires

Considering the simplification of the pantograph model and the research scope, the modelling is focused on the vertical system kinetics and the impact of axial wire tensile force. Therefore, a 2-D Euler–Bernoulli type of beam element is used for the wire FE modelling, which can accurately represent the load-carrying and deflection characteristics of beams (wires).

For each discretised node of a tensioned beam, the combined force in the vertical direction is equal to the sum of the effect of tension, bending moment, damping and the external force, as expressed in Eqn. 3.3.1. In the theory of FEM, the essence is to represent the equation using node displacement (including vertical and angle displacements).

$$F_{joint} = F_{tensile} - F_{bending} - F_{damping} + F_{external} \tag{3.3.1}$$

The dynamic behaviour of the beam can be written in the partial differential equation as shown in Eqn. 3.3.2, where the variables $\rho, A, w, t, T, E, I, x, c$ and F respectively denote the density of the wire, the cross-sectional area of the wire, the deflection of the measured point, the time, the tensile force, the Young's modulus of the wire, the second moment of area of the wire, the axial position of the measured point, the damping coefficient and the external force.

$$\rho A \frac{d^2w}{dt^2} = T \frac{d^2w}{dx^2} - EI \frac{d^4w}{dx^4} - c \frac{dw}{dt} + F(x,t) \tag{3.3.2}$$

Based on the equation above, the FE model of the catenary wires can be constructed as shown in Eqn. 3.3.3, where $\boldsymbol{M^e}$, $\boldsymbol{C^e}$ and $\boldsymbol{K^e}$ are defined as the mass, damper and stiffness matrices for the FE model, respectively; F^e denotes the imposed external force. For the sake of brevity, the step-by-step FE-wire modelling process is presented in Appendix A.

$$\boldsymbol{M^e} * \ddot{q^e} + \boldsymbol{C^e} * \dot{q^e} + \boldsymbol{K^e} * q^e = F^e \tag{3.3.3}$$

3.3.2 Wire suspensions

The wire suspensions consist of the contact wire suspension (also referred to as 'steady arm') and the messenger wire suspension. They are important components that affect both the static and dynamic behaviour of the catenary system. Generally, if the wire suspensions are not modelled reasonably, on the one hand, the wire waves do not propagate properly through the suspension positions, while on the other hand, the wire uplift at masts when the pantograph passes through cannot be reproduced.

A variety of models of the steady arm can be used, ranging from a simple spring to detailed FE models. Collina and Bruni (2002) found that the differences in the models are mainly in the extreme values of the contact forces, where FE models predict less extreme force data near the

position of masts. In this thesis, a spring element will be used as the steady arm model because of the convenience in integrating it with the FE wire model. As long as the pantograph–catenary simulation can be validated against the EN standard for pantograph–catenary simulation, this simplification will be considered reasonable.

In this thesis (and in most other studies), the messenger wire suspension is modelled as a very stiff spring–damper system, and the mast (support) is considered to be fixed.

3.3.3 Droppers

The nonlinearity of the dropper is a critical feature of the catenary. The dropper is mainly used to achieve the desired geometry of the contact wire through connecting contact and messenger wires with different lengths. The force-displacement performance of the droppers can be found in the work of (Collina and Bruni, 2002). It shows that when the dropper is in extension, the stiffness of the dropper is approximately fixed; once it is compressed, the stiffness will quickly reduce and approach zero. This behaviour can be modelled as a spring, the stiffness of which is a piecewise function, as in Eqn. 3.3.4. Besides the dropper itself, the mass of dropper clamps on wires will be considered in the modelling.

$$k_d = \begin{cases} k_{ext} & \Delta x > 0 \;\; i.e., in\ extension \\ k_{comp} & \Delta x \leq 0 \;\; i.e., in\ contraction \end{cases} \tag{3.3.4}$$

3.3.4 Catenary geometry

The catenary geometry refers to the profile of the span length, height and dropper distribution. There are two widely used catenary geometries in modelling. The main difference between them is that one assumes that all dropper–contact wire connecting points are placed at the same vertical level by adjusting the dropper lengths, and the geometry in the other model is designed to make the wire–dropper connection points hold at different heights (this is described as pre-

sag configuration). In this thesis, the latter one will be used for the catenary modelling to allow validation against the latest version of EN 50318 and a benchmark study of pantograph–catenary simulation. The modelling and simulation results based on the former geometry using the same framework can be found in the work of (Duan et al., 2022).

3.3.5 Time integration

To simulate the dynamic behaviour of the catenary model, a method of time integration to solve the dynamic problem has to be chosen. The Newmark-beta and Alpha methods are the most widely used time integration algorithms for pantograph–catenary simulation of dynamics (Bruni et al., 2015), although in some studies, especially when the pantograph is modelled as a multibody system, some other methods are used to ensure the exchange of kinetic information between the pantograph and catenary models (Rauter et al., 2007, Ambrósio et al., 2009, Ambrósio et al., 2012a, Massat et al., 2014, Bautista et al., 2016, Kulkarni et al., 2017, Antunes et al., 2019, Ramalho et al., 2022).

In this thesis, the Newmark-beta method (Newmark, 1959) with the rule of average constant acceleration is used in solving the time integration of the FE catenary model. The iteration of the displacement and speed follow the trapezoidal rule. The derivation of the kinetic states at the next time step starts from the assumption of the average constant acceleration as expressed in Eqns. 3.3.5, 3.3.6 and 3.3.7, where $y(t)$ denotes the displacement at the current time step.

$$y(t+\Delta t) = y(t) + \frac{1}{2}[\dot{y}(t) + \dot{y}(t+\Delta t)]\Delta t \tag{3.3.5}$$

$$\dot{y}(t+\Delta t) = \dot{y}(t) + \frac{1}{2}[\ddot{y}(t) + \ddot{y}(t+\Delta t)]\Delta t \tag{3.3.6}$$

$$y(t+\Delta t) = y(t) + \dot{y}(t)\Delta t + \frac{1}{4}[\ddot{y}(t) + \ddot{y}(t+\Delta t)]\Delta t^2 \tag{3.3.7}$$

From Eqns. 3.3.6 and 3.3.7, the acceleration and speed at $t + \Delta t$ can be derived.

$$\ddot{y}(t + \Delta t) = \frac{4}{\Delta t^2}[y(t + \Delta t) - y(t)] - \frac{4}{\Delta t}\dot{y}(t) - \ddot{y}(t) \tag{3.3.8}$$

$$\dot{y}(t + \Delta t) = -\dot{y}(t) + \frac{2}{\Delta t}[y(t + \Delta t) - y(t)] \tag{3.3.9}$$

Combining Eqn. 3.3.3 at $t + \Delta t$ and Eqns. 3.3.8 and 3.3.9, the kinetic states at $t + \Delta t$ can be therefore calculated based on the kinetic states in the previous time step.

$$y(t + \Delta t) = \frac{F^e(t + \Delta t) + \left[\frac{4}{\Delta t^2}y(t) + \frac{4}{\Delta t}\dot{y}(t) + \ddot{y}(t)\right] * \boldsymbol{M^e} + \left[\frac{2}{\Delta t}y(t) + \dot{y}(t)\right] * \boldsymbol{C^e}}{\boldsymbol{K^e} + \frac{4}{\Delta t^2}\boldsymbol{M^e} + \frac{2}{\Delta t}\boldsymbol{C^e}} \tag{3.3.10}$$

$$\ddot{y}(t + \Delta t) = \frac{4}{\Delta t^2} * [y(t + \Delta t) - y(t)] - \frac{4}{\Delta t}\dot{y}(t) - \ddot{y}(t) \tag{3.3.11}$$

$$\dot{y}(t + \Delta t) = \dot{y}(t) + \frac{\Delta t}{2}\ddot{y}(t) + \frac{\Delta t}{2}\ddot{y}(t + \Delta t) \tag{3.3.12}$$

3.3.6 Summary of catenary modelling

One of the key points of modelling the catenary system accurately is to reproduce the catenary geometry and phenomenon of wire wave propagation, as they have significant impacts on the contact force simulation result. Hence, the contact and messenger wires are modelled discretely by an Euler–Bernoulli beam with the FEM. The above two features will be demonstrated in the later static and dynamic simulations.

As active pantograph design and validation, rather than precise imitation of the catenary dynamics, are the main research objective, some catenary components are simplified appropriately as long as the model can meet the requirement of the simulation standard. The

wire suspensions at masts are modelled as spring and spring–damper systems; the dropper is modelled as a nonlinear spring model whose stiffness is a piecewise function; pre-sag catenary geometry is chosen in order to validate the simulation results against the latest standard. The Newmark-beta time integration algorithm is used for dynamic simulation of the catenary model.

The parameters used for the catenary model are summarised in Table 3.3.1 and Table 3.3.2. The parameters are primarily taken from EN 50318:2018. As the stiffness of the steady arm spring model is not provided, this value was found through trial and error in simulations, which will be presented in Appendix B.2. The obtained stiffness is proved to be valid in both static and dynamic performance when validating with the standard.

Table 3.3.1. Parameters of the wires

	Contact wire	Messenger wire
Bending stiffness (Nm^2)	195	131.7
Density (kg/m)	1.35	1.07
Tension (N)	22000	16000

Table 3.3.2. Parameters of the droppers, suspensions and catenary geometry

Dropper stiffness in extension (kN/m)	[197 223 247 264 269 264 247 223 197]
Dropper stiffness in contraction (N/m)	0
Mass of one clamp on the messenger wire (kg)	0.195
Mass of one clamp on the contact wire (kg)	0.165
Steady arm stiffness (N/m)	300
Messenger wire suspension stiffness (kN/m)	500

Messenger wire suspension damping (Ns/m)	1000
Span length (m)	55
Dropper position along a span (m)	[4.5 10.25 16 21.75 27.5 33.25 39 44.75 50.5]

3.4 Interaction method (contact model)

As discussed in Chapter 2.2.3, the penalty method is a competent method and the most popular one for pantograph–catenary simulations when using an FE catenary and it is convenient for generating contact forces and identifying contact losses. By the penalty method, the contact force is obtained through Eqn. 3.4.1, where k is the coefficient for the penalty method, x_{head} is the displacement of the pantograph head and x_{wire} is the displacement of the contact wire. The coefficient k is equivalent to the stiffness of the virtual spring between the pantograph and catenary.

$$F = k(x_{head} - x_{wire}) \tag{3.4.1}$$

As also widely accepted in the literature, EN 50318 advises a coefficient of 50,000 N/m for the interaction penalty model, which will be used in this thesis.

3.5 Simulation framework and workflow

In summary, the overall system, including the models of the pantograph, catenary and their interaction, is depicted in Figure 3.5.1. Note that the geometry of the catenary system is not drawn here.

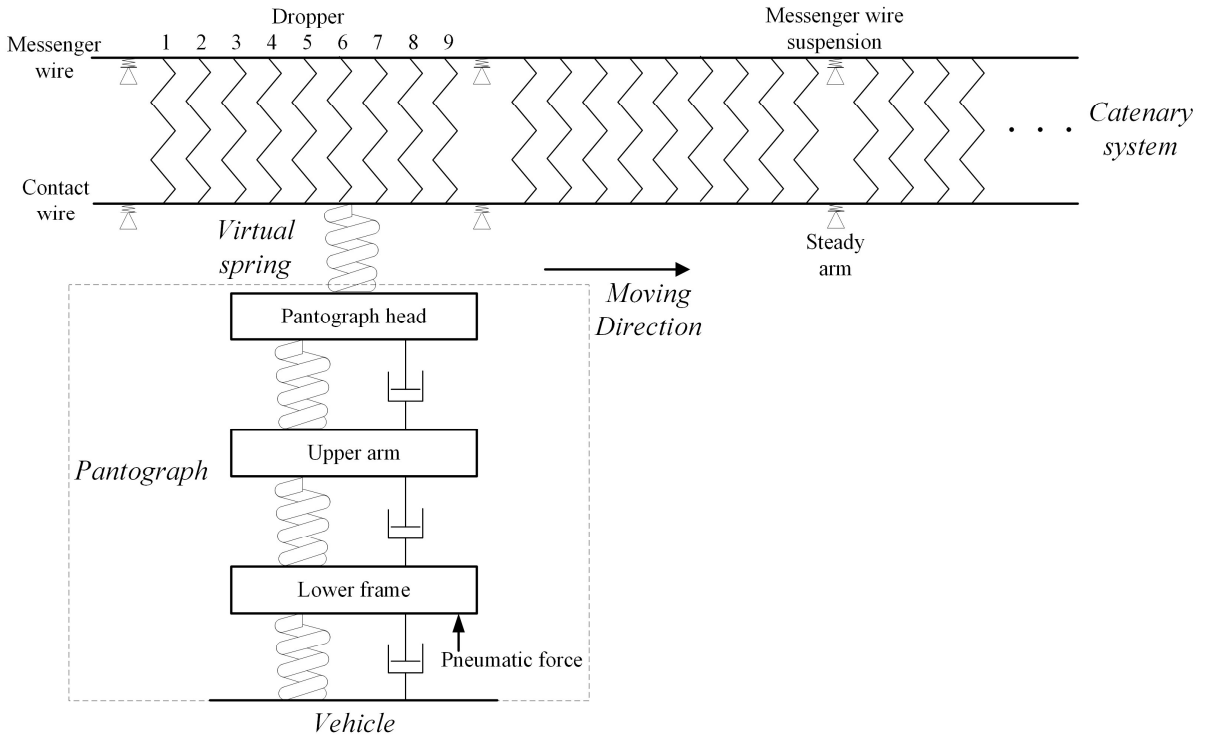


Figure 3.5.1. Modelling of the detailed pantograph–catenary system

3.5.1 Static simulation

Based on the parameters and methods given in the previous subsections, the system simulation is coded and conducted in Matlab-Simulink. Considering the complexity of the pantograph–catenary system, the workflow of how to assemble the components and find their initial conditions is elaborated in this section.

The workflow of finding the steady state of the pantograph–catenary model is presented in Figure 3.5.2 with seven steps. This is important, because by finding the steady state of the pantograph–catenary model, the initial transient disturbance effect on the dynamic simulation can be negated.

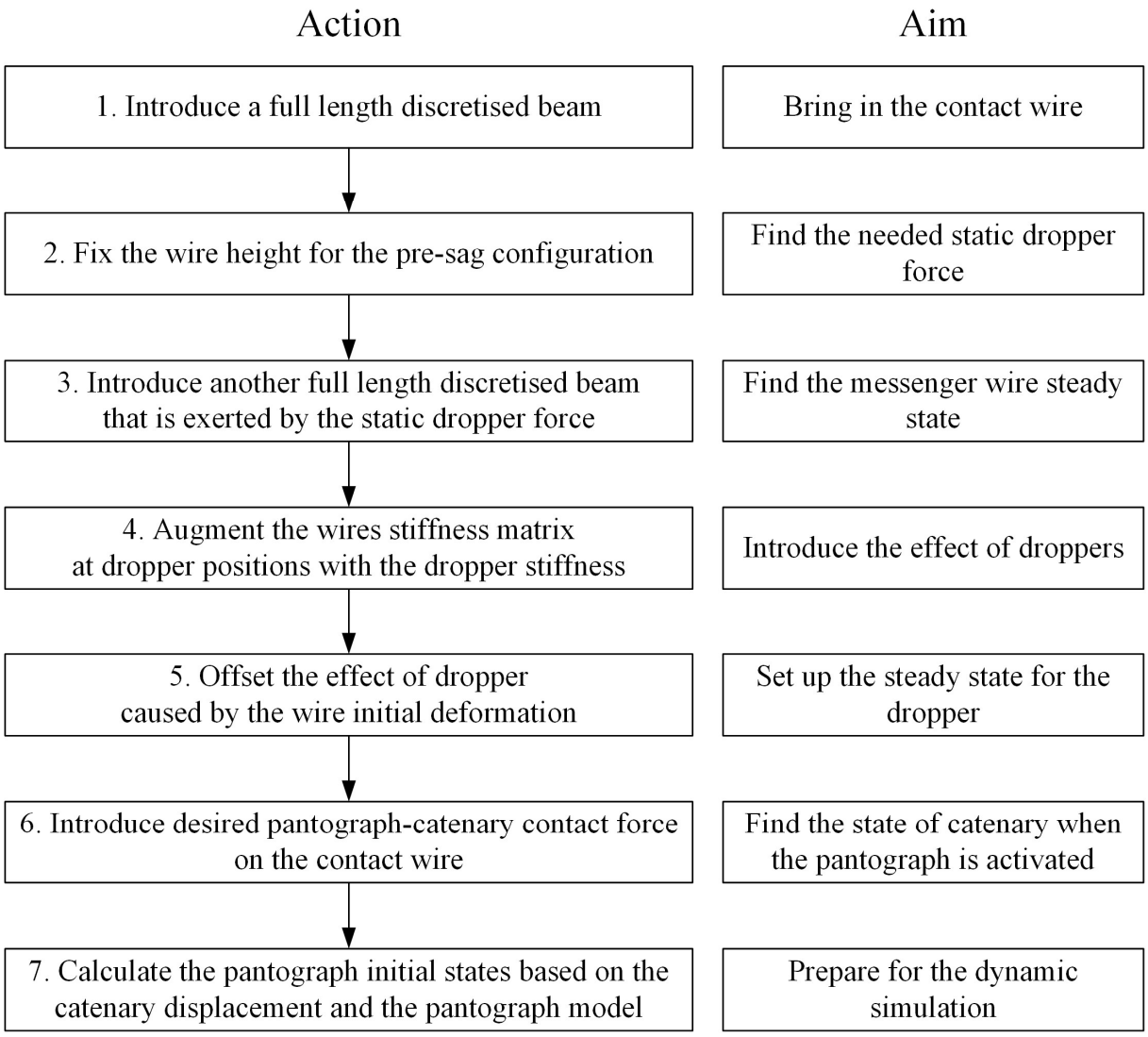


Figure 3.5.2. Workflow of assembling the components and finding initial conditions

1. The modelling starts with a full-length beam that is supposed to be the contact wire. The wire is subjected to the impacts of tension, gravity and steady arm suspension. The stiffness and mass of each discretised element are assembled.

2. The pre-sag configuration (wire geometry) is set up by placing the boundary conditions at desired (dropper) positions with desired heights. Based on the deformation in the pre-sag state, the structural force can be calculated by Eqn. 3.5.1. The required dropper force for holding this geometry can be calculated by subtracting the gravitational effect from the structural force, as in Eqn. 3.5.2. Note that the mass of clamps is also considered in this step.

$$F^e = \boldsymbol{K^e} * q^e \tag{3.5.1}$$

$$F^e_{d_ini} = F^e - F^e_{gravity} \tag{3.5.2}$$

Using the parameters in Table 3.3.1 and Table 3.3.2, the resulting contact wire vertical displacement is presented in Figure 3.5.3. The static tension force of each dropper in the central catenary span is listed in Table 3.5.1.

Table 3.5.1. Dropper force at steady state

Dropper number (In order from left to right within a span)	Dropper static force (N)
1	162.09
2	50.48
3	54.74
4	46.99
5	54.75
6	46.99
7	54.74
8	50.48
9	162.09

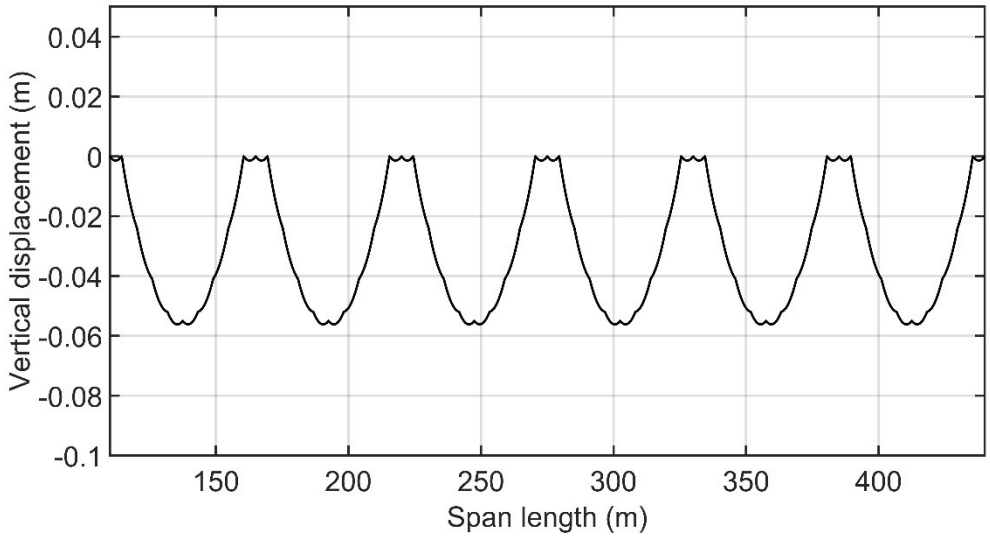


Figure 3.5.3. Vertical displacement of the contact wire at steady state

3. Another full-length beam is introduced as the messenger wire, which is subjected to the gravity, suspension, tension and initial dropper forces calculated from Eqn. 3.5.2. The vertical displacement of the messenger wire at steady state is presented in Figure 3.5.4.

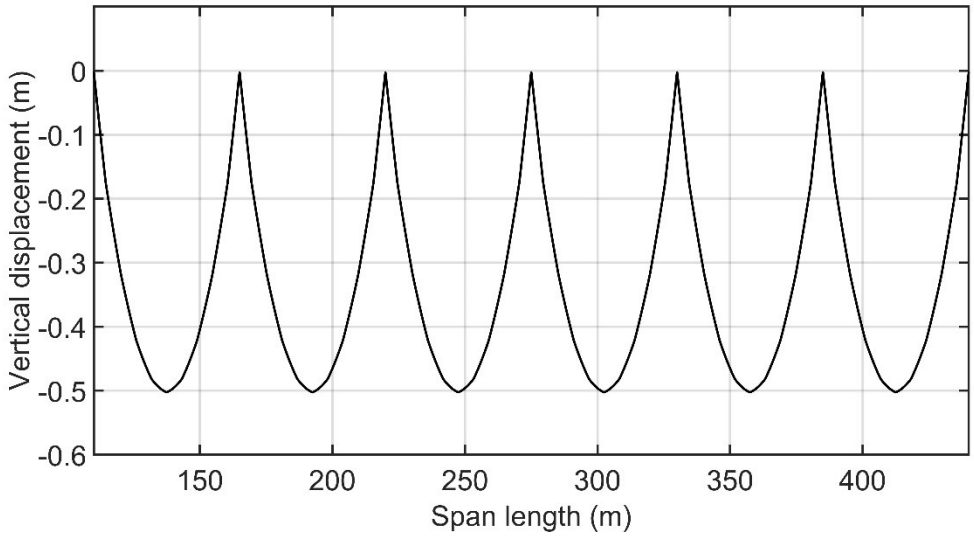


Figure 3.5.4. Vertical displacement of the messenger wire at steady state

4. The wire stiffness matrix at the dropper positions is augmented with the dropper stiffness, so that the dropper effect can be expressed through the FE stiffness matrix.

$$\boldsymbol{K^e = K^e + K_d^e} \tag{3.5.3}$$

5. As the contact and messenger wires are now configured at their steady state (displaced from the origin), the effect of the dropper stiffness matrix needs to be offset. This can be realised by introducing an external force term to cancel out the effect of dropper stiffness at steady state. Now, compared with other nodes, the dropper position is only subjected to F_{d_ini}.

$$F_{d_{offset}}^e = \boldsymbol{K_d^e} * q^e \tag{3.5.4}$$

6. The desired pantograph–catenary contact force can be applied on a desired node of the contact wire to find the steady state of the catenary system with the pantograph activated. For example, the vertical displacement of the contact under 95 N force at the point of 55 m (the first steady arm) is presented in Figure 3.5.5.

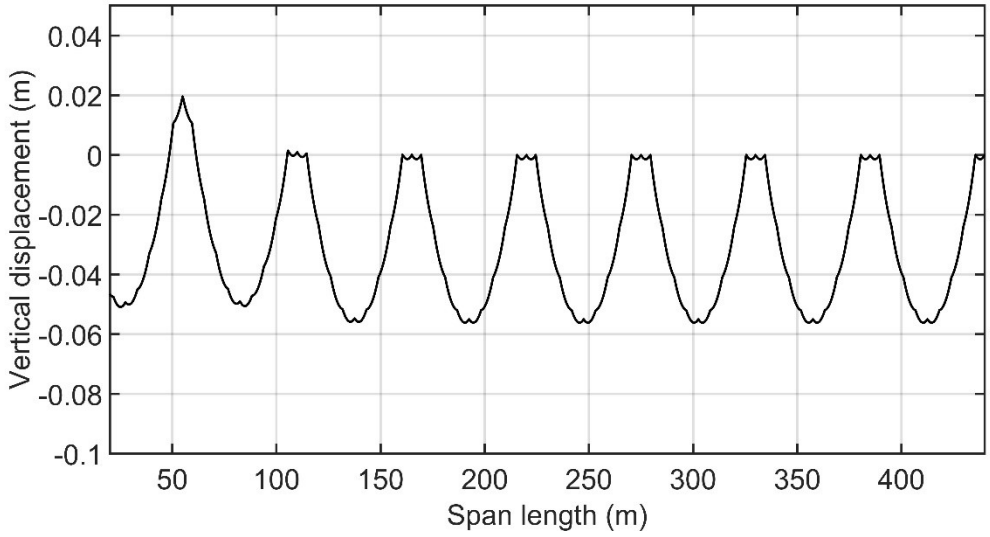


Figure 3.5.5. Vertical displacement of the contact wire under 95 N contact force

7. According to the contact wire deformation and the desired initial contact force, the steady state of the pantograph model can be calculated through its mathematical representation. With a 95 N contact force, the pantograph model's displacements of the masses are listed in

Table 3.5.2. It shows that a 101.59 N uplift force needs to be placed on the frame mass to exert the 95 N contact force.

Table 3.5.2. Steady states of the pantograph model for ensuring a 95 N contact force

Mass of the pantograph model	Displacement (m)
Frame and lower arm	0.0412
Upper arm	0.0351
Head	0.0215

3.5.2 dynamic simulation

Once the initial (static) conditions of the pantograph and catenary are found, the dynamic simulation can be conducted using the framework shown in Figure 3.5.6. At each simulation step, the contact wire height at the contact point is read from the memory that contains the kinetic information of the thousands of nodes of the catenary model at the last time step. The contact wire height is sent to the pantograph and penalty model, from which the contact force and pantograph dynamic response can be calculated. The obtained contact force is finally used to excite the catenary model, and the kinetic conditions at this time step can be derived through the time integration algorithm. The new kinetic conditions can be saved in the memory for the next simulation step.

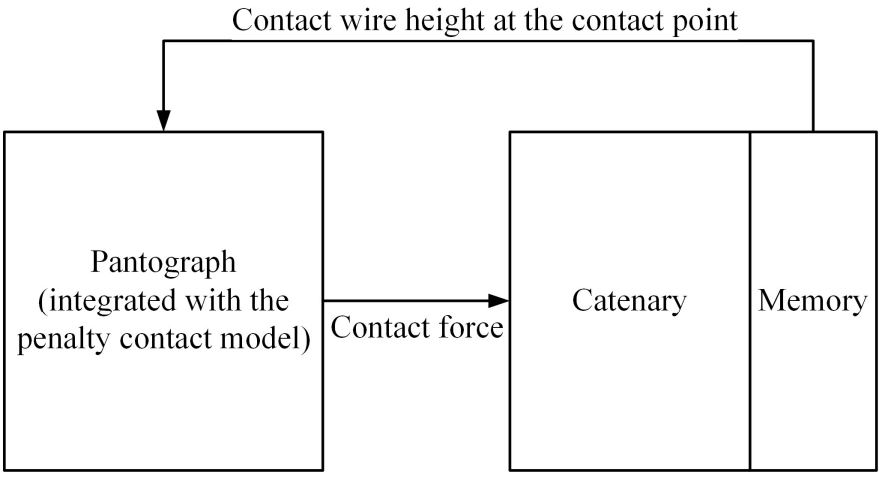


Figure 3.5.6. Overall dynamic simulation framework

The dynamics of the penalty and pantograph models are represented in state space. The time integration of the linear pantograph model is solved by ode5 in Simulink. Regarding the catenary block in Figure 3.5.6, as it must be able to represent the nonlinear characteristics of the dropper, its workflow at each time step is given as shown in Figure 3.5.7.

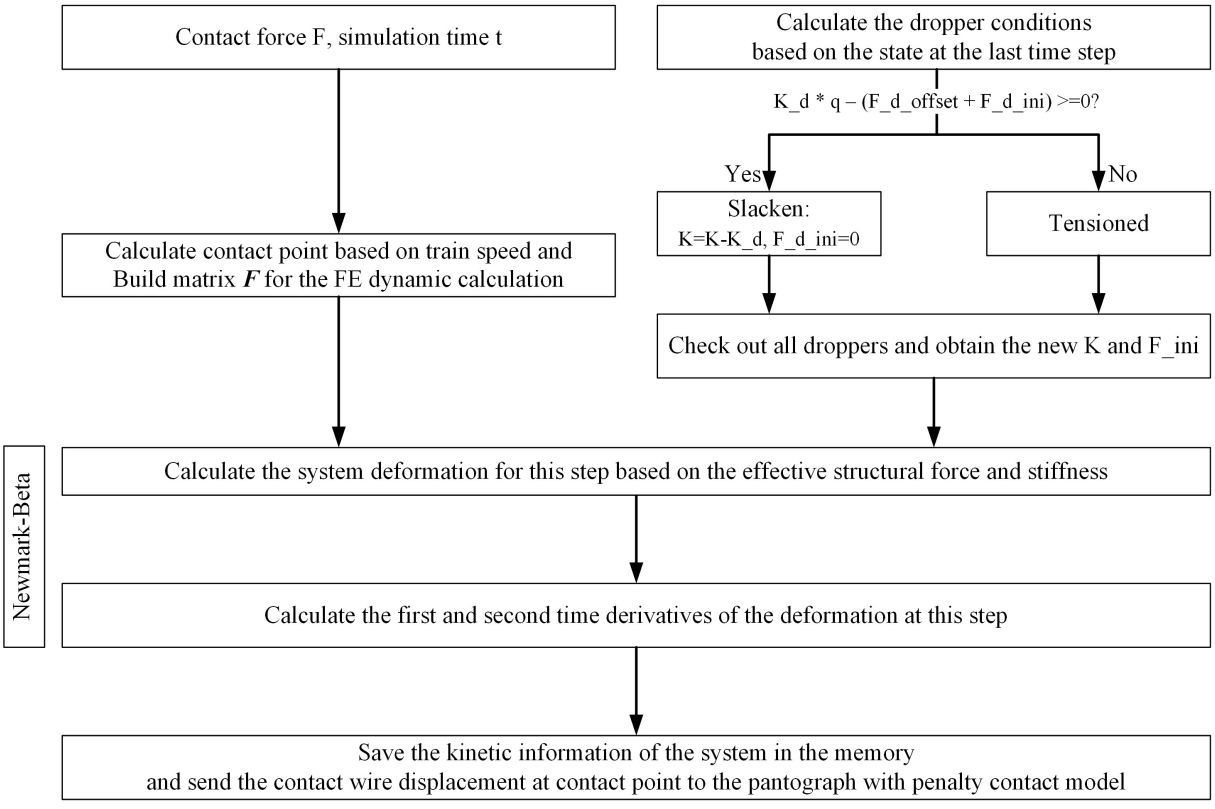


Figure 3.5.7. Catenary dynamic simulation workflow

First, the contact force and simulation time are used to build an external force matrix containing the contact point and force information. If the moving speed of the train (pantograph) is assumed to be constant, the contact point will move uniformly forward along the discrete wire. If the simulation step size is smaller than the ratio of element length to the speed, the contact will stay at each point for more than one time step, which is beneficial in delivering a smooth result considering the wire discretisation.

To represent the dropper's nonlinearity, at each time step, the dropper conditions have to be checked (as either slackened or tensioned). If slackening happens (identified by Eqn. 3.5.5), the augmented dropper stiffness $\boldsymbol{K_d^e}$ will be taken out from the system stiffness matrix $\boldsymbol{K^e}$ and the wires will not be subject to the initial dropper force $F_{d_ini}^e$. This dropper condition checking needs to be processed for all droppers at each time step, and the system stiffness and dropper force rectification may need to be conducted for each dropper.

$$\boldsymbol{K_d^e} * q^e - \left(F_{d_{offset}}^e + F_{d_{ini}}^e\right) \geq 0 \tag{3.5.5}$$

Once the external force (including the dropper force and contact force) and the system rectified stiffness are assembled, the Newmark-beta algorithm is applied to calculate the kinetic conditions of the catenary system at this time step using Eqns. 3.3.10, 3.3.11 and 3.3.12. The kinetic data will be saved in the memory for the calculation at the next time step.

3.6 Simulation validation

Before conducting the validation, some simulation parameters that have not been decided previously need to be found for the simulation. The parameters include FE meshing size (0.25 m), steady arm stiffness (300 N/m), simulation step size (0.0005 s) and the number of simulated

spans (10) and measured spans. The process of how these parameters are determined and their impacts on the simulation result is presented and analysed in Appendix B.

The developed simulation framework with the pantograph and catenary models is then validated against EN 50318:2018, the latest version of the standard for pantograph–catenary simulation. As described previously, the simple AC overhead contact line and pantograph presented in the standard are modelled. Although the active pantograph discussed in this thesis only concerns the single-pantograph operational condition, the double pantograph is simulated first in order to undertake the validation (as per the standard). The double-pantograph case is simulated to be running at 320 km/h with a 200 m interval. The pantograph (pneumatic) uplift force is set to ensure the two pantographs exert 169 N static (mean) contact forces on the contact wire.

The simulation result for a single-pantograph case is additionally compared with a benchmark study of pantograph–catenary simulation.

3.6.1 Static result

In the EN standard, two static metrics are required to be validated: the contact wire static elasticity and dropper length.

The contact wire static elasticity can be obtained by measuring the resulting displacement when applying a force on the contact wire nodes. The elasticity is expressed by the ratio of the displacement to the force (used in the EN standard) or the ratio of the force to the displacement (usually used in academic papers). As different amplitudes of the applied force can lead to different elasticity results, here, in order to comply with the standard, a 200 N contact force is applied.

The elasticity performance along a wire span is presented in Figure 3.6.1. The units here are N/m and it is shown that the elasticity in the middle of a span is generally lower than that in a section near a mast. For the model validation process, the elasticity at dropper positions is compared with the referenced value (in the units of mm/N). The comparison is presented in Table 3.6.1, and the elasticity deviation is within 0.005 mm/N (3%), which is better than the allowance.

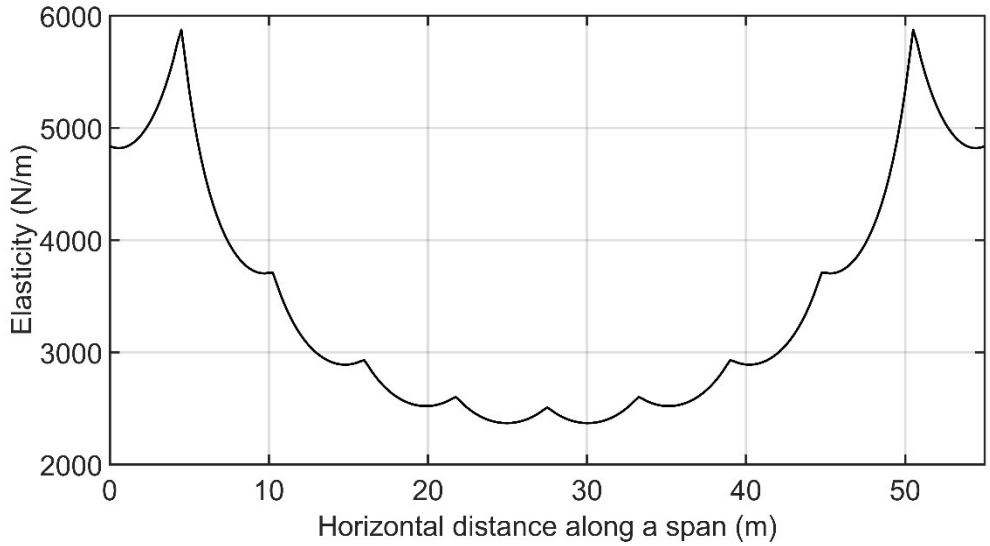


Figure 3.6.1. Static elasticity along a span when the imposed force is 169 N

The dropper length in the developed framework can be obtained by analysing the deformations of the contact and messenger wires. This can be conducted with the help of the encumbrance which is the axial distance between contact and messenger wires at masts (the referenced model has a 1.2 m encumbrance). The difference between the contact and messenger wire vertical coordinates at the dropper positions is therefore regarded as the dropper length at steady state. The obtained dropper lengths are listed in Table 3.6.1. Compared with the reference values, the dropper length is generally longer but complies with the required accuracy.

Table 3.6.1. Static result validation against EN 50318:2018

Static results		Dropper number									support	Required/obtained accuracy
		1	2	3	4	5	6	7	8	9		
Referenced	Elasticity (mm/N)	0.165	0.273	0.345	0.388	0.400	0.388	0.345	0.273	0.165	0.206	± 0.1 mm/N or ± 10% whichever is greater
	Dropper length (m)	1.023	0.902	0.815	0.764	0.747	0.764	0.815	0.902	1.023	N.A.	± 10 mm
Obtained	Elasticity (mm/N)	0.170	0.270	0.341	0.384	0.399	0.384	0.341	0.270	0.170	0.207	≤ ± 0.005 mm/N and ≤ ± 3%
	Dropper length (m)	1.023	0.908	0.823	0.773	0.755	0.773	0.823	0.908	1.023	N.A.	≤ ± 9 mm

3.6.2 Dynamic result: double pantograph

Validation of the dynamic simulation is conducted on the double-pantograph case. The whole catenary model consists of 10 spans. The pantograph is simulated to run from the start of the second span rather than the first span to mitigate the end effect of the catenary model. The numerical result is measured from the start of the 5th to the end of the 7th span (i.e. from the 5th to 8th mast). The reason for choosing this section is to ensure that the effect of the waves generated by the leading pantograph on the trailing pantograph can be included. This requires the measured section to be several spans after the running start point.

As the wires are discretised, the simulation result contains a high-frequency numerical FE error. It is advised that the frequency range of interest is from 0 to 20 Hz, so a 3-order low-pass filter with a passband of 20 Hz is designed.

The principle of the filter design is to create a low-pass filter to remove the undesired frequency components. Besides the target of a passband of 20 Hz, the filter accompanying a FE catenary model is responsible for removing the artificial error caused by FE discretisation. This error is strong and appear at high frequency that is related to the length L of the FE beam and the train (pantograph) running speed v, as shown in Eqn.3.6.1. The filter should therefore have a narrow transition width to make sure the FE error can be attenuated at the desired level.

$$f_{error} = \frac{v}{L} \tag{3.6.1}$$

A third-order low-pass filter is designed for a running speed of 200 km/h with an element length of 0.25 m. Here, f_{error} is 222.22 Hz. This filter is also compatible with higher-speed simulation cases. The state-space representation of the designed filter is presented in Eqn. 3.6.2 and its frequency response (bode diagram) is shown in Figure 3.6.2. The designed filter has a passband ripple of 0.1 dB. The filter starts to be effective from 20 Hz, and as the frequency increases, the amplitude response of the filter decreases sharply. After the FE error frequency, the filter attenuation level remains higher than 60 dB.

$$\begin{aligned} \dot{z_f} &= A * z_f + B * u_f \\ y_u &= C * z_f + D * u_f \end{aligned} \tag{3.6.2}$$

where

$$A = \begin{bmatrix} -242.969190115129 & -41384.0052445899 & -3273520.55943891 \\ 1 & 0 & 0 \\ 0 & 1 & 0 \end{bmatrix}$$

$$B = \begin{bmatrix} 1 \\ 0 \\ 0 \end{bmatrix}$$

$$C = [2.81506897463041{,}559 \quad 559.734092472278 \quad 3271882.09326326]$$

$$D = [0.000500521119672818]$$

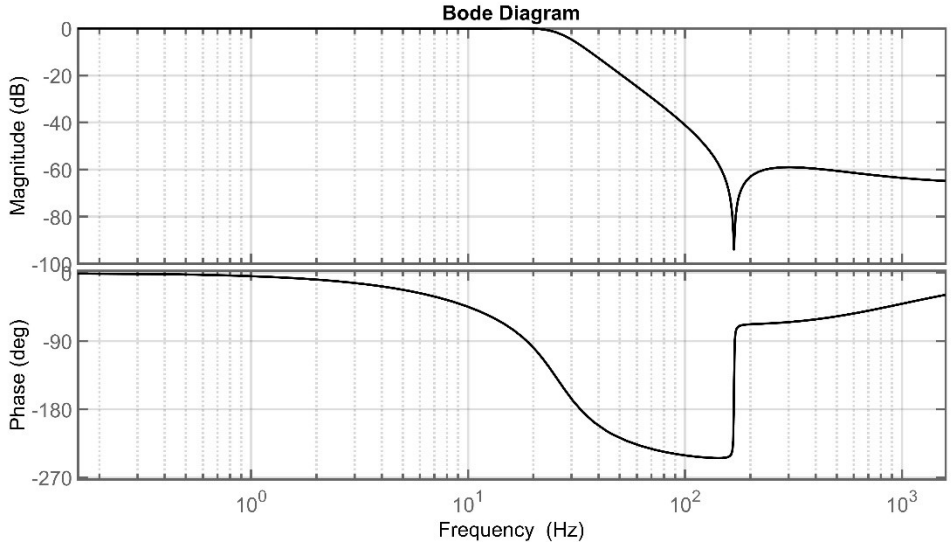


Figure 3.6.2. Frequency response of the designed filter

It should be noted that the filter is considered an integral part of the FE catenary model. Whilst it has the benefit of reducing the amplitude of the higher frequency errors, it also introduces a phase shift in the (below 20 Hz) region of interest. It is argued that whilst this effect will be seen in the results, it does not affect the findings discussed in the next chapters, which are related to the evaluation of the relative effectiveness (in simulation and application) of a simplified catenary model in the design and validation of active pantographs.

The contact force and contact wire displacement outputs for the pantographs are presented in Figure 3.6.3 to Figure 3.6.7, where the vertical dash-dot lines denote the catenary mast position. For the validation, the numerical results are listed and compared with the reference in Table 3.6.2. It can be seen that the fluctuations in contact force and displacement of the trailing pantograph are milder than for the leading pantograph. This is because the contact wire has already been excited by the leading pantograph so the effect of the catenary geometry on the

pantograph–catenary dynamic interaction is mitigated. However, because of wave propagation (which can be observed from Figure 3.6.7), the trailing pantograph is more likely to lose contact with the contact wire. It is also emphasised that the reproduction of the catenary geometry and wave propagation is important in research on the pantograph–catenary interaction, especially the double-pantograph case.

For the validation against the EN standard, all indicators fall within the required (valid) ranges. Only the maximum contact force of the leading pantograph is close to the lower bound; this is because the pantograph (pneumatic) uplift force is tuned to exert a 169 N contact force at the steady arm position. If the uplift force is tuned in the middle of a span, the uplift force will be higher and the maximum contact force will be higher in the dynamic simulation.

The framework and models have now been validated and confirmed to be appropriate for the pantograph–catenary simulation.

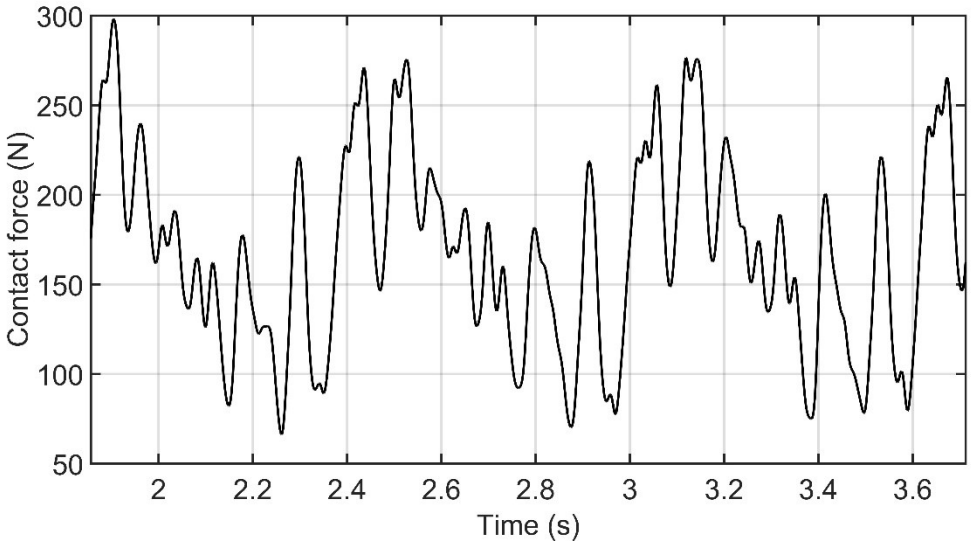


Figure 3.6.3. Contact force for the leading pantograph

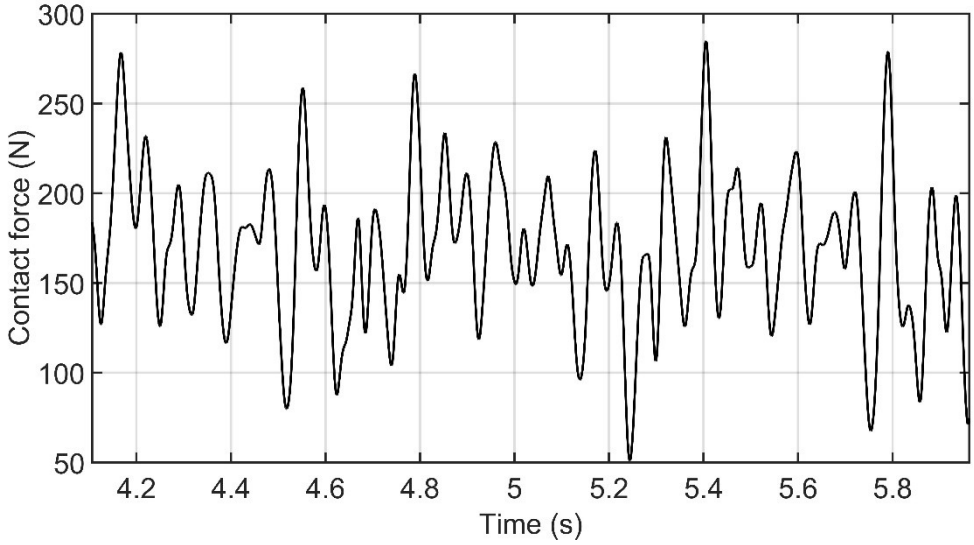


Figure 3.6.4. Contact force for the trailing pantograph

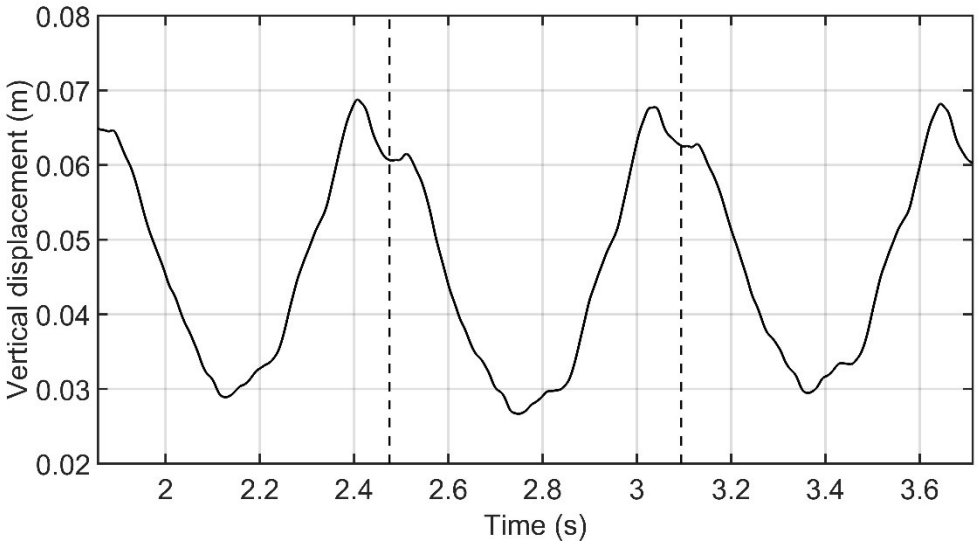


Figure 3.6.5. Contact wire displacement for the leading pantograph

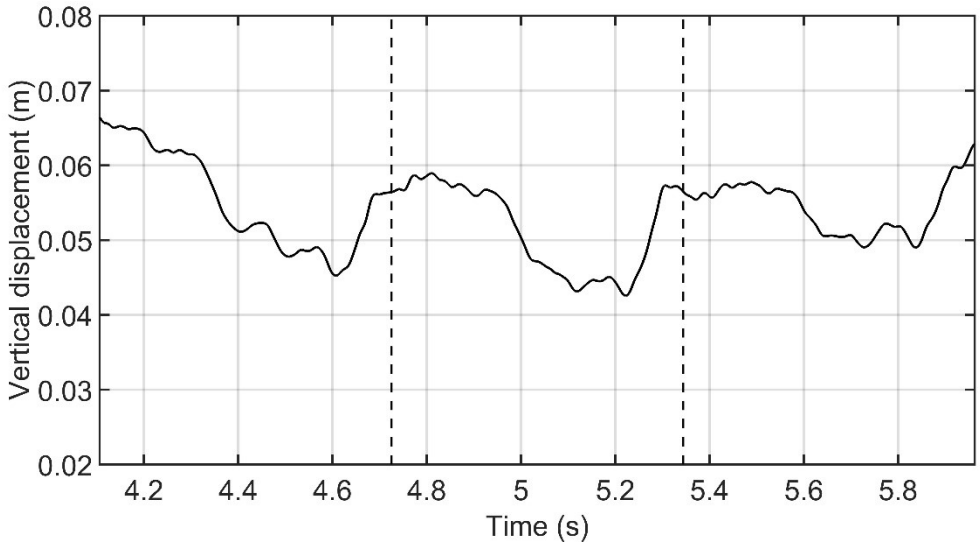


Figure 3.6.6. Contact wire displacement for the trailing pantograph

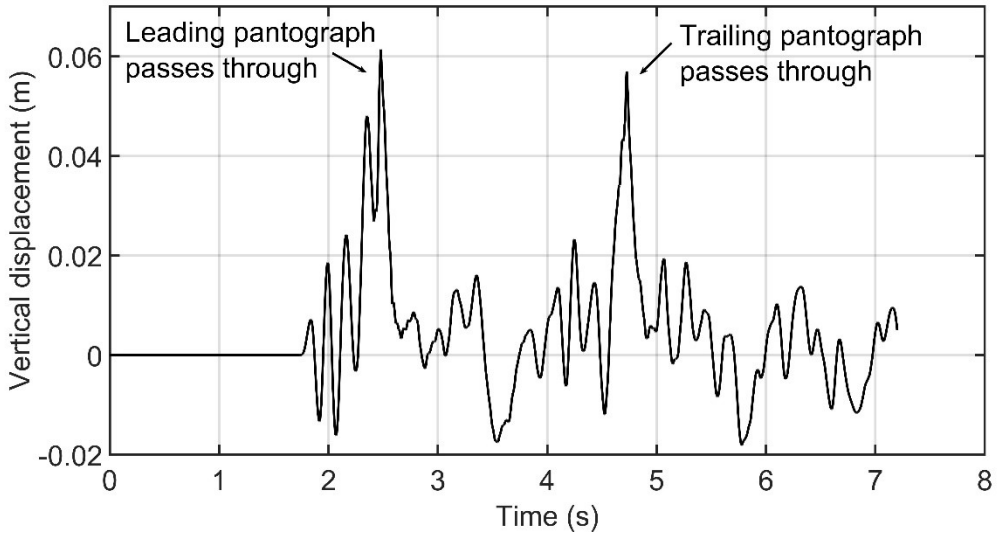


Figure 3.6.7. Contact wire uplift at the 6th mast

Table 3.6.2. Dynamic result validation against EN 50318:2018

Double pantograph	Referenced ranges		Obtained results	
Speed (km/h)	320			
Pantograph	1	2	1	2
Mean force (N)	166.5 to 171.5		168.95	168.91
Force standard deviation (N)	49.5 to 62.9	30.2 to 43.8	54.15	41.55
Force standard deviation (0 to 5Hz)[1] (N)	38.7 to 44.4	14.3 to 23.3	39.47	17.88
Force standard deviation (5 to 20Hz) (N)	29.0 to 46.2	26.7 to 38.2	36.33	35.48
Maximum of contact force (N)	295 to 343	252 to 317	297.96	284.84
Minimum of contact force (N)	55 to 82	21 to 86	66.34	51.10
Peak-to-peak of the contact point (mm)	39 to 51	18 to 35	42.09	23.85
Maximum uplift at support (mm)	57 to 64	50 to 61	61.42	56.96

[1] The banded force is filtered using a minimum-order filter that has a 0.99 filter Steepness and 60 dB attenuation level.

3.6.3 Dynamic result: single pantograph

As the active pantograph will be designed for the single-pantograph case in this thesis, the simulation result of the single-pantograph case is presented in this section. The measured section for the single pantograph is extended to seven spans, from the start of the 3rd to the end of the 9th span (i.e., from the 3rd to 10th mast), to avoid the end effect and initial settling effect. The time history graphs of the contact force, contact wire and uplift at the 6th mast are presented in Figure 3.6.8 to Figure 3.6.10.

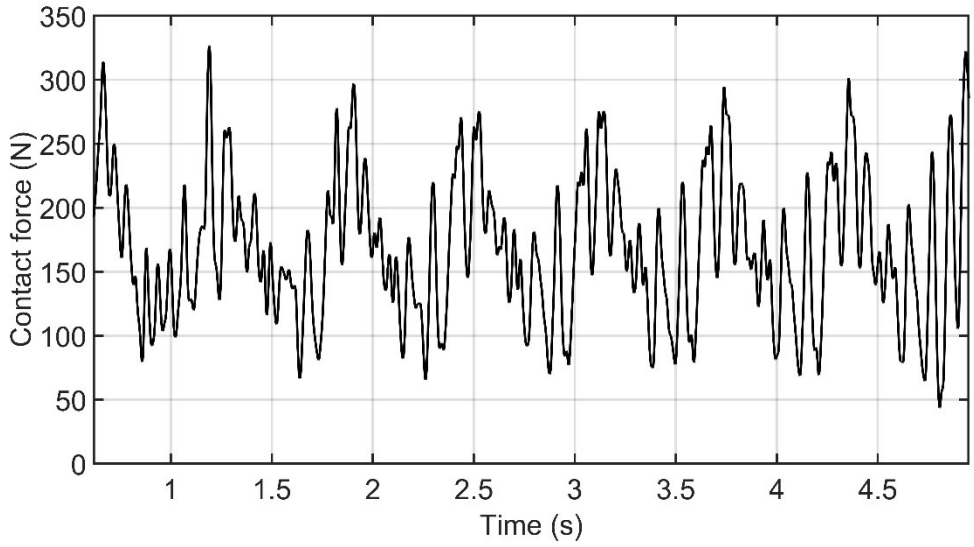


Figure 3.6.8. Contact force for the single-pantograph case

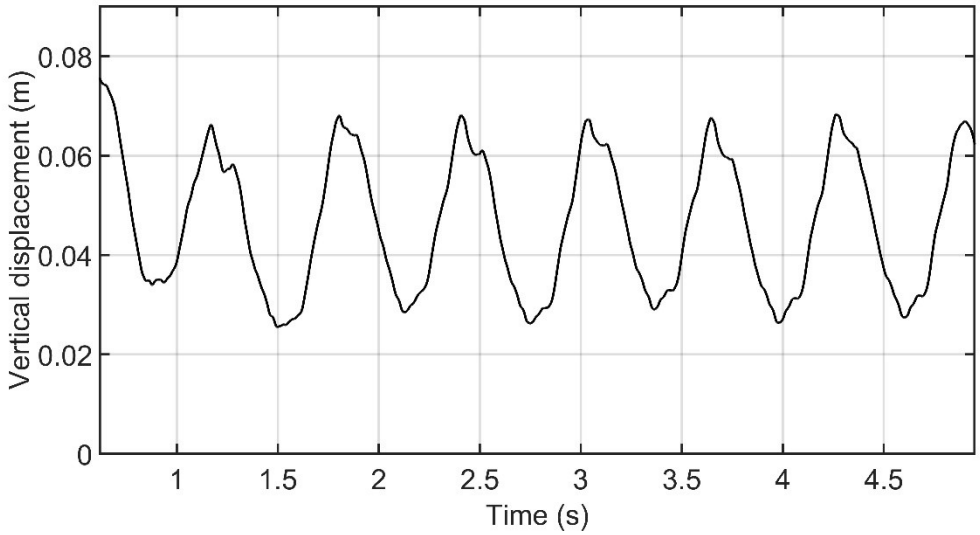


Figure 3.6.9. Contact wire displacement for the single-pantograph case

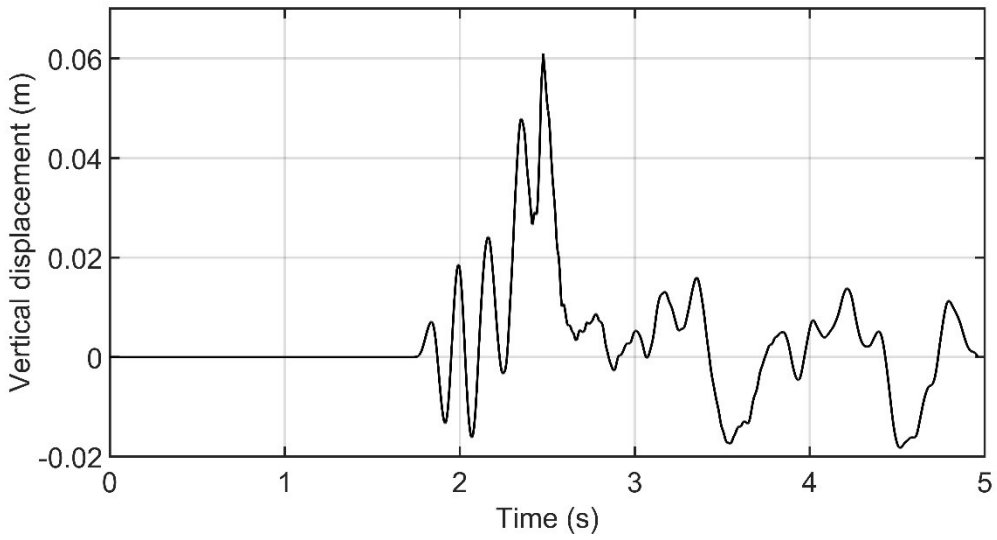


Figure 3.6.10. Contact wire uplift at the 6th mast for the single-pantograph case

Although the reference range for the single-pantograph case is not indicated in EN 50318:2018 (the industry standard), considering the fact that the validation criteria in the EN standard refer to the benchmark study (Bruni et al., 2015), the result for a single pantograph presented in the benchmark can be compared with the previous single-pantograph simulation result. A comparison of the numerical results is listed in Table 3.6.3. All of the obtained numerical results lie within one standard deviation of the benchmark results, which demonstrates that the proposed framework is able to deliver results that have good agreement with the other simulation codes.

Table 3.6.3. Single-pantograph dynamic result compared with the benchmark

Single pantograph	Benchmark Results		Obtained results	
	Mean	Standard deviation	Value	Deviation
Speed (km/h)	320			
Force standard deviation (N)	53.9145	15.4%	56.2687	4.4%
Force standard deviation (0 to 2Hz) (N)	38.2675	5.5%	37.3001	2.6%
Force standard deviation (0 to 5Hz) (N)	41.0387	4.3%	39.7322	3.2%
Force standard deviation (5 to 20Hz) (N)	34.7957	35.6%	45.4486	30.6%
Maximum of contact force (N)	313.2245	10.3%	326.2222	4.1%
Minimum of contact force (N)	60.4004	31.6%	43.7494	27.6%
Peak-to-peak of the contact point (mm)	47.5775	10.0%	42.8407	10.0%
Maximum uplift at support (mm)	59.1232	5.4%	61.0005	3.2%

3.7 Summary and Conclusion

In this chapter, a pantograph–catenary model was developed where the pantograph was modelled as a three-mass linear system; the catenary system was modelled through the FE; the penalty method was used to act in between pantograph and catenary models and generate a contact force. To simulate the static and dynamic responses of the above model, a simulation framework was developed and coded in Matlab-Simulink. The static result (initial condition) of the pantograph–catenary system can be obtained step by step, from the order of introducing the contact wire, messenger wire and droppers, to the pantograph. The dynamic simulation of the pantograph–catenary system is realised by a moving contact point on the contact wire. The deformation state of each dropper is checked at every time step.

Using the datasheets of the referenced pantograph and catenary systems, the result of the developed pantograph–catenary model from the simulation framework was compared with the EN standard and a benchmark study. It has shown that all metrics of interest fall within the required ranges in both static and dynamic simulations. Hence, the framework and models are now validated and confirmed to be appropriate for the pantograph–catenary simulation. In addition, the impacts of some simulation parameters on the contact force result were analysed and discussed.

The simulation result obtained from the developed framework will serve as a source of truth for the pantograph–catenary interaction behaviour. The result will be used for the parameterisation of a linear catenary model (in Chapter 4.2.2); the design of the proposed disturbance-observer-based (DO-based) catenary model (in Chapters 4.3 and 6.4); the veracity evaluation for the DO-based catenary model in open-loop (in Chapter 4.3) and closed-loop (in Chapters 4.3 and 5); and the validation of the hardware-in-the-loop (virtual catenary) design (in Chapter 6.5).

CHAPTER 4 DISTURBANCE-OBSERVER-BASED CATENARY MODEL FOR ACTIVE PANTOGRAPH VALIDATION

4.1 Introduction

As mentioned in the literature review, since active control designs mostly rely on linear and time-invariant models, the pantograph–catenary system is usually simplified as a linear system for active pantograph design. Once a controller is designed, the active pantograph will need to be validated with complex models that can represent the real dynamic behaviour (such as an FE catenary model). However, as it may take several hours to run in simulation, an FE catenary model is not convenient for testing active pantograph designs. Hence, researchers focused on active pantographs prefer a time-varying lumped-mass catenary model for controller validations.

However, some notable issues can be found in the literature; the most critical one is that assessment of the effectiveness of controllers validated with a time-varying lumped-mass catenary model is sometimes more optimistic than for results with an FE model. Certainly, if the control effectiveness obtained from a model deviates significantly from a detailed model or real situation, the model needs to be used with caution until the deviation is fully understood and rectified.

In this chapter, to avoid using the classic time-varying lumped-mass catenary model and improve the trustworthiness of active pantograph validation, a novel disturbance-observer

(DO)-based model is proposed. The new model aims to achieve good accuracy with fast computational speed in active pantograph validation.

As the proposed DO-based model is designed on top of the linear model and proposed to replace the role of the classic time-varying lumped-mass catenary model, the linear and classic time-varying models are introduced and discussed in Chapter 4.2. In Chapter 4.3, the development of a DO-based catenary is proposed, and its open-loop (passive pantograph) result is compared with that of the FE catenary model (the source of truth). In Chapter 4.4, the DO catenary model's performance in a closed loop is demonstrated where a PID controller is designed and simulated as an example.

It should be noted that as the physical pantograph that will be used in the hardware-in-the-loop experiment is designed for the British Rail Class 390 Pendolino high-speed train with a design service maximum of 200 km/h (Knight, 1998), the simulation from this point is conducted at a train speed of 200 km/h.

4.2 Linear and classic time-varying lumped-mass catenary models

4.2.1 Linear catenary model for active pantograph design

When a pantograph (train) is running in contact with the catenary, the contact wire will be vertically displaced due to the contact force. This behaviour can be approximately represented by a mass–spring–damper system, so the catenary system can be linearised as a second-order system for the controller design. Eqn. 4.2.1 is the dynamic equation of the linearised catenary model, where x, m_c, c_c, k_c and F are the model displacement, mass, damping, stiffness and pantograph–catenary contact force, respectively.

$$m_c\ddot{x} = c_c * \dot{x} + k_c * x + F \tag{4.2.1}$$

Consequently, combining the linearised pantograph and catenary models, the complete linear pantograph–catenary model is presented in Figure 4.2.1 (the penalty contact model is used to ensure consistency when comparing the simulation result with the FE catenary). The model's representation in state space is given in Eqn. 4.2.2, where k_1, k_2, k_3, c_1, c_2, c_3, m_1, m_2 and m_3 are the spring, damper and mass coefficients of the pantograph lower frame, upper arm, head, respectively; k_4 is the penalty interaction coefficient; m_c, k_c and c_c are the linearised mass, damper and stiffness of the catenary; the system states x_1, x_3, x_5 and x_7 denote the mass displacements and x_2, x_4, x_6 and x_8 denote the mass velocities; system input u is the pantograph uplift force and the output y is the pantograph–catenary contact force.

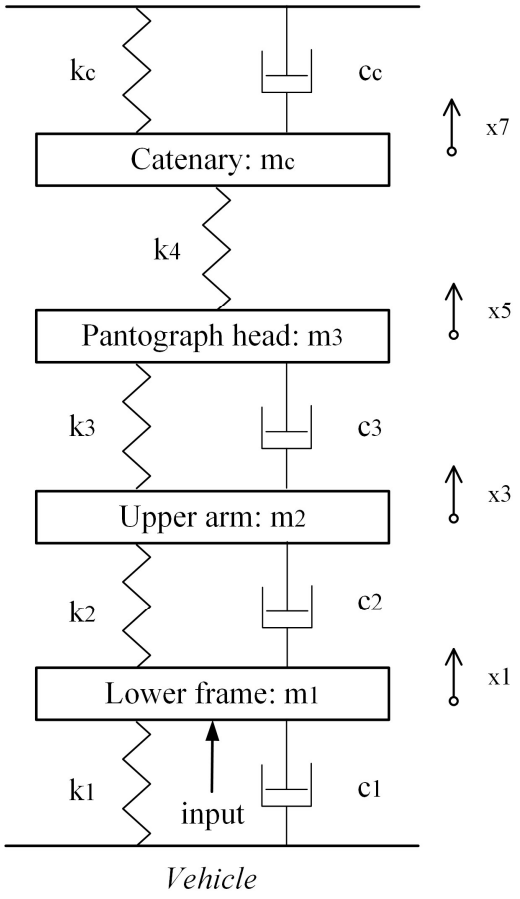


Figure 4.2.1. Linear pantograph–catenary model

$$\dot{x} = Ax + Bu \qquad y = Cx + Du \tag{4.2.2}$$

Where

$$x = [x_1 \quad x_2 \quad x_3 \quad x_4 \quad x_5 \quad x_6 \quad x_7 \quad x_8]^T$$

$$A = \begin{bmatrix} 0 & 1 & 0 & 0 & 0 & 0 & 0 & 0 \\ -\frac{(k_1+k_2)}{m_1} & -\frac{(c_1+c_2)}{m_1} & \frac{k_2}{m_1} & \frac{c_2}{m_1} & 0 & 0 & 0 & 0 \\ 0 & 0 & 0 & 1 & 0 & 0 & 0 & 0 \\ \frac{k_2}{m_2} & \frac{c_2}{m_2} & -\frac{(k_2+k_3)}{m_2} & -\frac{(c_2+c_3)}{m_2} & \frac{k_3}{m_2} & \frac{c_3}{m_2} & 0 & 0 \\ 0 & 0 & 0 & 0 & 0 & 1 & 0 & 0 \\ 0 & 0 & \frac{k_3}{m_3} & \frac{c_3}{m_3} & -\frac{(k_3+k_4)}{m_3} & -\frac{c_3}{m_3} & \frac{k_4}{m_3} & 0 \\ 0 & 0 & 0 & 0 & 0 & 0 & 0 & 1 \\ 0 & 0 & 0 & 0 & \frac{k_4}{m_c} & 0 & -\frac{(k_4+k_c)}{m_c} & -\frac{c_c}{m_c} \end{bmatrix}$$

$$B = \begin{bmatrix} 0 & \frac{1}{m_1} & 0 & 0 & 0 & 0 & 0 & 0 \end{bmatrix}^T$$

$$C = [0 \quad 0 \quad 0 \quad 0 \quad k_4 \quad 0 \quad -k_4 \quad 0] \qquad D = 0$$

4.2.2 Parameterisation of the linear catenary model

It is found in the literature (as mentioned in Chapter 2.2.4) that the coefficients of the lumped-mass catenary model are very inconsistent. As the parameters of the lumped-mass catenary model are critical to its dynamic behaviour and thus modelling accuracy, in this section, a system-identification-based method is proposed to parameterise the linear lumped-mass catenary model, aiming to reproduce the dynamic behaviour of the FE catenary.

System identification is an efficient tool to estimate unmodelled systems through the input and output signals of the experimental data. By optimising the variables of a particular model structure, the estimated model can fit the reference output with the input through a cost function. A typical cost function shown in Eqn. 4.2.3 is used in this thesis.

$$J = \sum_{t=0}^{t_N} e(t) \times e(t)$$
$$e(t) = y_{ref}(t) - y_{sim}(t) \tag{4.2.3}$$

As the contact force is the result of interest, and it is calculated through displacement of the contact wire (and pantograph head), the principle of parameterising the lumped-mass catenary is to reproduce the contact wire behaviour of a real or FE catenary. Hence, the reference input and output are the contact force excited on a catenary and the resulting contact wire displacement, respectively. To reflect the impact of the contact wire height variation, the relative contact wire displacement is considered. The relative contact wire displacement is the relative vertical displacement of the contact wire (point) against its static vertical height. Note that, when the pantograph is moving, the contact wire dynamic behaviour is essentially the contact point dynamic behaviour.

The parameterisation task now is interpreted as finding a mass–spring–damper model subject to the reference input (contact force) that can behave mostly close (defined by Eqn. 4.2.3) to the referenced output (relative displacement). The reference signals are obtained from the pantograph simulation framework with the lumped-mass pantograph and FE catenary models developed in Chapter 3.

Reasonable bounds are defined for the optimisation, and the resulting identified parameters are summarised in Table 4.2.1, which will be used for later simulations. The relative displacement of the estimated catenary model subject to the reference input is presented in Figure 4.2.2. Compared with the reference output, it can be seen that low-frequency displacement can be generally reproduced, but the high-frequency components are missing due to the limitation of the second-order plant. It can be expected that the linear model estimated using system

identification can approximately behave, and thus generate contact force, similar to the FE catenary.

Table 4.2.1. Constraint and result of parameter identification for a running condition

Lumped-mass model coefficient	Minimum value	Maximum value	Estimated value
Mass (kg)	1	200	99.66
Damper (Ns/m)	1	300	144.92
Spring (N/m)	1000	6000	2736

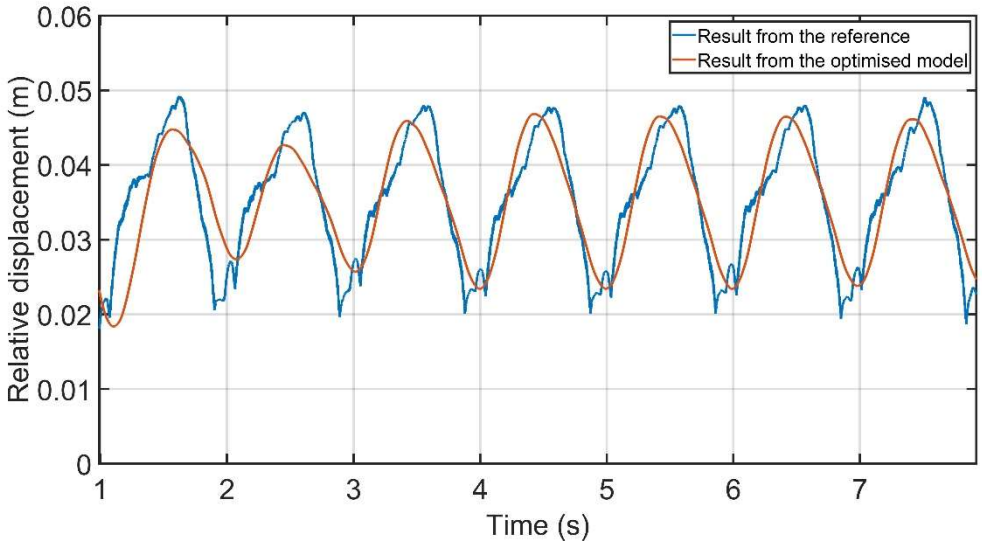


Figure 4.2.2. Relative displacement of contact wire with FE and estimated catenary models

4.2.3 Classic time-varying catenary model for active pantograph validation

As mentioned in Chapter 2.2.2, the classic time-varying catenary model, which is designed on top of the linear mass–spring–damper system, is popular for active pantograph validation. The key idea of this classic approach is to use a pre-defined spatially varying spring to represent the variation in stiffness along a catenary span. The spatial (time)-varying stiffness can be found offline through a line test or static simulation from the FE catenary model.

A spatially varying stiffness result for the developed FE catenary has been obtained in Chapter 3.5.1 (where the nominal imposed force is 169 N). However, the value of the spatially varying stiffness varies with the contact force imposed and the simulated train speed has been changed from 320 km/h to 200 km/h. Hence, the nominal contact force is changed and assumed to be 95 N (according to EN 50367 (BSI, 2012), the allowable range of the mean contact force for the 200 km/h is from 78.8 to 108.8 N). The static stiffness calculation is re-performed with the imposed force of 95 N and the result is shown in Figure 4.2.3 (it has been converted from spatially varying to time-varying).

Alternatively, an empirical mathematical representation of the time-varying stiffness can be used, as described in Chapter 2.2.2. Based on Eqn. 2.2.3, the time-varying stiffness obtained from the empirical method is compared with the static FE simulation. It is shown that the impact of droppers on the stiffness cannot be represented by the empirical method. Therefore, it is recommended that the empirical function should be used carefully.

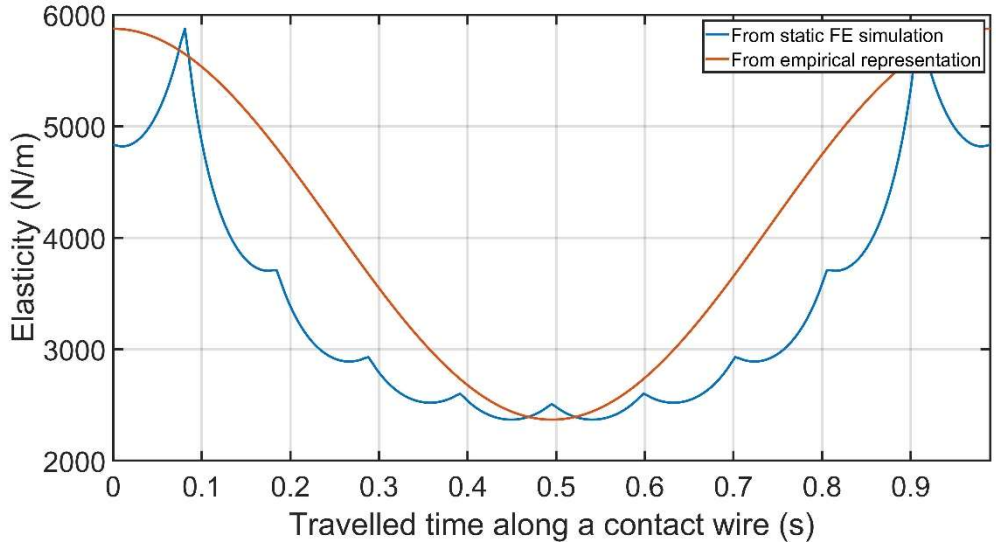


Figure 4.2.3. Static elasticity along a span when the imposed force is 95 N

Besides the stiffness variation, the lumped-mass catenary model is responsible for representing the height variation. This is critical when the catenary has a pre-sag geometry, where the catenary structure is designed to make the wire-dropper connection points hold at different heights. The height variation for the developed FE catenary model is presented in Figure 4.2.4.

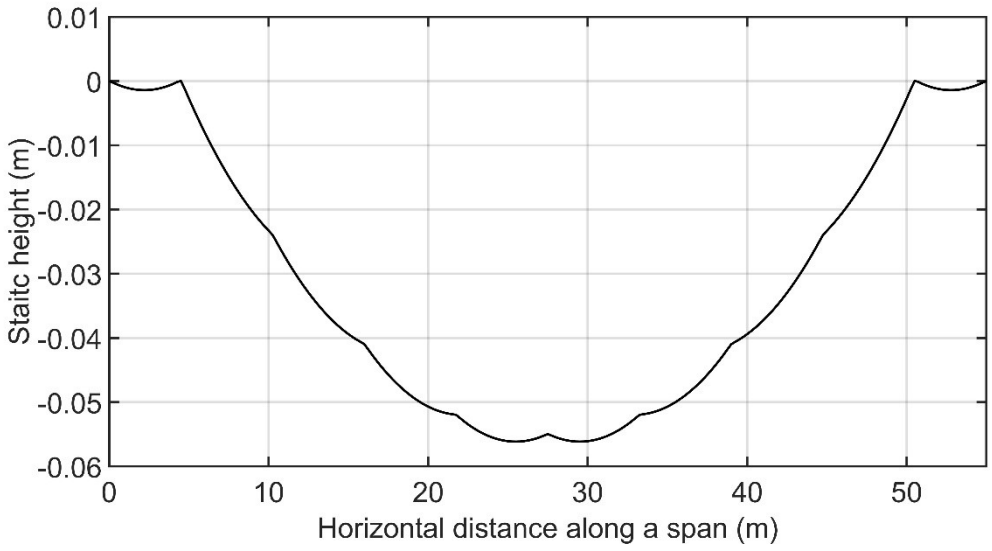


Figure 4.2.4. Height variation of the FE catenary model (pre-sag)

The static height variation can be incorporated into the catenary model included by offsetting its impact. When the pantograph travels along a contact wire section where the height is falling, the model is considered to be offset by a downward force that is a product of the height and stiffness on the catenary mass, and vice versa. The spatially varying offset force for the developed FE model is presented in Figure 4.2.5.

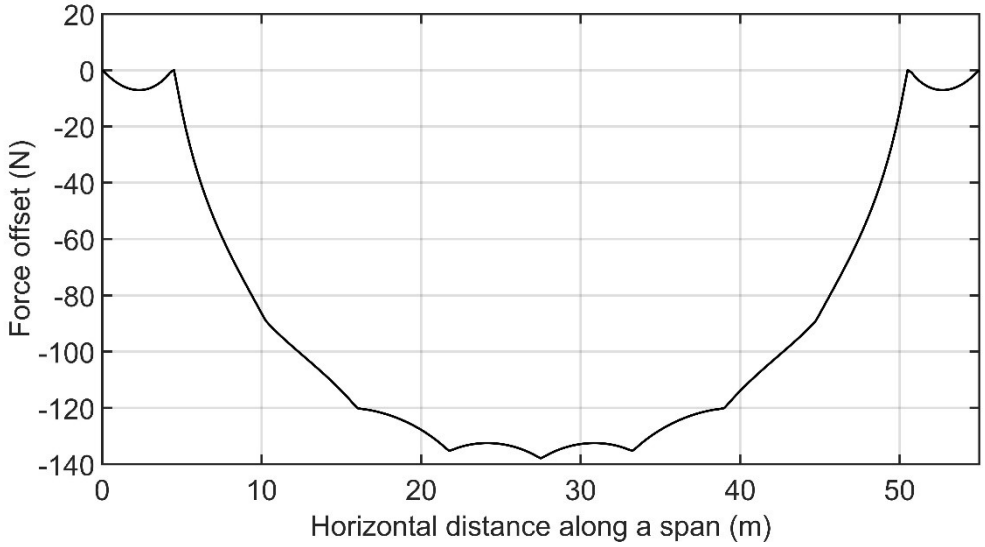


Figure 4.2.5. Spatially varying offset force against the gradient change

With the time-varying height force offset and stiffness, the classic time-varying lumped-mass catenary can be simulated. Figure 4.2.6 and Table 4.2.2 compare the contact force result between the classic time-varying lumped-mass and FE catenary models. It can be seen that the error of contact force to the FE catenary is remarkable (the R-squared is -1.5187). The high-frequency components are missing and the low-frequency components are not accurate, which results in the contact force fluctuating less and having a smaller peak range. The main reason for the error is that the time-varying parameters, the source of system disturbance in the classic lumped-mass model, are obtained on the condition that the vehicle is stationary, but in an FE (or physical) catenary, the parameters are dynamically changed.

To improve the accuracy of the lumped-mass catenary, a novel DO-based model will be proposed in the next subsection.

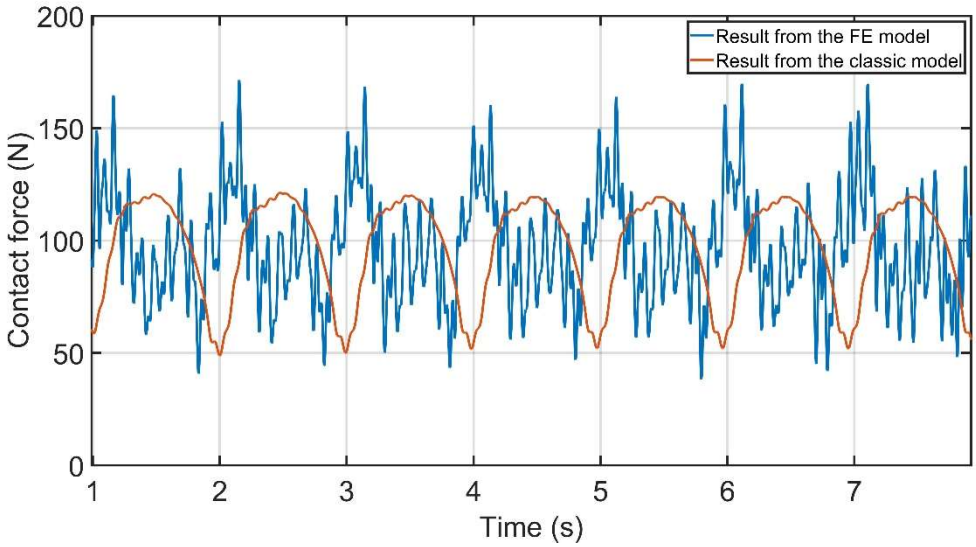


Figure 4.2.6. Contact force result of the classic model

Table 4.2.2. Numerical result of the classic model

Contact force	Classic model	FE model
Mean (N)	97.31	97.34
Standard deviation (N)	22.01	24.24
Minimum (N)	48.82	38.31
Maximum (N)	121.26	171.38
R^2 (coefficient of determination)	-1.5187	

4.3 DO-based lumped-mass model

As demonstrated in the previous subsection, for a lumped-mass catenary, the classic way of representing catenary perturbation (the variation in physical states due to the train's movement) is using time-varying parameters. However, it has been found that there are remarkable differences in the simulation results between the classic lumped-mass and FE catenary models because the time-varying parameters are not only incomplete but also inaccurate in representing the system disturbance. Therefore, extracting the source of system disturbance (which is

dynamics-based) and augmenting it on the nominal linear catenary model are considered, so that the disturbance on the lumped-mass catenary can be fully reproduced.

To extract the dynamics-based disturbance information, a DO is used. The DO assumes that a linear model is subject to an external signal which is a lumped disturbance consisting of system nonlinearity, parameter perturbation and external interference on the nominal linear system. Generally, as shown in Eqn. 4.3.1, a system represented in state space with a pair of (A, B, C, D) is augmented with a disturbance state d, where the matrix E is determined by how the defined disturbance impacts the system.

$$\begin{aligned} \begin{bmatrix} \dot{x} \\ \dot{d} \end{bmatrix} &= \begin{bmatrix} A & E \\ 0 & 0 \end{bmatrix} \begin{bmatrix} x \\ d \end{bmatrix} + \begin{bmatrix} B \\ 0 \end{bmatrix} u \\ y &= \begin{bmatrix} C & 0 \end{bmatrix} \begin{bmatrix} x \\ d \end{bmatrix} + Du \end{aligned} \tag{4.3.1}$$

The disturbance state d can be estimated by a state observer through the input and output of the system. For the above linear system, a linear Luenberger observer is designed as in Eqn. 4.3.2, where the hat notation denotes the estimated state. According to Eqn. 4.3.3, the gain L is tuned to stabilise the observer with the required bandwidth, so that the observer error $e(t) \to 0$ when $t \to \infty$.

$$\begin{aligned} \begin{bmatrix} \dot{\hat{x}} \\ \dot{\hat{d}} \end{bmatrix} &= \begin{bmatrix} A & E \\ 0 & 0 \end{bmatrix} \begin{bmatrix} \hat{x} \\ \hat{d} \end{bmatrix} + \begin{bmatrix} B \\ 0 \end{bmatrix} u + L(y - \hat{y}) \\ \hat{y} &= \begin{bmatrix} C & 0 \end{bmatrix} \begin{bmatrix} \hat{x} \\ \hat{d} \end{bmatrix} + Du \end{aligned} \tag{4.3.2}$$

$$\begin{aligned} \dot{e} &= (A - LC)e \\ e &= x - \hat{x} \end{aligned} \tag{4.3.3}$$

The assumption in Eqn. 4.3.1 that the differential of the disturbance is zero (i.e., $\dot{d} = 0$) is only used to facilitate estimation of the disturbance via the DOB (i.e., for the observer design). It is

explained in (Sariyildiz et al., 2019b) and references therein that, a DOB, can precisely estimate disturbances by using very simple dynamic models. For example, a constant disturbance model is generally used and found effective for estimating not only constant, but also variable disturbances in practice.

It is true that with the minimum order DOB, asymptotic stability of disturbance estimation cannot be achieved when $\dot{d} \neq 0$. The estimation error e_{dis} is bounded by the equation below, where λ_{min} is the bandwidth of DOB and $\dot{\delta}$ is the upper bound of the first derivative of the disturbance (Sariyildiz et al., 2019a). The equation shows that the convergence rate and the accuracy of disturbance estimation can be improved simply by increasing the observer gain.

$$\|e_{dis}(t)\| \leq exp(-\lambda_{min}t)\|e_{dis}(t_0)\| + \lambda_{min}^{-1}\dot{\delta} \tag{4.3.4}$$

In the thesis, the DOB bandwidth is more than doubled the frequency of interest to reduce the observer error, but error can still be found in the simulation results. From Figure 4.3.3 in the later simulation, it can be seen that the DO-based catenary cannot perfectly, but can well imitate the high-frequency (10-20 Hz) behaviour of the FE catenary due to DO error. An example of using a second-order DOB to precisely estimate the second derivative of the disturbance with a high bandwidth can be found in (Sariyildiz et al., 2019a). Although it uses a higher-order DOB, the concept is the same.

To estimate the disturbance for the catenary model in Eqn. 4.2.1, the input and output signals can be derived from the field test or simulation with the FE catenary (here, the latter is used). The disturbance-augmented catenary system is represented in Eqn. 4.3.5. Considering that it is the contact force that causes the displacement of the contact wire which is the most interested result, the system input is the contact force, and the output is the contact wire displacement.

The disturbance is regarded to act on the time derivative of the state of catenary velocity (i.e., $E = [0 \quad 1]^T$). This assumes that the disturbance is applied in the form of force (acceleration change) on the mass of the nominal linear model.

$$\begin{bmatrix} \dot{x} \\ \ddot{x} \\ \dot{d} \end{bmatrix} = \begin{bmatrix} 0 & 1 & 0 \\ -\frac{k_c}{m_c} & -\frac{C_c}{m_c} & 1 \\ 0 & 0 & 0 \end{bmatrix} \begin{bmatrix} x \\ \dot{x} \\ d \end{bmatrix} + \begin{bmatrix} 0 \\ \frac{1}{m_c} \\ 0 \end{bmatrix} u \qquad y = [1 \quad 0 \quad 0] \begin{bmatrix} x \\ \dot{x} \\ d \end{bmatrix} \tag{4.3.5}$$

With the parameters of the lumped-mass catenary presented in Table 4.2.1, the disturbance can be obtained through the system observer, as shown in Figure 4.3.1. The obtained disturbance is then augmented on the nominal linear lumped-mass catenary model to reproduce the system disturbance. The overall workflow is presented in Figure 4.3.2.

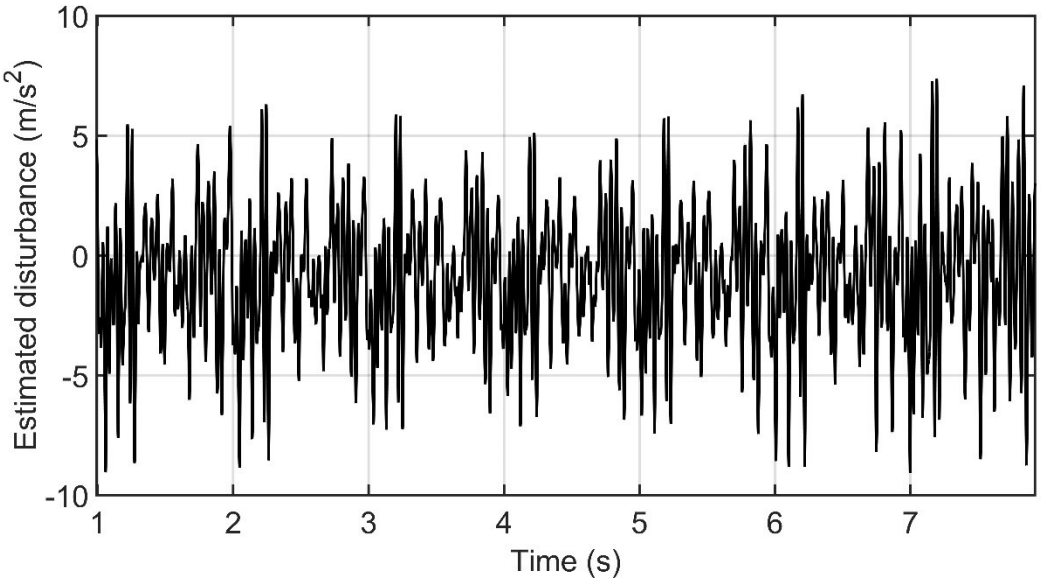


Figure 4.3.1. Obtained disturbance signal

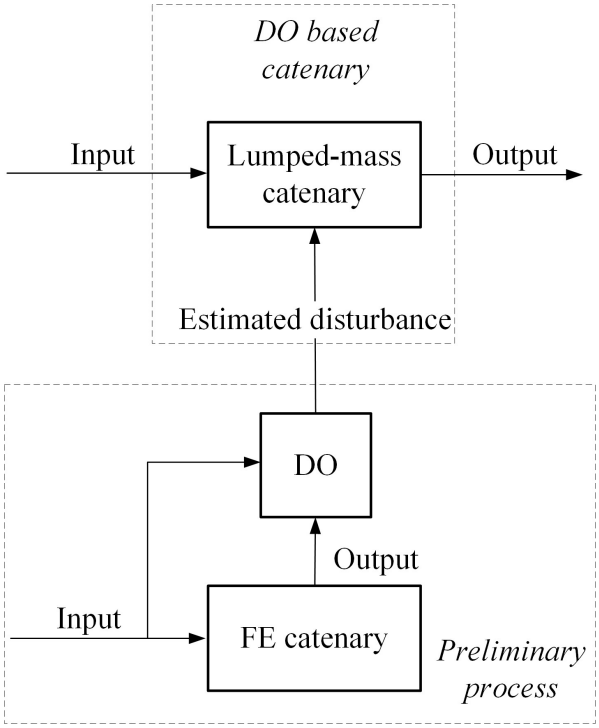


Figure 4.3.2. Workflow of DO-based catenary development

The developed DO-based catenary is then simulated and compared with the FE catenary. Figure 4.3.3 compares the contact force time history and Table 4.3.1 compares the numerical indicators of the contact force, which all indicate the DO-based result is nearly identical to that of the FE catenary.

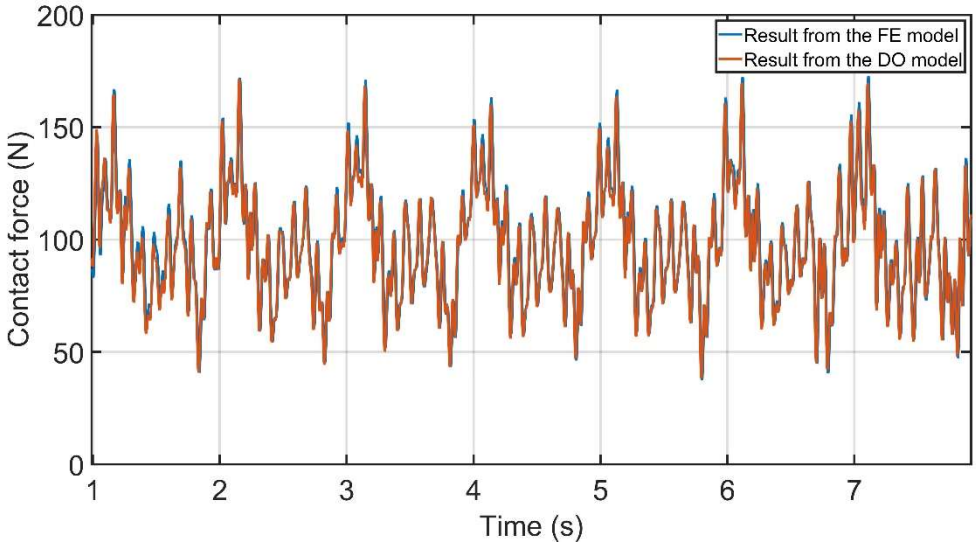


Figure 4.3.3. Contact force result of the DO model

Table 4.3.1. Numerical result of the DO model

Contact force	DO model	FE model
Mean (N)	98.55	97.34
Standard deviation (N)	24.72	24.24
Minimum (N)	37.45	38.31
Maximum (N)	172.80	171.38
R^2 (coefficient of determination)	0.8837	

4.4 Evaluation of DO-based catenary in active pantograph validation

Even though the DO-based catenary model has shown nearly identical contact force compared with the FE catenary in the open-loop (passive pantograph) situation, the motivation for proposing the model is to validate the design of active pantographs. In this section, a controller will be built based on the linear model of the pantograph–catenary system and the active pantograph will be simulated with the FE, classic time-varying lumped-mass and DO-based catenary models to evaluate the advantage of the DO-based catenary.

The goal of designing an active pantograph is to control the contact force by providing the measured contact force (i.e., output feedback), to make the contact force closer to the desired magnitude and thus reduce fluctuations. A block diagram for the pantograph–catenary closed-loop system is depicted in Figure 4.4.1. The pantograph–catenary system (i.e., the plant to be controlled) contains a pantograph and a catenary model. The contact force is obtained by the penalty method and compared with the output set point. The output error is processed by a designed controller to produce the control input. It should be noted that the control input is force

in simulation, whereas the control input is the pneumatic pressure in the pantograph in the experiment in Chapter 6.6.

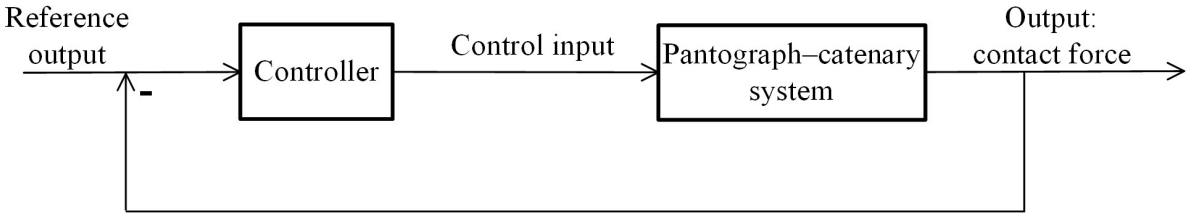


Figure 4.4.1. Block diagram for the pantograph–catenary closed-loop system

As discussed in the literature review, a frame-actuated active pantograph has not been realised in the closed-loop HIL situation, so this thesis focuses on the development of a frame-actuated active pantograph. Hence, in the system state-space representation Eqn. 4.2.2, the input matrix remains the same as the channel of the pantograph pneumatic uplift force, but the meaning of the input u changes to the control force. The parameters used for the linear model are presented in Table 3.2.1 and Table 4.2.1. Note that the linearised catenary model is parameterised for a running speed of 200 km/h, and thus the active pantograph will be designed and validated for the case of 200 km/h.

PID controllers are still used extensively and dominatingly in solving output regulation problems (Rawlings et al., 2002). Hence, a PID controller will be designed for the active pantograph as an example to evaluate the performance of the DO-based catenary model in the validation.

Tuning of a PID usually aims to balance the closed-loop response of the plant (such as response time and transient behaviour (i.e., phase margin)), from which the disturbance rejection ability can be roughly estimated. An intuitive way to derive a good disturbance rejection performance is that the rise time should be fast (and no overshoot appears) and the oscillation in the transient period should be mild. This accords with the fact that the oscillation phenomenon and overshoot

can usually be interpreted as a resonance in the closed-loop frequency response, which contradicts the target of disturbance rejection where the magnitude of the closed-loop frequency response is expected to be 1.

According to the above argument, the PID controller is tuned with a closed-loop step response time of 0.45 seconds and the most robust transient behaviour (phase margin of 90 degrees). The tuned closed-loop step response is shown in Figure 4.4.2. The PID parameters and step response performances are summarised in Table 4.4.1.

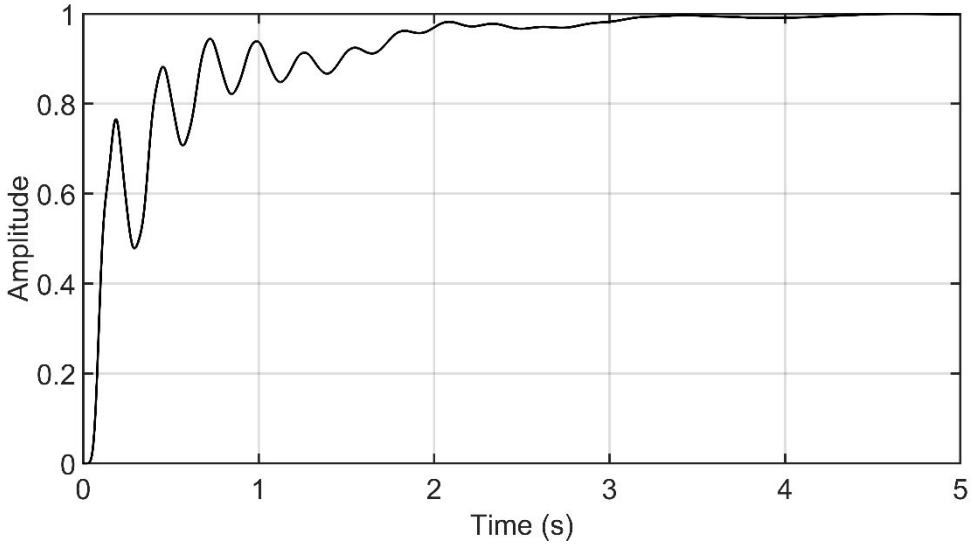


Figure 4.4.2. Step response of the closed-loop system

Table 4.4.1. Dynamic result of the DO model

Parameters				Performance		
Proportional (P)	Integral (I)	Derivative (D)	Filter coefficient (N)	Rise time (s)	Settling time (s)	Overshoot (%)
1.0833	2.5861	−0.1887	4.4444	0.607	2.92	0

The controllers are then validated on the FE, classic and DO-based lumped-mass catenary models at a train running speed of 200 km/h. The contact force and control input are shown and

compared in Figure 4.4.3 and Figure 4.4.4. The accuracy of the two lumped-mass catenary models on the basis of the FE model is measured and compared in Table 4.4.2.

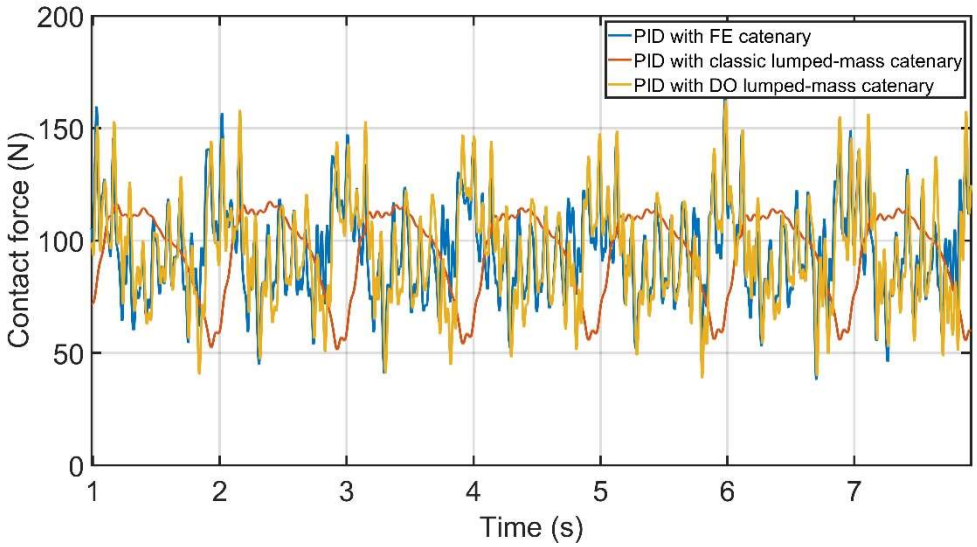


Figure 4.4.3. Control output - PID active pantograph with catenary models

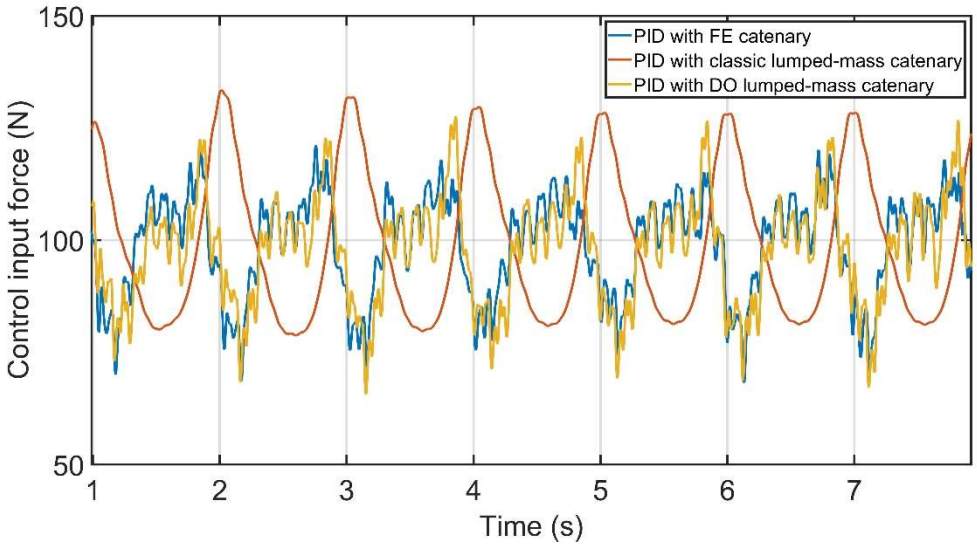


Figure 4.4.4. Control input - PID active pantograph with catenary models

Table 4.4.2. Accuracy comparison between the two catenary models

Catenary model	DO-based	Classic time-varying
R^2 of contact force (output)	0.4995	−1.6806
R^2 of control force (input)	0.6944	−4.3150

In terms of the veracity of the classic and DO-based lumped-mass models, it is clear from the figures and the R-squared index that the performance of the DO-based catenary model is much closer to that of the FE catenary regarding the contact force and control input. In terms of the simulation computing time of each model, the two lumped-mass catenary models can save approximately 12 hours for each validation run compared to the FE model. Therefore, it is concluded that the DO-based catenary model is an accurate and time-efficient approach for active pantograph validation.

Table 4.4.3 is focused on the metrics of the closed-loop performance of the PID controller. The control performance in reducing contact force fluctuation with the DO-based catenary is shown to be more conservative than that with the FE catenary, which is considered to be a good feature in the controller validation process. The conservativeness is due to when the pantograph–catenary contact force fluctuates less, the (lumped) disturbance is also reduced, becoming smaller than the estimated value in the passive pantograph case.

Table 4.4.3. Numerical results of the PID active pantograph

Closed-loop performance	DO-based model		FE model	
	Value	Improvement from its open loop	Value	Improvement from its open loop

Contact force (N) (output)	Standard deviation	23.06	6.72%	20.58	15.08%
	Minimum	38.78	3.55%	38.04	6.29%
	Maximum	162.42	6.01%	166.09	3.03%
Control force (N) (input)	Minimum	65.65	N.A.	68.21	N.A.
	Maximum	127.56	N.A.	121.13	N.A.

The DO-based lumped-mass catenary has shown fast computational speed and high accuracy, which can be used in fast controller validation for active pantographs and the design of a virtual catenary for HIL experiments. However, two drawbacks should be noted when using this model. As the system disturbance is pre-defined, if there are other changes in the system (such as input variation in a closed loop), the disturbance cannot be modified in real time. Therefore, the application of the DO catenary should be limited to the situation where the 'other changes' are not significant. In addition, to acquire the disturbance signal, the system input and output signals are required, so it is necessary to run the complete FE model once. If different dynamic behaviours (such as with different speeds) are of interest, the simulations and disturbance observations in different situations must be conducted separately.

4.5 Summary and conclusion

As the classic time-varying lumped-mass model may not be accurate in delivering authentic pantograph–catenary contact force results, a novel DO-based catenary model was proposed, and compared with the classic approach in this chapter. The DO-based catenary model was developed by using the DO to extract the dynamic information of the FE catenary and

augmenting the information with the linear catenary model to reproduce the dynamic behaviour exhibited in the FE catenary.

In the open-loop (passive pantograph) simulation, the DO-based catenary model can present contact force results nearly identical to those of the FE model (which is considered as the source of truth), much better than the classic time-varying lumped-mass model. The outcome of the DO-based catenary model is delivered by the augmented disturbance that sums up the impact of the catenary geometry variation on the contact wire.

The accuracy of the model in the closed loop is has been evaluated with an active pantograph. The active pantograph is actuated by a PID controller which was designed based on the mathematical representation of the pantograph–catenary system. Although the performance of the DO-based model in the closed loop is more conservative, not as perfect as in the open loop in terms of reproducing the response of the FE catenary (as the actual disturbance changes with the control input), the result with the DO-based model is still quite similar to that with the source of truth. It is concluded that the proposed DO-based catenary is a competent model for active pantograph validation, which can replace the role of the classic time-varying lumped-mass model.

As the DO-based catenary is accurate (due to the contribution of the DO) and computationally efficient (as it is built on top of the lumped-mass catenary model), it is also a decent candidate for being a virtual catenary model in real-time HIL experiments. Moreover, by virtue of using the DO, the DO-based model is able to incorporate external (environmental) interferences into the catenary model, and the real-world contact force data can be also used in developing the DO-based catenary model, all of which can improve the modelling authenticity.

CHAPTER 5 ACTIVE PANTOGRAPH DESIGN AND VALIDATION IN SIMULATION

5.1 Introduction

In this chapter, active pantographs are designed with a variety of control methods based on the linear pantograph–catenary model, and validated with the previously developed DO-based catenary model in simulation. There are three motivations for conducting the active pantograph designs and validations.

First, in the literature review, it was found that not many active pantograph studies have been validated with accurate catenary models. Even though some have been well validated, most of them use PID controllers whose tuning is not based on the mathematical model of the pantograph–catenary system. Therefore, it is worthwhile exploring the effectiveness of the model-based active pantograph when validating with an accurate catenary model (such as a DO-based catenary).

Second, besides the PID controller (which has been designed in Chapter 4.4), four control methods, ranging from the classic control method to the proposed DO-based sliding mode controller, are further applied to design active pantographs (in Chapters 5.2 to 5.5, respectively). By comparing the pros and cons of these control laws in active pantographs in simulation, the feasibility of applying the active pantographs in the laboratory can be discussed.

Third, besides validating the active pantographs with the DO-based catenary model, they are additionally tested with the FE catenary. The comparison between the results can be used to further evaluate and confirm the veracity of the DO-based catenary model in the active pantograph validation.

As already mentioned in Chapter 4.4, this thesis is focused on the development of a frame-actuated active pantograph, and the design is based on the linearised system plant of Eqn. 4.2.2 with the parameters presented in Table 3.2.1 and Table 4.2.1.

It is worth noting that the goal of designing a closed-loop pantograph is to control the contact force through output feedback to make the contact force closer to the set point, as shown in Figure 4.4.1. Hence, a key aim of the control is to minimise standard deviation of variations in contact force. From the simulation in the previous chapter, it can be seen that the fluctuation of the contact force is dominated by a component at the dropper-passing frequency (around 10 Hz). Therefore, in the simulation of active pantograph design and validation in this chapter, some controllers (the H-infinity and disturbance observer based sliding mode) are designed to attenuate the response at this high frequency.

However, in Chapter 6, the pneumatic system is selected as the actuator for active control, with a bandwidth of around 2 Hz, in the experiment. Therefore, the two controllers designed in this chapter are not as effective in practice as they would be in simulation, but however, they are worth discussing to explore the theoretical performance of active pantographs under different control laws and to evaluate the accuracy of the DO-based catenary model in active pantograph validation. In the long run this could be improved by a redesign of the pantograph itself in order to obtain an active system with a higher bandwidth.

5.2 Loop shaping and phase-lead or lag compensator

If a good reference tracking (output regulation) performance is desired, the magnitude of the closed-loop response is expected to be 1 and its open-loop response should be as large as possible (in a unit negative feedback system). However, this might result in the controller becoming sensitive to noise. To balance the tracking and noise rejection performances, the

terms Sensitivity and Complementary Sensitivity are introduced (Sung and Hara, 1988). Generally, for a unit negative feedback system (with an open-loop response CG, where C and G is the system of controller and plant, respectively), the Sensitivity (Eqn.5.2.1) is related to the performance of output tracking while the Complementary Sensitivity (Eqn. 5.2.2) is related to the anti-noise performance (Åström and Murray, 2021).

$$S = \frac{1}{1 + CG} \tag{5.2.1}$$

$$T = \frac{CG}{1 + CG} \tag{5.2.2}$$

Both S and T are supposed to be small but as $S + T = 1$, it is impossible to make both two indicators low at the same frequency. Therefore, a common solution is to make S small at low frequency and T small at high frequency, for good reference tracking and disturbance rejection performance. Considering the open-loop response CG, this solution can be interpreted as making the magnitude of the open-loop response large at low frequency and small at high frequency.

The controller C is responsible for shaping the system's open-loop response with the above target. A simple approach is using a phase-lead or phase-lag controller or their combination. A general transfer function of lead compensators is shown in Eqn. 5.2.3. This type of compensator can offer a magnitude increase and phase lead after and at a particular frequency. It is usually used to improve the phase margin. A general transfer function of lag compensators is shown in Eqn. 5.2.4. This type can reduce the magnitude of the open-loop response at high frequency and thus improve the gain margin.

$$G_{lead}(s) = \frac{\alpha Ts + 1}{Ts + 1}, \alpha > 1 \tag{5.2.3}$$

$$G_{lag}(s) = \frac{\alpha Ts + 1}{Ts + 1}, \alpha > 1 \tag{5.2.4}$$

Besides the phase-lead or lag compensator, it is recommended that the loop-shaping synthesis can be further considered to compute a controller which can help to obtain the desired open-loop shape (Skogestad and Postlethwaite, 2005).

As the phase-lead or lag compensator is usually designed based on the open-loop frequency response, it is difficult to optimise the performance of disturbance rejection. Hence, the phase-lead or lag compensator can also be tuned by foucing on reducing the system disturbance response. The tuning is usually based on experience and can be further studied to improve control effectiveness.

Considering the linearised pantograph–catenary model, a phase-lag compensator is designed for the pantograph–catenary linear model. The lag compensator reduces 32.89 degrees at 3.09 Hz on the open-loop response, and its transfer function is shown in Eqn. 5.2.5. The system disturbance rejection performance is presented in Figure 5.2.1, where the system disturbance is defined as the force (acceleration change) on the mass of the nominal catenary linear model, as same as in Chapter 4.3. It is shown that the closed-loop reduces the disturbance response at the pantograph span-passing frequency (at around 1 Hz) and dropper-passing frequency (at around 10 Hz).

$$C(s) = 0.16827 * \frac{s + 224.1}{s + 66.38} \tag{5.2.5}$$

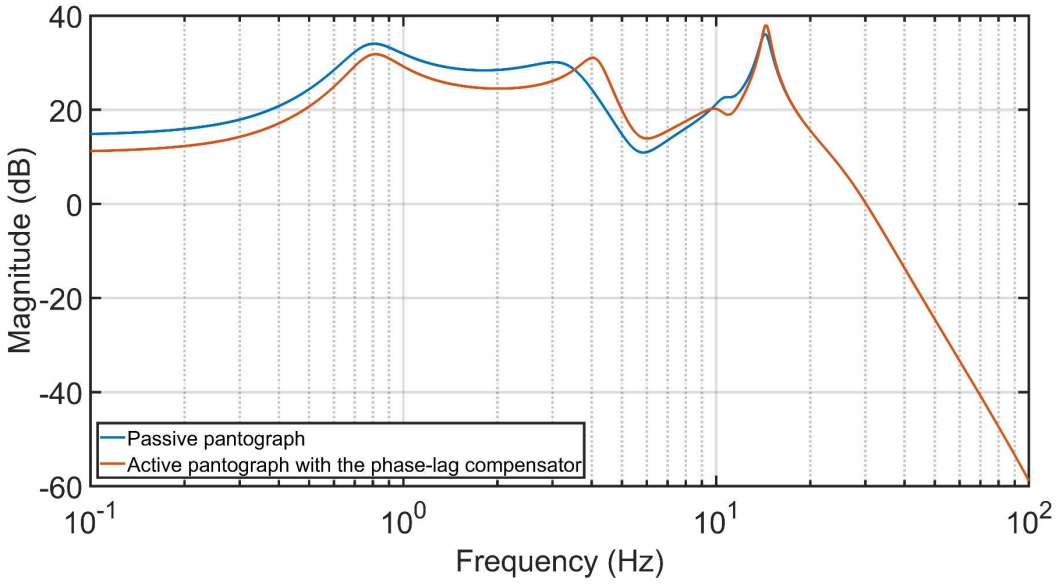


Figure 5.2.1. Disturbance rejection performance of passive and active pantographs

The designed active pantograph is validated with the DO-based catenary model and FE catenary model (to confirm the veracity of the DO-based catenary model). The results are presented in Figure 5.2.2, Figure 5.2.3 and Table 5.2.1. With the phase-lag controller, the contact force standard deviation is reduced. The reduction is stronger than for the PID approach (presented in Table 4.4.3), but the efforts in control input are less required.

Not surprisingly, from the table and figures, it can be seen that the DO-based catenary performs similarly to the FE catenary, including the contact force and input force. The controller effectiveness metrics show that the improvement with the DO-based catenary model is still conservative.

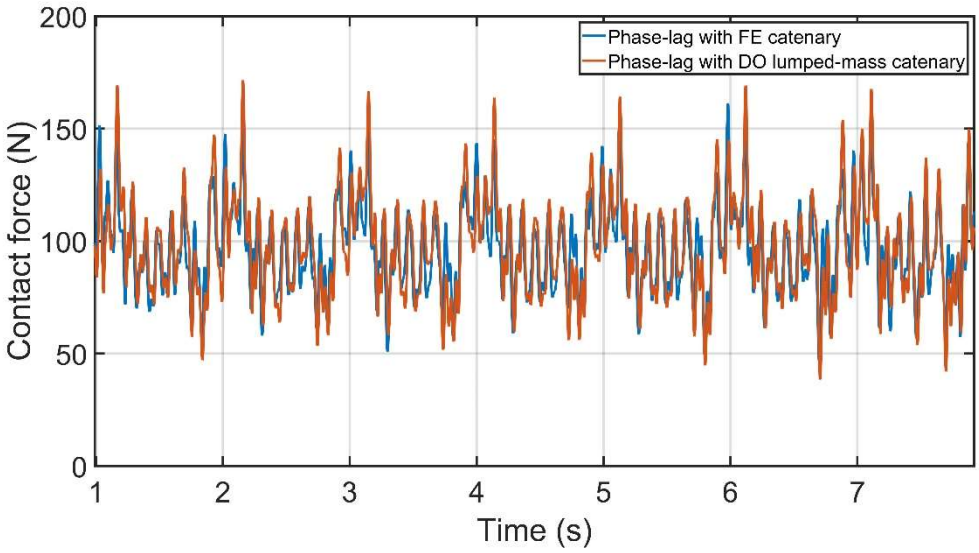


Figure 5.2.2. Control output - phase-lag active pantograph with catenary models

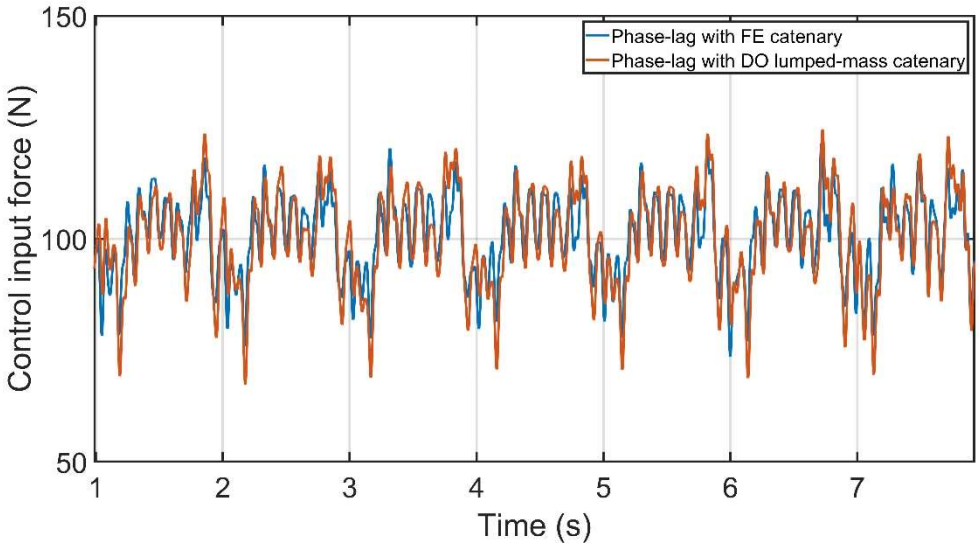


Figure 5.2.3. Control input - phase-lag active pantograph with catenary models

Table 5.2.1. Numerical results of the phase-lag active pantograph

Closed-loop performance		DO-based model		FE model	
		Value	Improvement from its open loop	Value	Improvement from its open loop
Contact force (N) (output)	Standard deviation	22.28	9.87%	19.00	21.62%
	Minimum	38.46	2.70%	46.09	20.31%
	Maximum	171.51	0.75%	161.16	5.96%
Control force (N) (input)	Minimum	67.29	N.A.	73.56	N.A.
	Maximum	124.50	N.A.	121.43	N.A.

5.3 Linear Quadratic Regulator

The previous PID and loop-shaping methods are mainly based on the classical control theory that relies on the understanding of a system's input-to-output response. The modern control theory using the state-space representation can reveal the dynamic characteristics of the states inside the model. This feature offers insights into the plant so that the dynamic behaviours (including input cost, disturbance impact, etc.) can be quantified and balanced.

One of the most widely used control laws in the modern control category is the Linear Quadratic Regulator (LQR) (Franklin et al., 2011). This method is also popular in solving the pantograph–catenary contact force regulation problem, as summarised in Table 2.3.1. The LQR is a linear controller aiming to regulate the states (and outputs) to be maintained at desired values, and it uses a quadratic cost function to design optimised feedback gains. A typical cost function is presented below, where x is the state matrix of the system; u is the input matrix of the system; Q is the state-cost weighted matrix; R is the input-cost weighted matrix.

$$J = \frac{1}{2}\int_{t_0}^{\infty} [x^T(t)Qx(t) + u^T(t)Ru(t)]dt \tag{5.3.1}$$

In order to ensure the cost function Eqn. 5.3.1 reaches the minimum, the control input is designed as in Eqn. 5.3.2.

$$u(t) = -Kx(t) = -R^{-1}B^T Px(t) \tag{5.3.2}$$

where P is the non-negative solution of the following Riccati equation.

$$PA + A^T P - PBR^{-1}B^T P + Q = 0 \tag{5.3.3}$$

It can be seen from Eqn. 5.3.2 that the control input is a function of the system states, which requires the measurement of all states (named state feedback). However, the states of a system may not be all measurable. Therefore, for a linear system, a Luenberger observer can be designed to estimate the states through the system's inputs and outputs (already introduced in Chapter 4.3). Based on the linear system model and the frequency of interest (20 Hz), the observer gain is designed as Eqn. 5.3.4.

$$L = [39.96, -97.72, 37.77, 165.12, 25.49, 30.15, 23.69, -3.16 \times 10^4, 19.17, -0.07, 3.67 \times 10^{-4}] \tag{5.3.4}$$

For the pantograph–catenary contact force regulation problem, the control target is to maintain the contact force at the desired value. To regulate the force, an additional state is constructed, which is designed as $\dot{x_i} = y_d - y$. By the LQR method, the controller is then tuned to minimise x_i which is the integral of the output error. The system representation Eqn. 4.2.2 becomes Eqn. 5.3.5. The block diagram of the LQR plus output integral is depicted in Figure 5.3.1.

$$\begin{bmatrix} \dot{x} \\ \dot{x_i} \end{bmatrix} = \begin{bmatrix} A & 0 \\ -C & 0 \end{bmatrix} \begin{bmatrix} x \\ x_i \end{bmatrix} + \begin{bmatrix} B \\ -D \end{bmatrix} u + \begin{bmatrix} 0 \\ y_d \end{bmatrix}$$
$$y = [C \quad 0] \begin{bmatrix} x \\ x_i \end{bmatrix} + Du \tag{5.3.5}$$

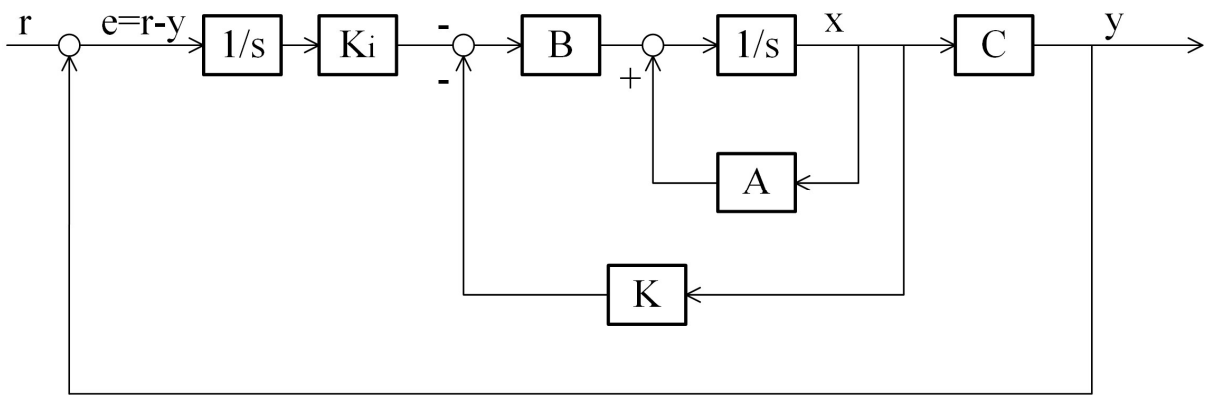


Figure 5.3.1. Structure of LQR plus output integral

The weighted matrices Q and R in Eqn. 5.3.1 are designed as follows. As the motion of the pantograph and catenary are not of interest, the only thing to be considered is how big an effort will be put in to minimise the output error. With a unified input weight, the optimal error weight can be found through exhaustive enumeration in the simulation. This enumeration is conducted with the DO-based catenary model to find the error weight (which is another advantage of fast simulation when using a DO-based catenary). An error weight of 70 is found for the best performance in contact force standard deviation reduction. By solving the Riccati equation Eqn. 5.3.3, the closed-loop poles and required feedback gains are obtained, as presented below.

$$Q = diag(0,0,0,0,0,0,0,0,0,0,70), R = 1 \tag{5.3.6}$$

$$poles = \begin{bmatrix} -0.83 + 5.03i \\ -0.83 - 5.03i \\ -3.76 + 90.15i \\ -3.76 - 90.15i \\ -5.03 + 67.25i \\ -5.03 - 67.25i \\ -5.91 + 21.43i \\ -5.91 - 21.43i \\ -6.46 + 0.00i \\ -60.02 + 151.74i \\ -60.02 - 151.74i \\ -122.94 + 0.0i \end{bmatrix} \tag{5.3.7}$$

$$K = [943.54 \quad 52.03 \quad 202.12 \quad 73.82 \quad -18.28 \quad 53.38 \quad -563.34 \quad -166.44 \quad 8.36 \quad 2042.78 \quad 347948.38 \quad -8.37] \tag{5.3.8}$$

The simulation results of the active pantograph with the LQR controller are shown in Figure 5.3.2, Figure 5.3.3 and Table 5.3.1. The response of the DO-based catenary is relatively consistent with that of the FE catenary. The numerical results show that the LQR-integral active pantograph has the lowest contact force standard deviation compared to the previous PID and phase-lag controllers. The controller performance validated with the DO-based catenary model is conservative, compared with validation with the FE catenary.

Compared to the classical control methods, the LQR requires the designs of the state observer and state weighting matrix, which provides more freedom but also makes it more difficult to tune and implement. The performance of the observer in estimating the contact wire displacement in the FE-based simulation is additionally presented in Figure 5.3.4.

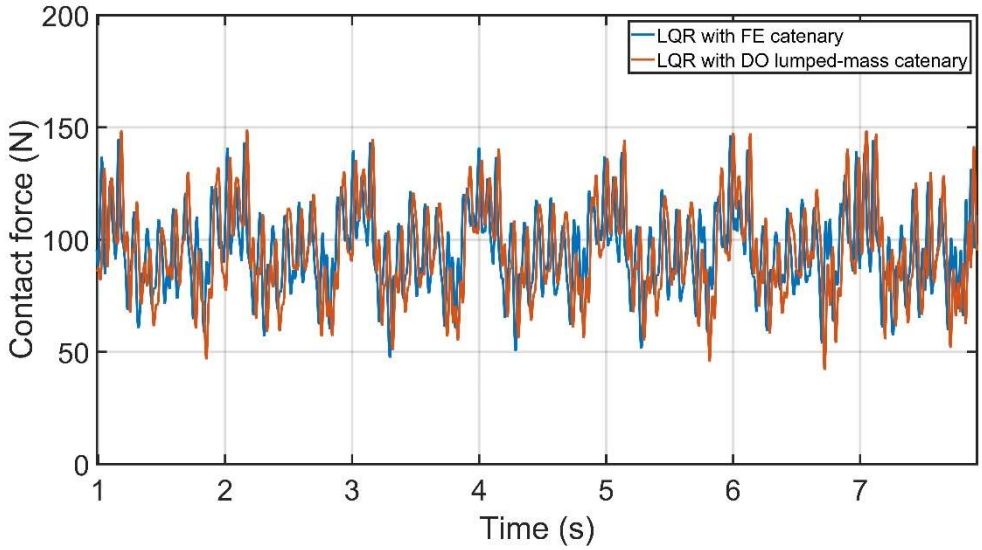


Figure 5.3.2. Control output - LQR-integral active pantograph with catenary models

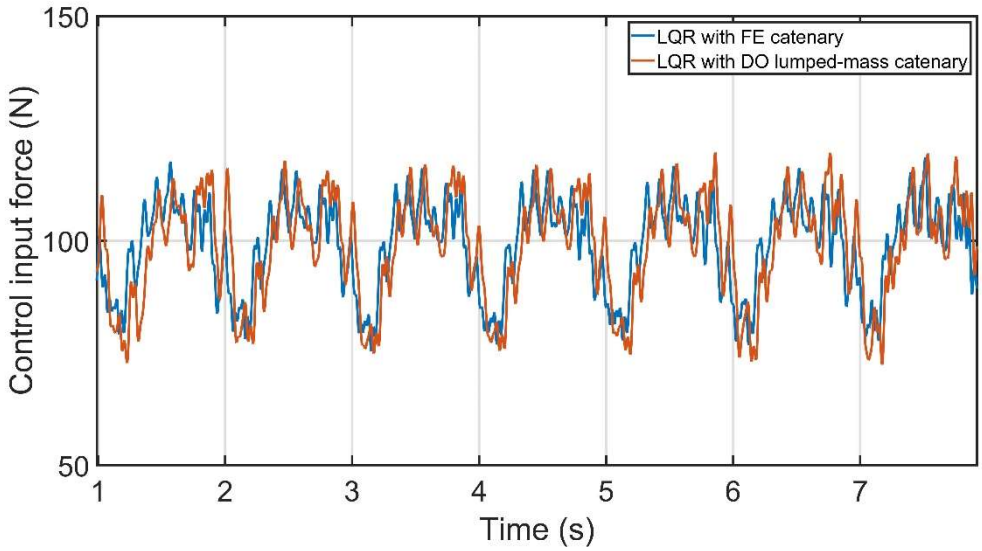


Figure 5.3.3. Control input - LQR-integral active pantograph with catenary models

Table 5.3.1. Numerical results of the LQR-integral active pantograph

Closed-loop performance		DO-based model		FE model	
		Value	Improvement from its open loop	Value	Improvement from its open loop
Contact force (N) (output)	Standard deviation	20.38	17.56%	17.83	26.44%
	Minimum	41.98	12.10%	47.41	23.75%
	Maximum	148.97	13.79%	146.57	14.48%
Control force (N) (input)	Minimum	40.74	N.A.	60.01	N.A.
	Maximum	115.40	N.A.	116.21	N.A.

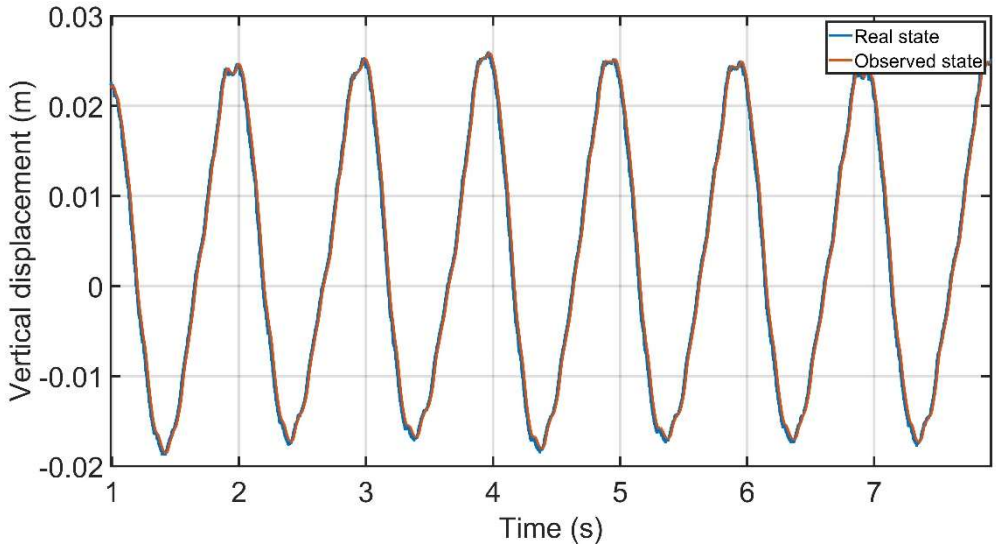


Figure 5.3.4. Contact wire displacement comparison between real and observed states

5.4 H-infinity optimal control

The H-infinity optimal controller aims to compute a controller that minimises the maximum effect of system disturbance on the output in the frequency domain. The H-infinity is essentially a norm that can be used to describe the peak response of a system. The H-infinity controller can be interpreted as reducing the peak of the disturbance magnitude response. To design optimal H-infinity controllers, if the way in which the disturbance enters the system is unknown, the H-infinity mixed-sensitivity loop-shaping approach can be applied. Unlike the loop shaping described in Chapter 5.2, the design of H-infinity loop shaping has a clear target which is reducing the H-infinity norms of the weighted indicators (i.e., sensitivity, complementary sensitivity, control effort). For more information about H-infinity loop shaping, please refer to (Ortega and Rubio, 2004, Safonov et al., 1989).

As it is assumed that the disturbance in the pantograph–catenary system is lumped as an acceleration change on the catenary mass, the optimal H-infinity controller can be designed from its augmented system. The general form of an augmented system is shown in Figure 5.4.1

and Eqn. 5.4.1, where z denotes the indicators of interest (e.g., system output); y denotes the signal feedback to the controller; w denotes the disturbance inputs; u denotes the control inputs.

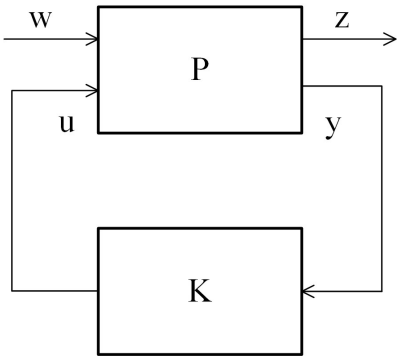


Figure 5.4.1. Augmented closed-loop plant for H-infinity design

$$\begin{bmatrix} z \\ y \end{bmatrix} = \begin{bmatrix} P_{11} & P_{12} \\ P_{21} & P_{21} \end{bmatrix} \begin{bmatrix} w \\ u \end{bmatrix} \tag{5.4.1}$$

Basically, the optimal controller that gives the minimum H-infinity norm γ_{min} of the controller cannot be obtained directly. A common way to find γ_{min} is to initially choose a γ and to check whether a controller is feasible through the Riccati formulae or linear matrix inequality functions (Doyle et al., 1988, Glover and Doyle, 1988). By iteratively reducing γ until there is no solution for the controller, the minimum value can be found.

For our pantograph–catenary force regulation problem, two metrics of the closed-loop system are of concern (i.e., z in Figure 5.4.1): the contact force and the control input. The system's external input signals (i.e., w in Figure 5.4.1) include desired (i.e., reference) output and system disturbance. Based on the pantograph–catenary linear representation in Eqn. 4.2.2 , the augmented system is presented in Eqn. 5.4.2 with two inputs: reference output r and defined disturbance d, and two outputs: control input effort u_o and output error e. E is the matrix that describes how the disturbance affects the system. A controller K is supposed to be designed with an input of e and output of u (i.e., the input and output are described for the controller K).

$$\dot{x} = Ax + [0 \quad E \quad B]\begin{bmatrix} r \\ d \\ u \end{bmatrix}$$
$$\begin{bmatrix} u_o \\ y \\ e \end{bmatrix} = \begin{bmatrix} 0 \\ C \\ -C \end{bmatrix} x + \begin{bmatrix} 0 & 0 & 1 \\ 0 & 0 & D \\ 1 & 0 & -D \end{bmatrix}\begin{bmatrix} r \\ d \\ u \end{bmatrix} \tag{5.4.2}$$

One of the benefits of using H-infinity synthesis is that the importance of each output (i.e., u_o and y) can be weighted separately at different frequencies through frequency-dependent functions. The frequency-dependent weight for the output y is designed as shown in Figure 5.4.2, whereas the weight for u_o is unified. The weight is obtained by superimposing four higher-order sub-weighting functions, which are specified using the Matlab function *makeweight* to determine the loop shapes. The sub-weighting functions are aimed to attenuate the disturbance caused by the pantograph span-passing (at around 1 Hz) and high-frequency noise.

Using such a high-order weighting factor can lead to a highly complex controller, which can be challenging to implement in practical control applications. This is a common practical issue with H-infinity control and a number of authors have considered methods for simplifying these controllers prior to implementation (Wang et al., 2007, Zebiri et al., 2014). Here, the focus is more on demonstrating the feasibility of frequency-based H-infinity controllers for active pantographs and evaluating the accuracy of the DO-based catenary model in active pantograph validation, especially under high-frequency control.

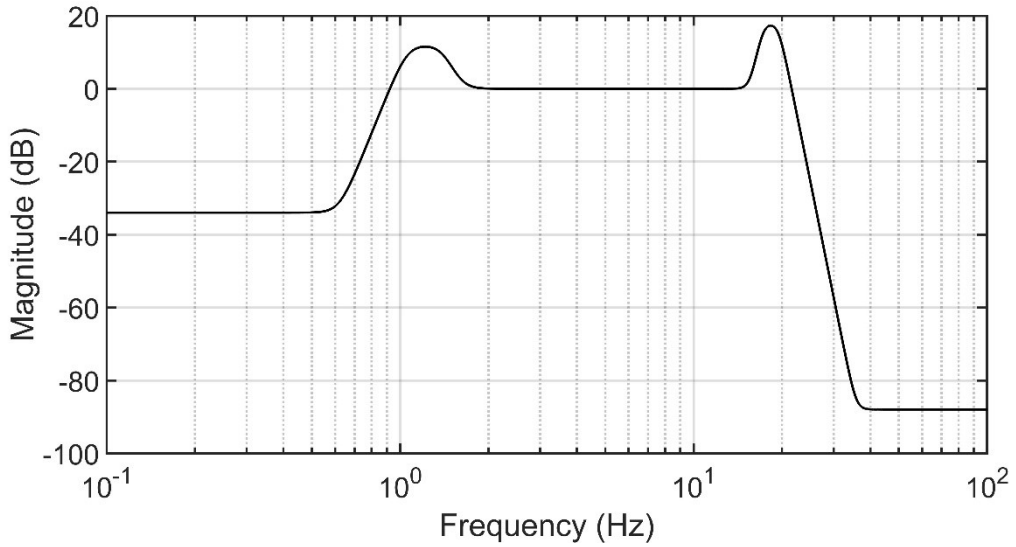


Figure 5.4.2. Frequency-dependent weight for the output *y*

The contact force and control input in simulations with the designed H-infinity controller are shown in Figure 5.4.3 and Figure 5.4.4. The numerical results are summarised in Table 5.4.1. Compared to the previous control methods, its control performance is just slightly worse than for the LQR. It can be further studied through the design of the frequency-dependent weighting factors. However, this requires comprehensive knowledge of the pantograph–catenary operation conditions.

The DO catenary still performs similarly to the FE catenary and its control performance is conservative. It is worthwhile mentioning that validation with the classic time-varying lumped-mass catenary model (not presented in the figure or table) delivers results that are too optimistic compared to the others: the standard deviation is reduced by 39.35%, while this number for DO catenary and FE catenary is 13.59% and 23.35%, respectively. The main reason is that the designed H-infinity controller has a 'side effect' in disturbance rejection performance at more than 5 Hz (which can be seen in Figure 5.4.5), but the high-frequency disturbance cannot be represented by the time-varying parameters in the classic lumped-mass catenary. This feature

has been confirmed to be critical in the validation of the active pantograph when a controller has an obvious effect at more than 5 Hz.

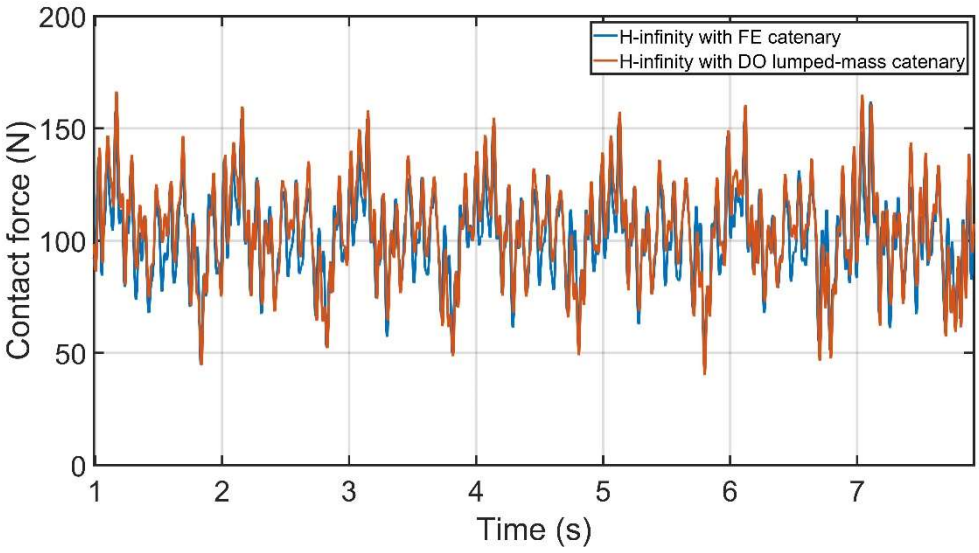


Figure 5.4.3. Control output - H-infinity active pantograph with catenary models

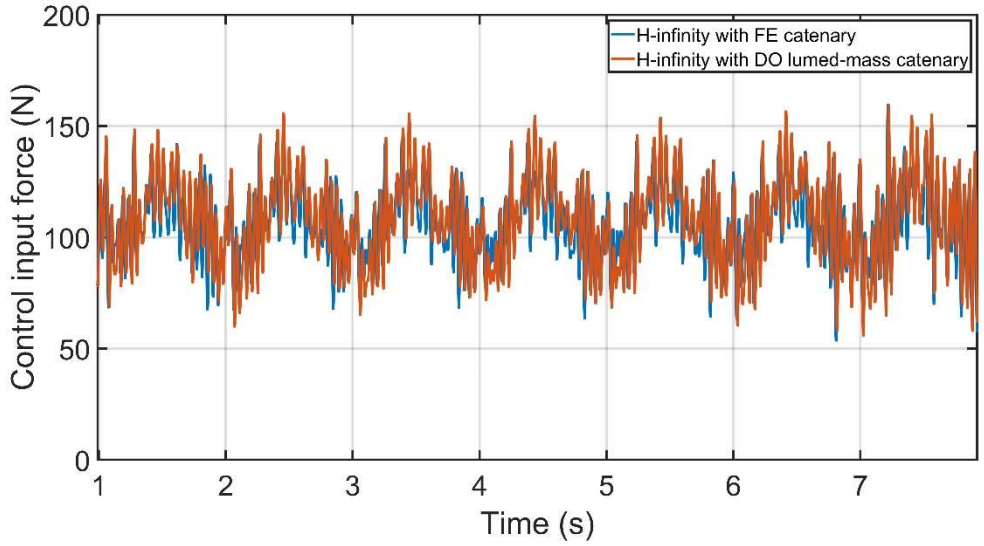


Figure 5.4.4. Control input - H-infinity active pantograph with catenary models

Table 5.4.1. Numerical results of the H-infinity active pantograph

Closed-loop performance		DO-based model		FE model	
		Value	Improvement from its open loop	Value	Improvement from its open loop
Contact force (N) (output)	Standard deviation	21.36	13.59%	18.58	23.35%
	Minimum	40.12	7.13%	44.82	16.99%
	Maximum	166.43	3.69%	161.88	5.54%
Control force (N) (input)	Minimum	55.43	N.A.	53.15	N.A.
	Maximum	159.62	N.A.	159.95	N.A.

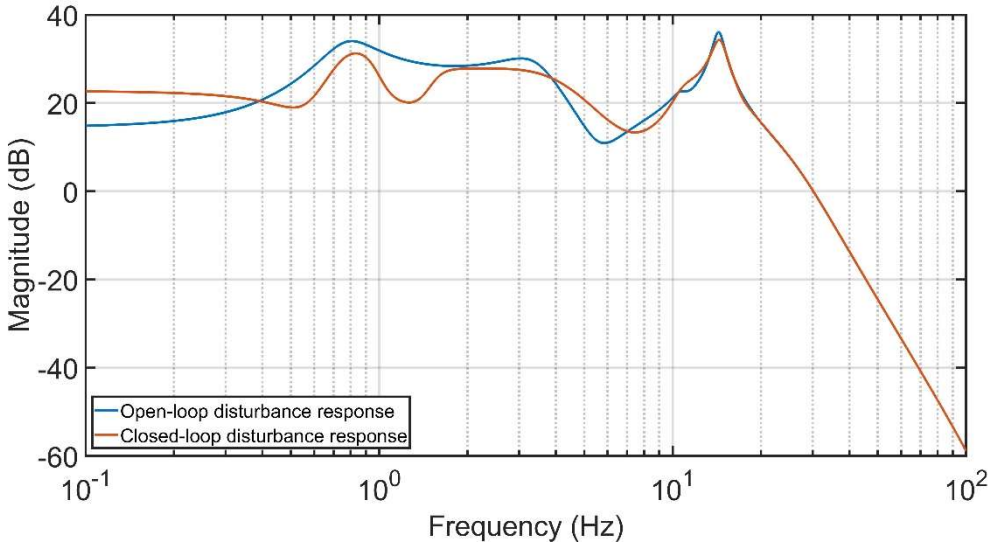


Figure 5.4.5. Disturbance response comparison between open loop and closed loop

5.5 Disturbance rejection and disturbance-observer-based control

5.5.1 Introduction

The target of the disturbance rejection control is to counteract or attenuate the effect of the disturbance. This disturbance includes modelling error, model uncertainties and unknown external interference; therefore, the method of rejecting the impact of the disturbance is also sometimes named robust control. In this section, a new control law combining the DO and sliding mode control is proposed and validated for the pantograph–catenary force regulation problem. In Chapter 4.3, the DO has been introduced and used to design the DO-based catenary model. The DO can estimate the lumped disturbance through the input and output of the defined pantograph–catenary system, which will be used in the closed-loop feedback.

A variety of disturbance rejection control laws have been developed. There are two classes in the disturbance rejection problem, that is whether the disturbance enters the system in the same channel as the control input (i.e., matched or mismatched disturbance) (Yang et al., 2011). For the problem with the matched condition, the essence of the robust compensator is to directly counteract the estimated disturbance by the system input (Zhong, 2002).

It can be found from the pantograph–catenary linear model that the defined disturbance affects the system on the second derivative of the catenary mass, which is different from the control input that affects the second derivative of the pantograph lower frame. To attenuate the influence of the mismatched disturbance, two control laws using a DO have been proposed by Li et al. (2011) and Sariyildiz et al. (2019a).

The above two disturbance rejection control methods have been applied to the pantograph–catenary model to try to counteract the effect of mismatched disturbance. However, the simulation result shows that neither of the above robust controllers is effective in attenuating

dynamic disturbance (they are effective with static and slowly changing disturbance); sometimes they may even result in a greater disturbance impact at high frequency. Hence, a new control law based on the DO and sliding mode control is proposed to regulate the pantograph–catenary contact force.

5.5.2 Disturbance observer based sliding mode control

Sliding mode control (SMC) belongs to the class of variable structure control (VSC) in control theory, which has a powerful ability to reject disturbances and plant uncertainties. Unlike the control laws introduced previously, the control law of VSC is changed during the control process according to the state of the system. Eqn. 5.5.12 is a commonly used switch function in SMC which modifies the control law based on the value of the sliding variable s. Once the states of the system are found outside the sliding surface $s = 0$, the control input can pull the states back to the sliding surface in a finite time, and the nominal system behaviour can be maintained (Edwards and Spurgeon, 1998).

$$sgn(s) = \begin{cases} 1 & if\ s > 0 \\ -1 & otherwise \end{cases} \tag{5.5.1}$$

It has been demonstrated that the combination of SMC and DO has a great benefit in attenuating the effect of mismatched disturbance for some classes of problem proposed in (Yang et al., 2012, Ginoya et al., 2013). Here, a DO-SMC control law for a class of the output regulation problem is proposed. Considering a system that is subject to a disturbance, as in Eqn. 5.5.2, where E is the channel of how the disturbance affects the system dynamics, the sliding variable is designed as in Eqn. 5.5.3, with the aim that the output error can approach zero.

$$\begin{aligned} \dot{x(t)} &= Ax(t) + Bu(t) + Ed(t) \\ y &= Cx(t) \end{aligned} \tag{5.5.2}$$

$$s = g * e + \dot{e} \tag{5.5.3}$$

where

$$e = y - y_d$$

For a class of problems where $CB = 0$ and $CE = 0$, the sliding variable becomes Eqn. 5.5.4 by combining Eqns. 5.5.2 and 5.5.3.

$$s = g * e + \dot{e} = g(Cx - y_d) + C(Ax + Bu + Ed) \tag{5.5.4}$$

Considering the disturbance-augmented linear pantograph–catenary model in Eqns. 4.2.2 and 4.3.1, no matter where the control input acts on the pantograph, $CB = 0$ and $CE = 0$. The sliding variable becomes Eqn. 5.5.5. The control input is designed as Eqn. 5.5.6.

$$s = g * e + \dot{e} = (gC + CA)x - gy_d \tag{5.5.5}$$

$$u = -(CAB)^{-1}[(gCA + CA^2)x + (Dis_{max} + \sigma) * sgn(s)] \tag{5.5.6}$$

where

$$Dis = |CAEd|$$

The parameter g is related to the speed of error approaching zero and D_{max} is the upper bound of the disturbance $CAEd$. To ensure the control input can always pull the states back to the sliding surface, the reachability condition is proved as follows.

From Eqn. 5.5.5,

$$\begin{gathered} \dot{s} = gC\dot{x} + CA\dot{x} \\ \dot{s} = gC(Ax + Bu + Ed) + CA(Ax + Bu + Ed) \\ \dot{s} = (gCA + CA^2)x + CABu + CAEd \end{gathered} \tag{5.5.7}$$

Let control input

$$u = -(CAB)^{-1}[(gCA + CA^2)x + v] \tag{5.5.8}$$

Combining Eqns. 5.5.7 and 5.5.8,

$$\dot{s} = -v + CAEd \tag{5.5.9}$$

Let

$$v = (|CAEd|_{max} + \sigma) * sgn(s) \tag{5.5.10}$$

Then

$$\begin{gathered} s\dot{s} = -sv + sCAEd \\ s\dot{s} = -D_{max}|s| - \sigma|s| + sCAEd \\ s\dot{s} \leq -\sigma|s| \leq 0 \end{gathered} \tag{5.5.11}$$

Control input design requires the knowledge of d as $|CAEd|$ needs to be estimated beforehand; it can be estimated offline from the DO, but does not need to be estimated with the observer in real time. The condition of applying this control law is Eqn. 5.5.12. If the control force acts on m_3 (pantograph head), the conditions can be met.

$$CAB \neq 0 \tag{5.5.12}$$

However, if the control input acts on m_1 (pantograph lower frame), which is the case discussed in this thesis, the condition of Eqn. 5.5.12 cannot be met. To apply the SMC in this case, the sliding variable with a higher order of error derivative is designed as Eqn. 5.5.13.

$$\begin{gathered} s = g_1 * e + g_2 * \dot{e} + g_3\ddot{e} + \dddot{e} \\ s = (g_1C + g_2CA + g_3CA^2 + CA^3)x + (g_3CAE + CA^2E)d + CAE\dot{d} - g_1y_d \end{gathered} \tag{5.5.13}$$

The control input of this case becomes Eqn. 5.5.14.

$$u = -(CA^3B)^{-1}[(g_1CA + g_2CA^2 + g_3CA^3 + CA^4)x + (Dis_{max} + \sigma) * sgn(s)] \quad (5.5.14)$$

where

$$Dis = |(g_2CA + g_3CA^2 + CA^3)Ed| + \left|(g_3CA + CA^2)E\dot{d}\right| + \left|CAE\ddot{d}\right|$$

The reachability proof is omitted as it is similar to the previous case. Dis now additionally consists of the first and second derivatives of the disturbance. Also, the sliding variable requires the real-time signals of d and $\dot{d}$, which requires a DO to observe the disturbance states.

The gain $g_i(i = 1,2,3\cdots)$ in the sliding variable s can be selected through the method proposed by (Lin and Hsiao, 2020), so that the eigenvalues of the sliding surface $s = 0$ can be located in the left plane that makes the error e approach to zero.

$$s = \left(\frac{d}{dt} + g\right)^n * e \quad (5.5.15)$$

For example, if $n = 3$ (i.e., the third-order derivative of the error exists), the sliding variable can be rewritten as Eqn. 5.5.16; by doing so, only one variable needs to be tuned.

$$s = g^3 * e + 3 * g^2 * \dot{e} + 3 * g * \ddot{e} + \dddot{e} \quad (5.5.16)$$

To estimate the disturbance d and its derivative $\dot{d}$, a first-order DO will be used. For a first-order DO, the system dynamics is augmented with a disturbance state (d) and its derivative, as shown in Eqn. 5.5.17 which assumes that $\ddot{d} = 0$.

$$\begin{bmatrix}\dot{x}\\ \dot{d}\\ \ddot{d}\end{bmatrix} = \begin{bmatrix}A & E & 0\\ 0 & 0 & 1\\ 0 & 0 & 0\end{bmatrix}\begin{bmatrix}x\\ d\\ \dot{d}\end{bmatrix} + \begin{bmatrix}B\\ 0\\ 0\end{bmatrix}u$$
$$y = [C \quad 0 \quad 0]\begin{bmatrix}x\\ d\\ \dot{d}\end{bmatrix} + Du \quad (5.5.17)$$

The disturbance states can be observed through a state observer. The observer estimates the states through the inputs and outputs of the system. For the disturbance-augmented linear system in Eqn. 4.3.5, a Luenberger observer can be designed as Eqn. 5.5.18, where $z = [x;\ d;\ \dot{d}]$, $A_d = [A\ E\ 0; 0\ 0\ 1; 0\ 0\ 0]$, $B_d = [B;\ 0;\ 0]$ and $C_d = [C\ 0\ 0]$; the hat notation represents the estimated state. The observer gain L is supposed to be tuned so that the observer error $e(t) = z - \hat{z} \to 0$ when $t \to \infty$.

$$\begin{aligned} \dot{\hat{z}} &= A_d\hat{z} + B_d u + L(y - \hat{y}) \\ \hat{y} &= C_d\hat{z} + Du \end{aligned} \tag{5.5.18}$$

Alleviation of the chattering problem is often to be considered when applying an SMC. When the states approach the sliding surface, the control structures will switch in high frequency as the states repeatedly cross the sliding surface. A natural solution is to smooth the discontinuity in the switching function. One possible approximation is the sigmoid-like function (Edwards and Spurgeon, 1998). In this thesis, an alleviation method proposed in (Ginoya et al., 2013) is applied, which introduces a linear term in the control input.

For the sliding variable containing the third-order differential of the error in Eqn. 5.5.13, the control input is modified as follows, where k_l is the SMC linear gain and k_s is the SMC switching gain, which are to be designed. The linear gain term helps alleviate chatter by making it possible to use a smaller k_s (i.e., $D_{max} + \sigma$).

$$u = -(CA^3B)^{-1}[(g_1CA + g_2CA^2 + g_3CA^3 + CA^4)x + k_l * s + k_s * sgn(s)] \tag{5.5.19}$$

5.5.3 Controller validation

Considering the identified parameters of the pantograph–catenary linear model listed in Table 3.1.1 and Table 4.2.1, the sliding variable and the control input are designed according to Eqns.

5.5.13, 5.5.14 and 5.5.16. $g = 50$ is selected to balance the control input and control performance. When the chattering alleviation method is adopted, the linear gain k_l is tuned as 50 and the switching gain k_s is tuned as 1.

The contact force and control input in simulations with the designed DO-SMC controller are shown in Figure 5.5.1 and Figure 5.5.2. The numerical results are summarised in Table 5.5.1. The control performance in the simulations with DO-based and FE catenary models becomes different. This emphasises that the accuracy of the DO model is limited by the magnitude of the closed-loop impact on the system compared to the nominal simulation conditions, although the resulted control effectiveness due to such errors is generally conservative. With the DO-SMC controller in action, the extremely large control input causes the actual disturbance to deviate away from the augmented disturbance. The unacceptable control input is because the control law contains the derivative of the disturbance, so the closed-loop system is sensitive to high-frequency changes (in disturbance) over the nominal model.

Focusing on the simulation with FE catenary (the source of truth), the DO-SMC control law has shown to be very effective in reducing contact force fluctuations, but the magnitude of control input is unacceptable.

Similar to the case with the H-infinity controller, as the high-frequency disturbance cannot be represented by the time-varying parameters in the classic lumped-mass catenary, validation with the classic time-varying lumped-mass catenary model (not presented in the figure or table) delivers results that are too optimistic: the standard deviation is reduced by 64.70% and the control input is reasonable (46–231 N). This evidences that the discrepancy of the classic lumped-mass catenary mode is critical in active pantograph validation.

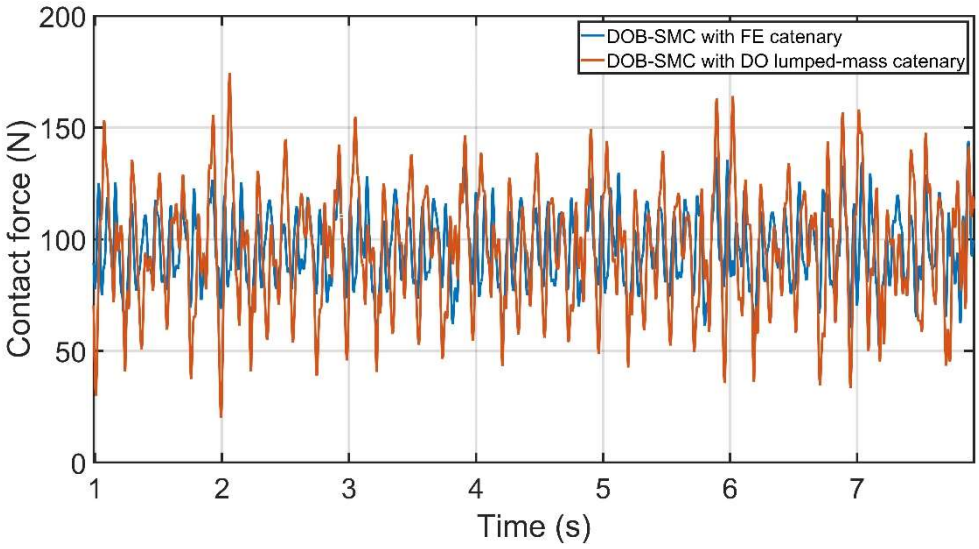


Figure 5.5.1. Control output - DO-SMC active pantograph with catenary models

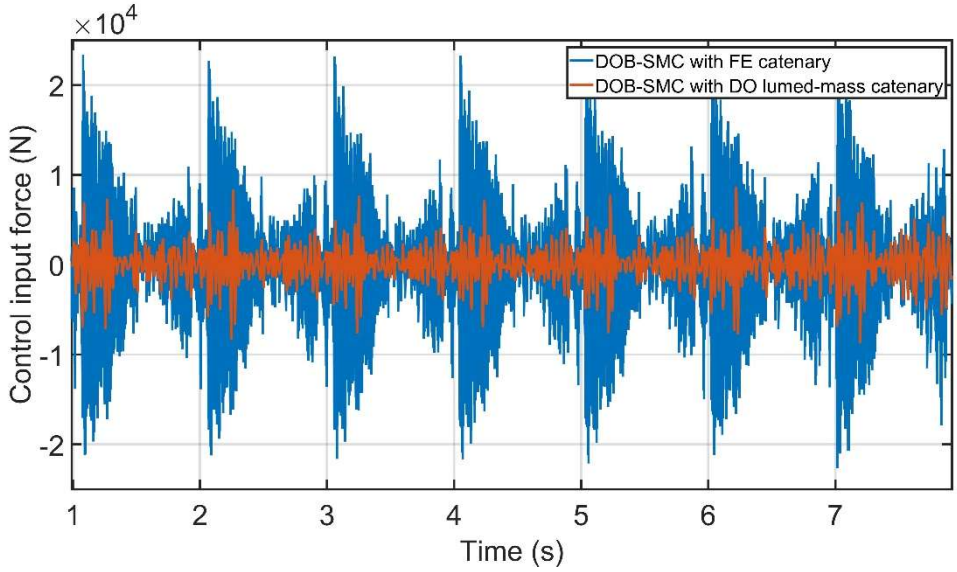


Figure 5.5.2. Control input - DO-SMC active pantograph with catenary models

Table 5.5.1. Numerical results of the DO-SMC active pantograph

Closed-loop performance		DO-based model		FE model	
		Value	Improvement from its open loop	Value	Improvement from its open loop
Contact force (N) (output)	Standard deviation	25.94	−4.92%	15.92	34.34%

	Minimum	20.08	−46.39%	50.86	32.76%
	Maximum	174.34	−0.89%	144.04	15.95%
Control force (N) (input)	Minimum	-8.77×10^3	N.A.	-2.26×10^4	N.A.
	Maximum	8.72×10^3	N.A.	2.40×10^4	N.A.

5.6 Summary and conclusions

This chapter presented the designs and validations of the active pantograph in simulation. It has shown that all the active controllers (including the PID which was designed in Chapter 4.4) can reduce the pantograph–catenary contact force standard deviation as they were expected at the design stage (except the DO-SMC approach due to an enumorous control input).

It is concluded that the active pantograph designed based on the linearised pantograph–catenary model is effective in reducing contact force fluctuation when validating with accurate catenary models. Each control method has its characteristics, as summarised below.

- The PID has the most limited control effectiveness (with the tuning method used) in reducing the contact force standard deviation, but it is easy to tune and implement.
- The phase-lead or lag compensator is designed based on the open-loop or disturbance rejection response of the system in the frequency domain. It is easy to tune and implement but it is difficult to optimise the disturbance rejection performance.
- The LQR can achieve good control effectiveness and it is easy to balance the control performance and the control input. However, the state observer increases the complexity of the feedback loop.

- H-infinity synthesis can balance the control performance and control input at different frequencies, but the design of weighting factors requires comprehensive knowledge of the pantograph–catenary operation conditions.
- Inspired by the SMC and DO, a DO-SMC control law suitable for the pantograph–catenary force regulation problem is proposed. Unlike the previous ones, this is a nonlinear controller which uses a switching function to modify the control input. The disturbance rejection performance is excellent but the most critical disadvantage is that it is very sensitive to high-frequency signals.

To realise the model-based active pantograph in the laboratory, the simplicity of the controller should be the most important factor at the current research stage considering the potentially large differences between a physical pantograph and its lumped-mass model. Therefore, considering the effectiveness and complexity of the controller, the phase-lead/lag compensator will be chosen as the candidate for active pantograph design and implementation in the laboratory in the next chapter.

The controllers were additionally simulated with the FE model to evaluate the veracity of the DO-based catenary model. The results showed that changes in the system inputs and outputs in the simulation with the DO-based catenary model generally follow those with the FE catenary, even with different control laws. The DO-based catenary model has been further confirmed to be an outstanding and effective approach for the active pantograph validation on the condition that the magnitude of the closed-loop impact on the system is not considerable.

CHAPTER 6 PANTOGRAPH–CATENARY HARDWARE-IN-THE-LOOP EXPERIMENT

6.1 Introduction

As testing active pantographs in a real-world situation is costly and risky, after designing and validating an active pantograph in simulation, the next step is developing and testing a prototype in the laboratory. As constructing a full-length overhead line for a pantograph to run through is not practical in the laboratory, hardware-in-the-loop (HIL) is the method used to study pantograph–catenary dynamics. In HIL, the contact between the pantograph and contact wire is reproduced by a moving contact point or contact bar whose motion follows the dynamics of a catenary model.

However, as concluded in the literature review, only a very limited number of validation works regarding active pantograph implementation and validation in the laboratory have been done, and none of their controllers is model-based. Therefore, the model-based active pantograph prototype is studied and tested in the HIL experiment in this chapter. Moreover, as the frame-actuated active pantograph has not been realised in a closed-loop HIL situation in existing studies, it is worthwhile developing a frame-actuated active pantograph. Due to the inherent difficulty in high-frequency control of objects, the limitation of the control bandwidth for frame-actuated systems is not as significant. This highlights the advantage of its ease of installation in the implementation of active pantograph.

This chapter has five subsections which deal with the aim of realising the model-based active pantograph in HIL.

In Chapter 6.2, the pantograph research test rig developed at the University of Birmingham (UoB) is briefly introduced.

As the development of the DO-based catenary model (the virtual catenary in HIL) requires the result of the pantograph–catenary simulation, the physical pantograph in the laboratory is first identified in Chapter 6.3.

In Chapter 6.4, simulation of the identified pantograph with an FE catenary is conducted, based on which the DO-based catenary model is developed.

The HIL control loop is developed in the pantograph test rig in Chapter 6.5, by which the test rig can reproduce the motion of the virtual catenary. The HIL performance is analysed and validated with the simulation results.

In Chapter 6.6, the active pantograph is designed and tested in HIL. The installation of the actuator and the design of closed-loop command flow in the test rig are presented. The whole system is identified and linearised, based on which the active controller is designed. The developed active pantograph is tested in simulation and HIL, and the results are analysed.

Before detailing each section, the overview of the developed active pantograph HIL test system is depicted in Figure 6.1.1. There are two control loops in the architecture: contact bar control loop and pantograph force control loop. The test rig contact bar control loop is designed for the HIL experiment where the height command is derived from the virtual catenary model subject to the contact force, aiming to reproduce the behaviour of the contact wire. The pantograph contact force control loop is designed to regulate the contact force through changing the air pressure in the pantograph. The air is provided by an air compressor and used to fill up a pneumatic actuator which is built into the body of the pantograph.

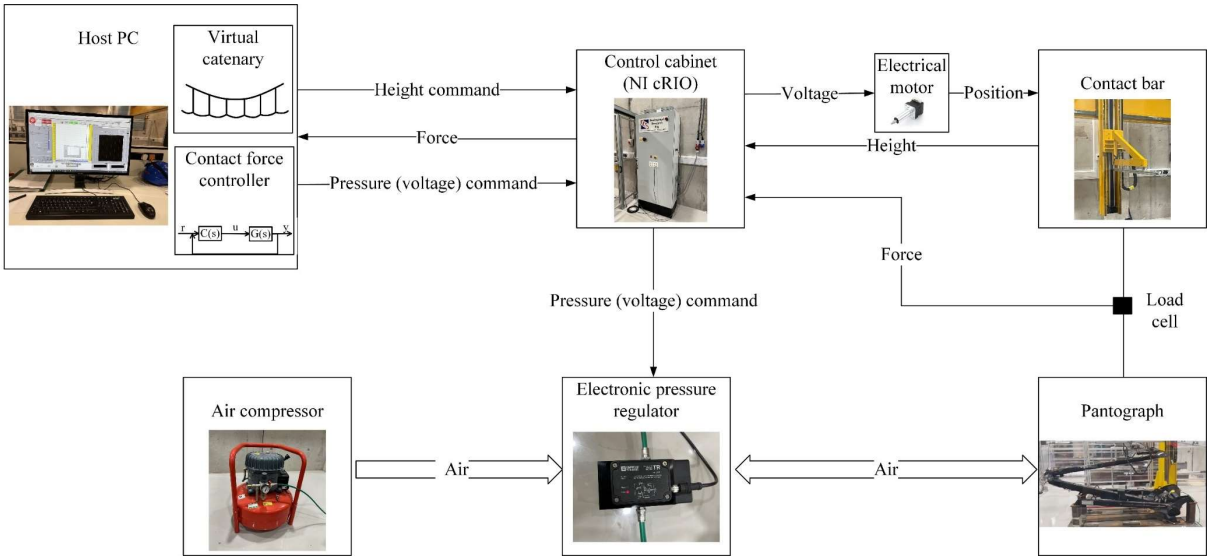


Figure 6.1.1. Overview of the active pantograph HIL test system

6.2 Test rig introduction

The pantograph–catenary HIL experiment is developed based on the UoB School of Engineering pantograph test rig. The pantograph test rig was built in 2016 and was initially used for the DynaPan project, which aims to design an intelligent condition monitoring system to realise automatic pantograph health checking for maintenance purposes. The pantograph under the test rig can be excited by pre-configured operating profiles, and the contact force data in tests are used for the pantograph health assessment (Xin et al., 2020).

The UoB pantograph test rig is mainly formed of three entities besides a physical pantograph: the host PC, control cabinet and contact bar frame, as shown in Figure 6.2.1. Generally, the host PC is the interface for the user to choose operation modes; the PC sends the command to the control cabinet; the control cabinet then controls the movement of the contact bar.

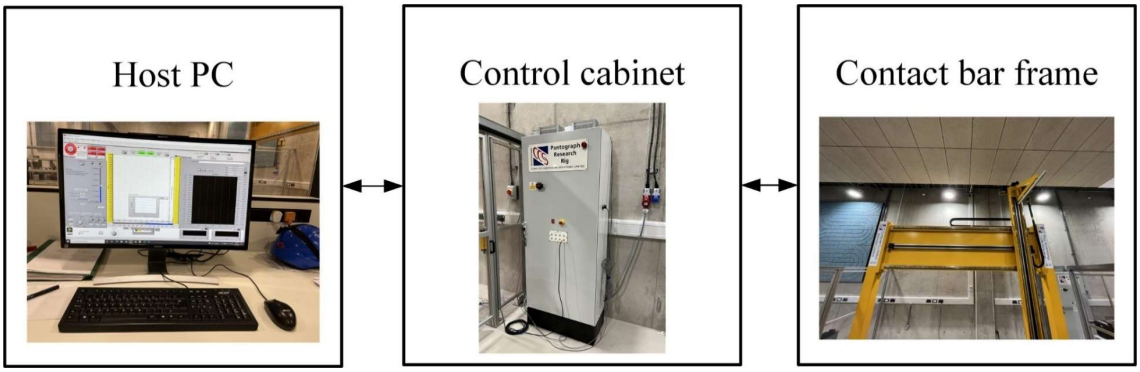


Figure 6.2.1. The three entities of the test rig

The physical pantograph used in the laboratory was manufactured by Brecknell Willis Ltd. The pantograph is designed for the British Rail Class 390 Pendolino high-speed train with a design maximum speed of 225 km/h and a service maximum of 200 km/h (Knight, 1998). The pantograph was not employed in train service before being sent to the laboratory, so it is in excellent condition for the study of pantograph–catenary dynamics. Figure 6.2.2 shows the pantograph situated under the contact bar frame in a state of collapse and separated from the contact bar. The air compressor needs to be turned on if the pantograph is expected to be in the normal operation state. The compressed air will then fill up the body of the pantograph and move the pantograph body upwards until it is in contact with the contact bar (contact wire with a physical catenary), as shown in Figure 6.2.3.



Figure 6.2.2. Collapsed pantograph under the test rig frame

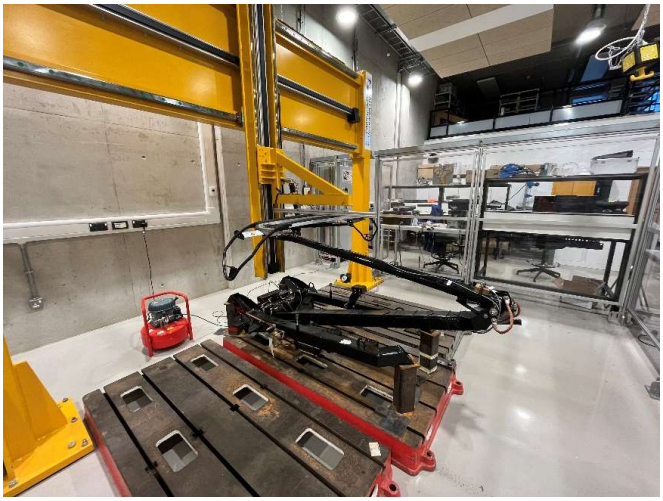


Figure 6.2.3. The pantograph in normal contact with the test rig frame

The development of the main test rig, including contact bar, control cabinet and host PC, is collaborated with Computer Controlled Solution Ltd and Motion Drives & Controls Ltd. The main function of the contact bar is to lead the movement of the pantograph so that it can be dynamically activated. The movement of the contact bar is controlled by two belts that are excited by electrical motors.

An accelerometer is mounted at the side of the contact bar, so the approximate pantograph head acceleration can be obtained. To obtain the contact force, two load cells are mounted between the silver contact bar and the yellow triangle frame. Considering the inertial effect, the contact force is derived through Eqn. 6.2.1 where $F_{sensors}$ is the measured force from the load cells, and ma is the inertial term of the contact bar.

$$F_{contact} = F_{sensors} + ma \tag{6.2.1}$$

The required pantograph (contact bar) movement is realised by a three-step workflow. The first is the user–PC interaction, where the operation modes (such as manual, dynamic and pre-configured movement) can be chosen on the user's interface.

The second process is the PC–CompactRIO interaction. The corresponding control functions will be sent into an NI-CompactRIO (cRIO) (model No. NI-9149) in the control cabinet. The cRIO provides high-performance real-time processing capabilities for the control of contact bar movement. The cRIO is also integrated with other modules used to receive and send analogue or digital signals from and to sensors, which are used to collect data from sensors and control electronic devices.

The last process is the cRIO–motor interaction. The control target is processed in the cRIO. Through the contact bar control function, the required voltage will be calculated and sent to the motor. The motors are then expected to move the belts to realise the speed or position control on the contact bar.

6.3 Pantograph identification by Frequency Response Function

As the development of the DO-based catenary model (the virtual catenary in HIL) requires the result of the pantograph–catenary simulation, the physical pantograph in the laboratory is required to be mathematically identified. As discussed in Chapter 2.2.1, the linear lumped-mass pantograph model is a mathematical abstraction rather than a physical representation of a pantograph, so the parameters generally need to be identified experimentally rather than based on the physical datasheets of components. In this section, the pantograph is identified by the Frequency Response Function (FRF).

The FRF is an effective method for understanding the dynamic behaviour of physical equipment (Wang, 2016). A common way to obtain FRF of a system is to excite the system by applied sinusoidal inputs. The input–output relationship is then analysed in the frequency domain, which can be derived by conducting Laplace transformation, as in Eqn. 6.3.1, where $Y(\omega)$ and

$U(\omega)$ are the Laplace transform of the output and input, respectively. The FRF result is the output per unit sinusoidal input at frequency ω.

$$G(\omega) = \frac{Y(\omega)}{U(\omega)} \tag{6.3.1}$$

For the pantograph identification task, a set of sinewaves to cover the frequency of interest is designed for the excitation. The contact force and the pantograph head acceleration are regarded as the system input and output, respectively, as both of them can be measured by independent sensors. As shown in Figure 6.3.1, for example, the variation of contact force (FRF input) and the pantograph head acceleration (FRF output) are plotted under the excitation of 10 Hz contact bar movement.

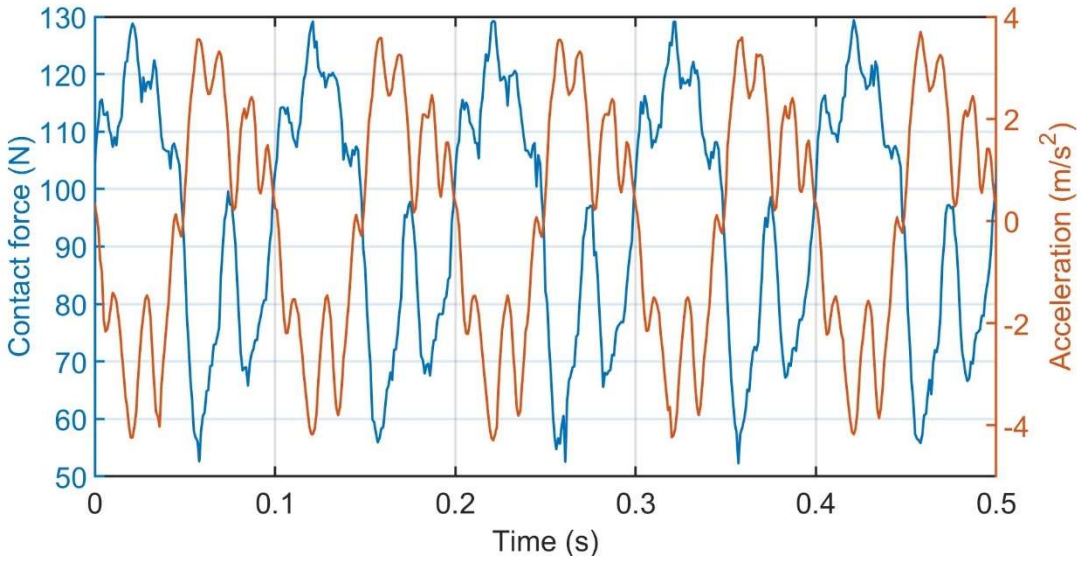


Figure 6.3.1. FRF input and output under 10 Hz contact bar movement

As FRF is usually used to model and identify linear systems (Wang, 2016), using it to identify a pantograph, a nonlinear system, has significant limitations. It can be noticed from excitation tests that different excitation profiles (i.e., amplitude) can exhibit different frequency responses (Xin, 2019). Hence, the veracity of the estimated linear model is limited to an operating

condition similar to the excitation profile. However, the benefit is obvious, so the linear model is preferred in controller design in active pantograph research.

In order to obtain a model with a reasonable excitation (frequency-amplitude) profile, the test rig movement is programmed according to the following steps.

1. The nominal contact wire height is 4700 mm (BSI, 2012); the Pendolino train height is 3560 mm; the pantograph in collapse is about 500 mm; so the nominal distance between the contact wire and the collapsed pantograph is 640 mm. The UoB test rig reaches the collapsed pantograph at the rig height of 200 mm. Therefore, the nominal contact height between the pantograph and the contact bar is 840 mm. The schematic working height diagram is shown in Figure 6.3.2.

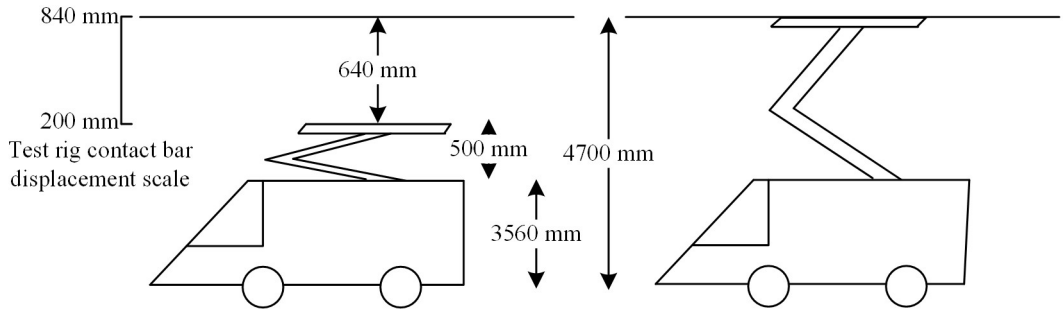


Figure 6.3.2. Nominal pantograph working height

2. The frequency of interest is up to 20 Hz and the FRF measurement step size is set as 0.2 Hz. At each frequency, the amplitude reduces with the increasing frequency as in Eqn. 6.3.2 (Xin, 2019). Compared to the original approach, the upper limit of 5 mm is released, so the low-frequency excitations come with large amplitudes, which is closer to the real-world situation.

$$A = \frac{5}{f} \tag{6.3.2}$$

3. At each excitation frequency, 30 cycles of excitation are imposed for the FRF experiment. Only the results of the last ten cycles are used in the frequency analysis to minimise the settling effect.

By exciting the pantograph with a series of sinewave signals, the force-to-acceleration response is separately measured and processed for each frequency point. The result containing 100 values is plotted in the Bode diagram against the excitation frequency, as shown in Figure 6.3.3.

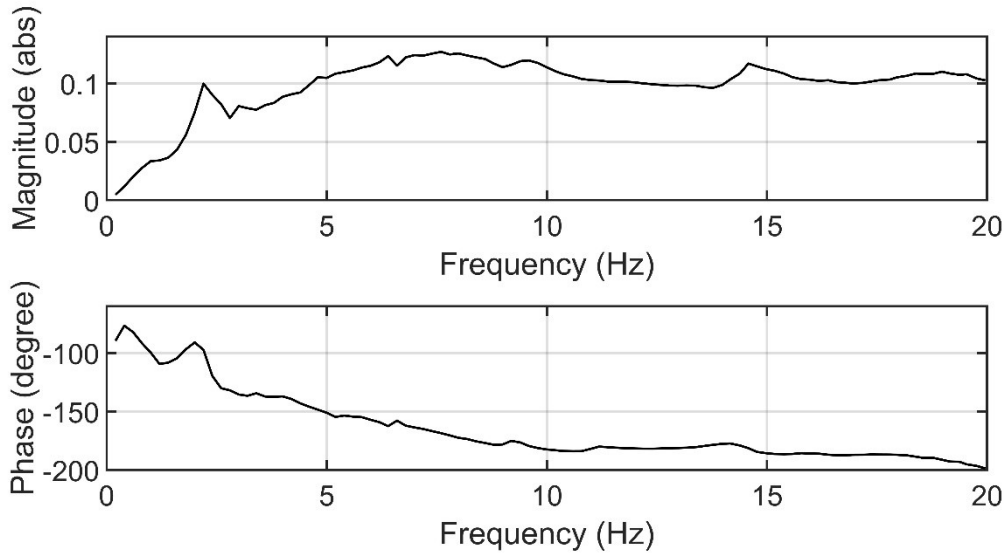


Figure 6.3.3. FRF of the physical pantograph (force-to-head-acceleration)

In the FRF result, at a frequency less than 2 Hz, the acceleration of the pantograph head is relatively resistant to the force. When high-frequency external force is exerted on the pantograph head, the acceleration is around one-tenth of the force in amplitude. Three resonances can be found, at around 2.2, 7.6, and 14.6 Hz.

Based on the FRF results, as a reference, the numerical model of the pantograph can be estimated by solving a nonlinear optimisation problem. The main idea is to build a model whose FRF is close to the reference. When trying to match the FRF reference, there is a trade-off to fit either magnitude or phase response (Xin, 2019). However, as the magnitude and phase are

both derived from the complex number through Fourier transformation, the Euclidean distance in the s-plane will be used to include both magnitude and phase information for the estimation.

Note that the pantograph identification by FRF is focused on fitting the response in the frequency domain, while the parameterisation method (Chapter 4.2.2) proposed for lumped-mass catenary models is focused on fitting the input-output result in the time domain.

A grey-box pantograph model (i.e., the three-mass model, as Eqn. 3.2.1) is used to fit the FRF results. By solving the nonlinear optimisation problem, the estimated model $G(\tilde{m}_i, \tilde{k}_i, \tilde{c}_i)$ is to be calculated whose transfer function $\tilde{G}(jw) = \tilde{a}(w) + \tilde{b}(w)j$ can reach the minimum of Eqn. 6.3.3. The optimisation solver used is 'fmincon' (Byrd et al., 2000).

$$J = \sum_{n=1,2\ldots} \left(\sqrt{(a_n - \tilde{a}_n)^2 + \left(b_n - \tilde{b}_n\right)^2} \right)^2 \tag{6.3.3}$$

To ensure a global optimum, a set of initial points are generated through a random sampling process; the range of sampled parameters is given in Table 6.3.1. Among these parameters, there are two that need to be carefully considered.

The lower-frame spring has a critical impact on the pantograph dynamics. When a physical pantograph works at different heights, the average contact force should not be significantly changed. However, if the lower-frame spring in the numerical model is estimated to be stiff, when the pantograph vertically moves along the catenary, the contact force will be significantly changed. Therefore, the lower-frame spring should be confined to a relatively small value compared to other springs.

The pantograph head mass in the numerical model is the only parameter that has a direct physical relationship with a physical pantograph. Therefore, it is worthwhile limiting the initial value to near the physical mass result, which is around 8.5 kg.

The optimisation process is performed for each sampled set, and at the end, the global minimum optimisation cost can be found. Figure 6.3.4 shows the error of the optimisation results for the 100 initial parameter sets, where the result with the 55^{th} set has the minimal difference to the reference. The corresponding estimated parameters are given in the last column of Table 6.3.1, and the estimated model's frequency response is compared with the reference in Figure 6.3.5. It shows that the frequency response of the estimated lumped-mass model has a good consistency with the physical pantograph, although some outliers can be noticed in the Bode diagram.

Table 6.3.1. Ranges of sampled initial parameters and results

Three-mass model	Coefficient	Minimum value	Maximum value	Estimated value
Lower frame	Mass (kg)	1	50	25.47
	Damper (Ns/m)	0.01	1000	154
	Spring (N/m)	1	500	60.75
Upper arm	Mass (kg)	1	50	4.06
	Damper (Ns/m)	0.01	1000	140
	Spring (N/m)	1	50000	1830
Head	Mass (kg)	1	20	10.82
	Damper (Ns/m)	0.01	1000	0.01
	Spring (N/m)	1	50000	5469

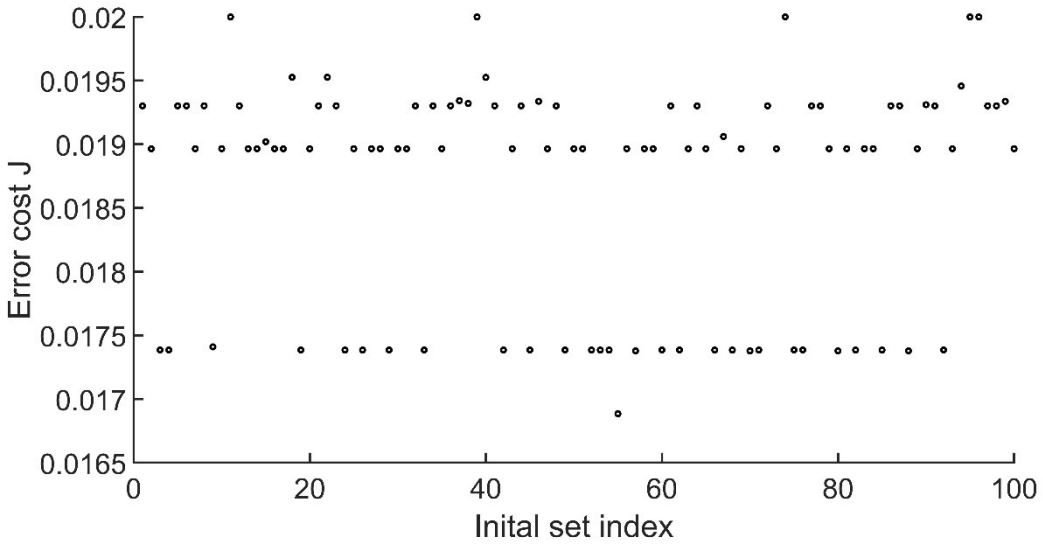


Figure 6.3.4. Error costs of the optimised results with the 100 initial parameter sets

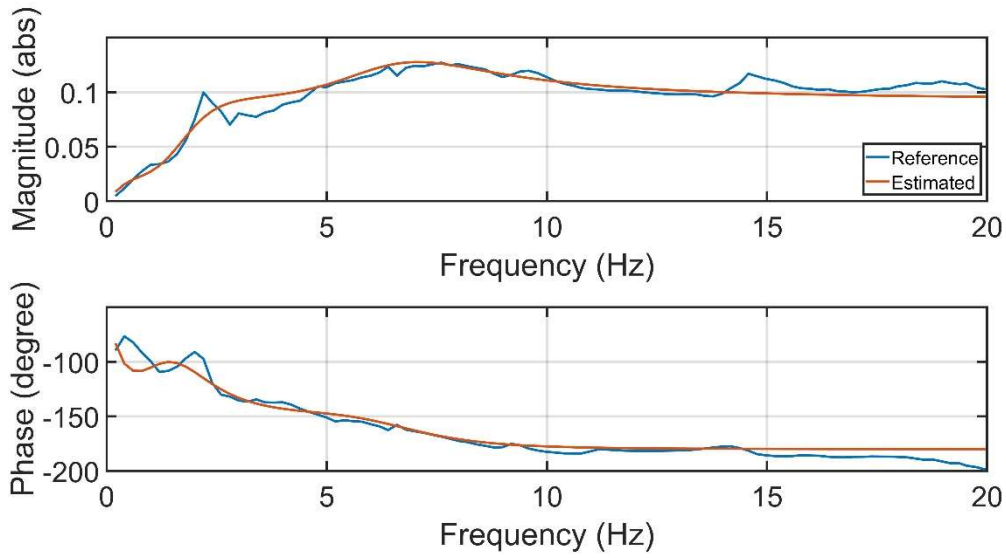


Figure 6.3.5. Comparison between optimised and reference results

6.4 The DO-based virtual catenary design

To realise the pantograph–catenary HIL experiment, it is necessary to build a virtual catenary model. As the computational speed of the virtual catenary must be faster than real time, it is unrealistic to use the original FE catenary model. Recently, to improve FE-based simulation efficiency, a few methods which can be applied to realise pantograph HIL experiments have

been developed by scholars (Gregori et al., 2017, Gregori et al., 2019, Kobayashi et al., 2019, Song et al., 2019).

In this thesis, the DO catenary model proposed in Chapter 4.3 will be used as the virtual catenary model. To build a DO-based catenary model, acquisition of the pantograph–catenary simulation results is a prerequisite. The pantograph model identified in Chapter 6.3 is simulated with the FE catenary model developed in Chapter 3. The simulation results of contact wire displacement and contact force are presented in Figure 6.4.1 and Figure 6.4.2.

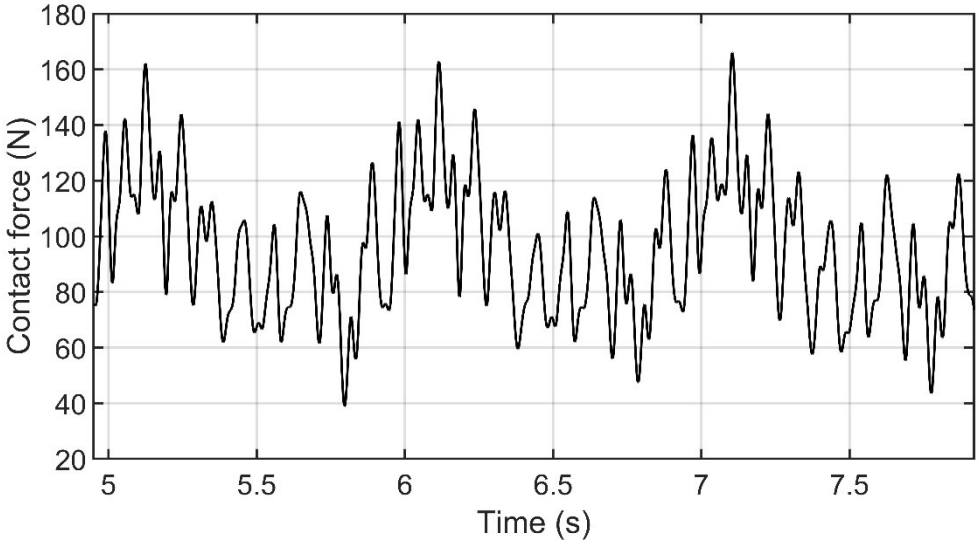


Figure 6.4.1. Contact force in the simulation with the identified pantograph model

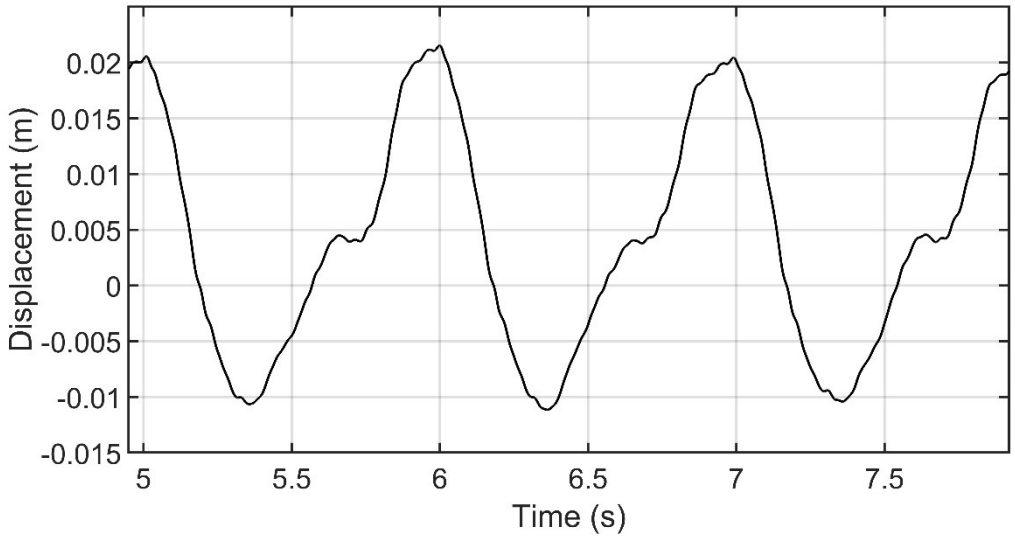


Figure 6.4.2. Contact wire displacement with the identified pantograph model

The DO-based catenary model can be designed according to the procedure presented in Chapters 4.2.2 (parameterisation) and 4.3(disturbance augmentation). As the pantograph model and thus the dynamic response of the catenary has been changed, the catenary parameterisation needs to be re-performed. The derived lumped-mass parameters are listed in Table 6.4.1, and the estimated and reference results are compared in Figure 6.4.3. The disturbance is presented in Figure 6.4.4. By augmenting the disturbance signal with the linear catenary model, the DO catenary is built.

Table 6.4.1. Parameterisation constraint and result for the HIL virtual catenary

Coefficient	Minimum value	Maximum value	Estimated value
Mass	1	200	84.71
Damper	1	300	175.87
Spring	1000	6000	2674

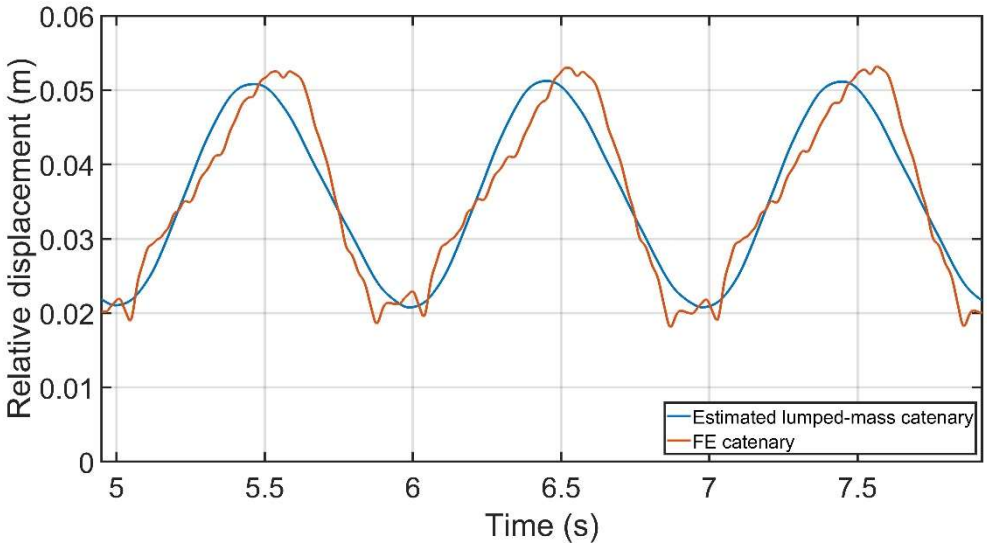


Figure 6.4.3. Contact wire relative displacement with FE and estimated catenary models

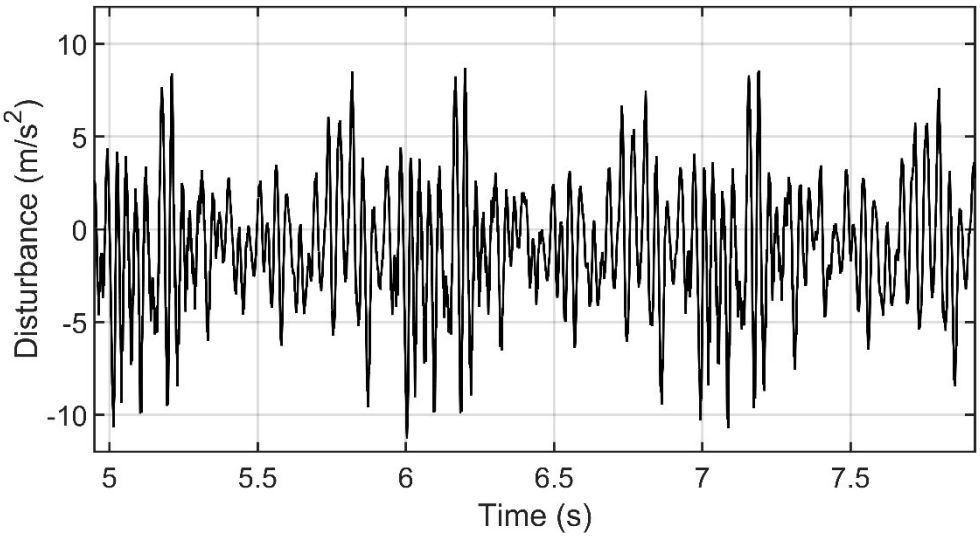


Figure 6.4.4. Estimated lumped disturbance

6.5 HIL design and validation

In this section, the HIL operation model of the test rig is developed, where the contact bar movement becomes a function of the contact force (following the behaviour of the virtual catenary). It should be noted that the virtual catenary does not represent the behaviour of a contact wire section but the contact point along the catenary when a train is moving. As shown

in Figure 6.5.1, five functions are set up for the HIL control loop: data collecting, feeding, simulating, sending and executing.

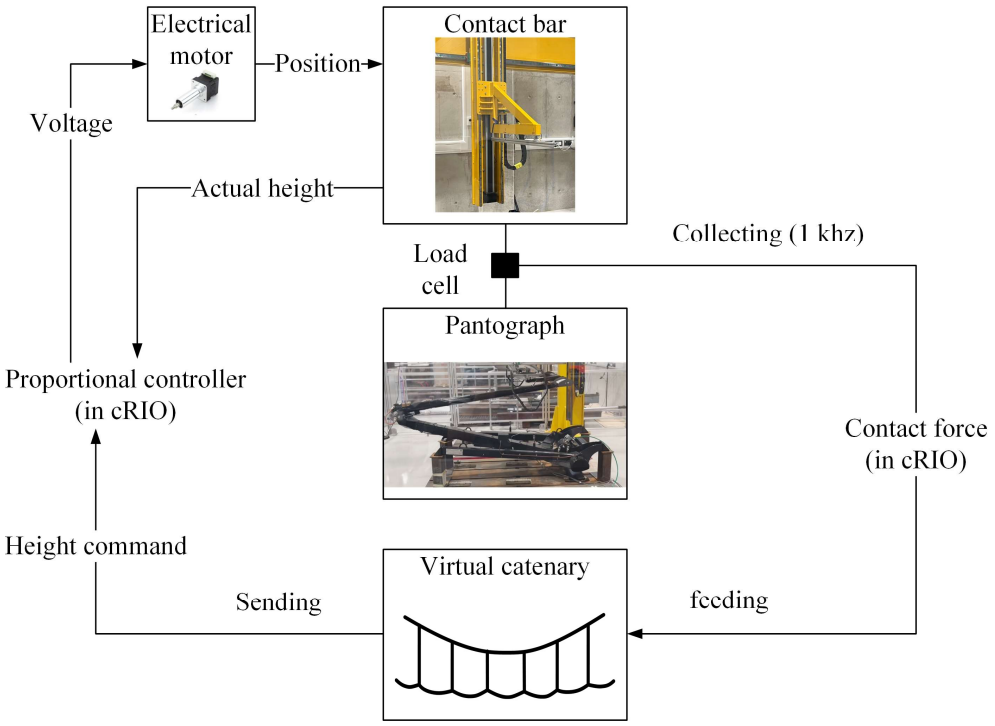


Figure 6.5.1. HIL control command flow

The five functions are introduced below, and the related parameters are discussed.

- Contact force collection from load cells to cRIO (control cabinet)

The acquisition of data from sensors is performed on the cRIO module, whose sampling rate is set as 1 kHz.

- Force data feeding to the virtual catenary block

Once the contact force data are collected in the cRIO, the host PC calls this function to read data and feed it to the virtual catenary model. As the contact force is required to be processed in real time in the HIL experiment, the data are directly communicated through a variable

between cRIO and PC instead of saved into FIFO (first-in-first-out) buffers. In this way, only the contact force will be used in the HIL so that significant CPU resource can be saved.

If the force feeding rate is too low, it may cause a sudden change in the virtual catenary behaviour. However, the feeding rate is limited by the host PC's computation capability.

- Virtual catenary simulation step size

The contact force is filtered and processed in the virtual catenary block. The data go through the DO-based catenary model, and the displacement of the contact wire is produced. The simulation step size affects the accuracy of the virtual catenary in reproducing the FE catenary behaviour. Compared to other functions in the HIL, the simulation block takes up fewer CPU resources. Even though a high simulation rate is configured, the movement of the test rig is mainly constrained by the command sending rate and test rig movement settings.

- Virtual catenary displacement command sending rate to the test rig

The displacement data are then sent to the cRIO for commanding the test rig. The command sending rate is critical to the accuracy of the contact bar movement. If the rate is low, the test rig can only update the virtual catenary height after a large time interval, and thus the test rig may move suddenly up and down. This unsmooth movement cannot reproduce the contact point displacement but also results in extreme contact force and loss of contact when the pantograph is activated. Therefore, the command feeding rate is the most critical parameter. Within current hardware resources, the maximum command sending rate is 10 ms.

- Test rig movement control parameters

Once the cRIO module receives the height command, the motor is activated to move the rig belt. The test rig contact bar position control is realised by a proportional controller. The role of the control parameter is simply as a common proportional gain in a closed-loop plant. Ideally, in order to ensure accurate and smooth height control, a relatively large gain needs to be applied. However, the value cannot be very big, because if the test rig moves to the set point a very short time (rise time) before the next command is sent into the cRIO, the overshoot can make the test rig movement unsmooth and thus result in extreme contact force. Therefore, based on experimental trials, if the command sending rate is set as 10 ms, a reasonable proportional gain is 25.

The four HIL parameters discussed above are summarised in Table 6.5.1. Among them, the height command sending rate is the most important, and the contact force feeding rate is set as the same as the sending rate to ensure simultaneous data exchange between the host PC and cRIO. The virtual catenary simulation step size is set to 2 ms.

Table 6.5.1. Summary of HIL parameters

	Contact force feeding	Virtual catenary simulation	Height command sending	Test rig control proportional gain
Importance	Medium	Low	High	High
Constrained by	CPU capability	CPU capability Required simulation bandwidth	CPU capability	Height sending rate
Rate/value	10 ms	2 ms	10 ms	25

Once the HIL operation mode is set up, two experimental cases are conducted to examine the HIL performance: with and without-a-pantograph operation. In the without-a-pantograph case, the pantograph is not activated and involved.

As shown in Figure 6.5.2, the contact force will not be collected from the sensors. The contact force data used to excite the virtual catenary come from a pre-loaded lookup table, which is identical to the contact force result in the FE catenary simulation. The contact force lookup table repeats the mid-span data of the simulation force result, which ensures the HIL can keep fabricating the mid-span catenary behaviour. A comparison of the contact wire displacement between the FE-based simulation and HIL experiment is presented in Figure 6.5.3.

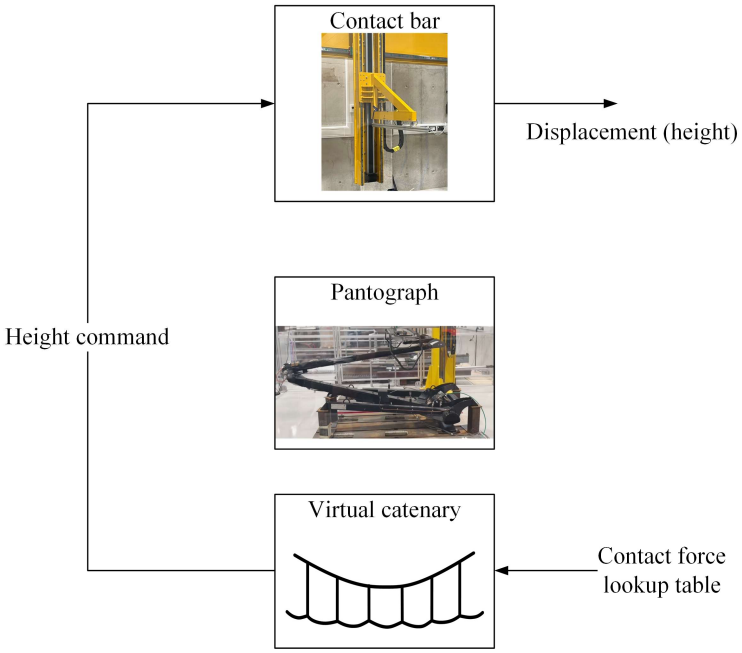


Figure 6.5.2. HIL validation: without-a-pantograph

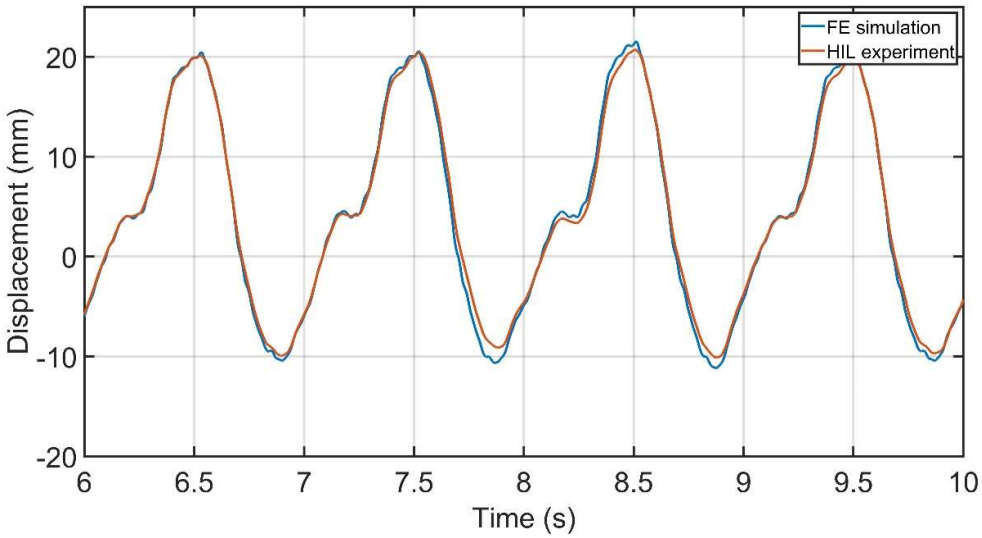


Figure 6.5.3. Without-a-pantograph displacement result

The difference between the FE-based simulation and the HIL experiment is negligible. The difference is mainly caused by the limited height command sending rate and the constrained test rig control gain. Despite the error due to the hardware limitation, the results evidence that the DO-based catenary is a computationally efficient, accurate method for the pantograph–catenary HIL.

In the with-a-pantograph case, the contact force lookup table is replaced by the real-time data collected from the load cells, as shown in Figure 6.5.4. The generated contact force and contact bar displacement are presented in Figure 6.5.5 and Figure 6.5.6.

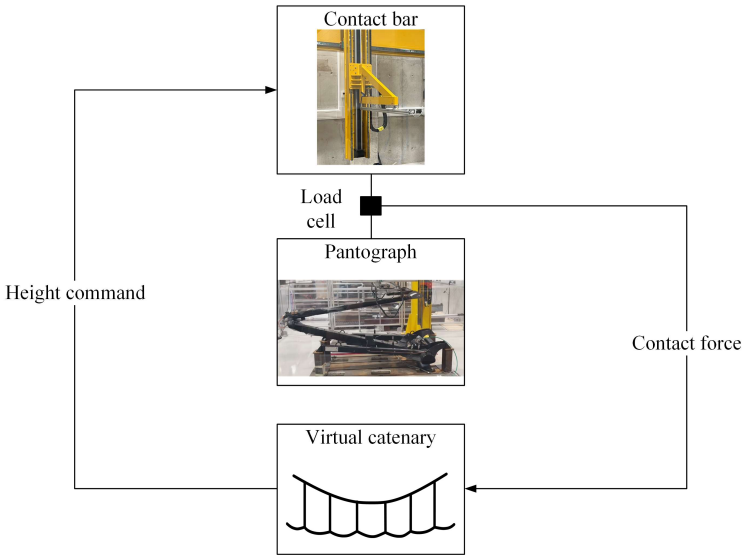


Figure 6.5.4. HIL validation: with-a-pantograph

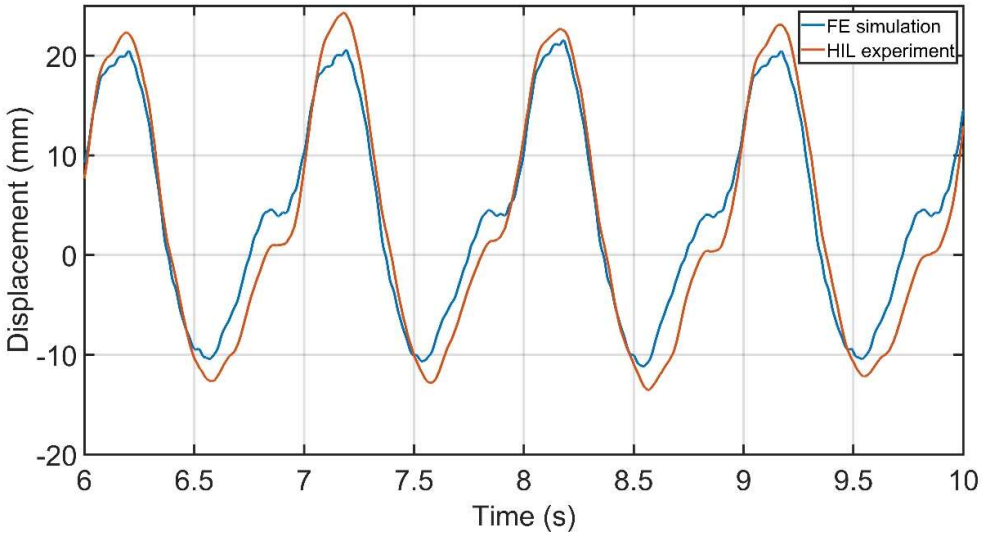


Figure 6.5.5. With-a-pantograph displacement result

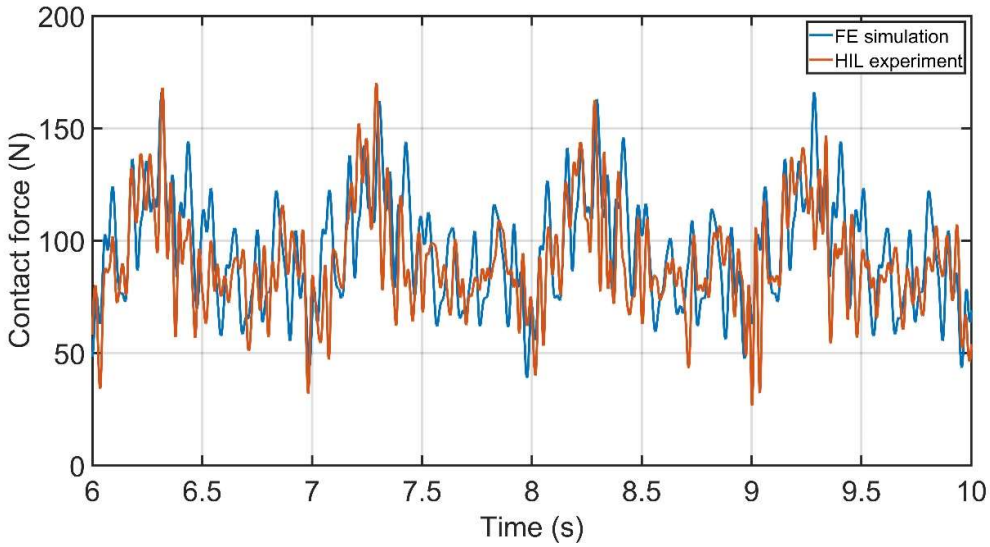


Figure 6.5.6. With-a-pantograph contact force result

Unlike the without-a-pantograph case, the difference between the FE-based simulation and the HIL experiment is relatively apparent. It is considered that the modelling error of the pantograph and the penalty contact model are the main reasons for the discrepancy since the ability of the virtual catenary to reproduce the FE catenary dynamics has been demonstrated in the without-a-pantograph case. As a physical pantograph and real mechanical contact are used in the HIL, the result of the HIL now becomes the source of truth. The result also indicates that the HIL with a physical pantograph is important for the pantograph study.

6.6 Active pantograph in HIL

The test rig HIL mode has been developed and validated with the case of the passive pantograph. To realise an active pantograph, the installation of the actuator for the pantograph will be discussed first. As discussed in the literature review, although the frame-actuated active pantograph has the advantage of being easy to install, it has not yet been realised in the closed-loop HIL situation, so the lower-frame actuator is considered.

A straightforward way to apply the force on the lower frame is through the pneumatic channel by the compressed air, which is used to excite the pantograph to reach the contact wire and supply contact force. By modifying the pressure of the compressed air, the uplift force on the pantograph can be changed. The advantage of this approach is that the original design of the pantograph can be retained as much as possible. No safety functions are compromised by installation of the active unit. The only modification is placing a pressure regulator between the air supply and the pantograph. It should be noted that the pantograph itself is equipped with a manual pressure valve, which has to be opened to the maximum to allow the pressure to be fully controlled by the regulator. Also, in the laboratory, an air compressor is used to supply the compressed air, whose valve also has to be fully opened. The airflow of the active pantograph in the laboratory is shown in Figure 6.6.1 and Figure 6.6.3.

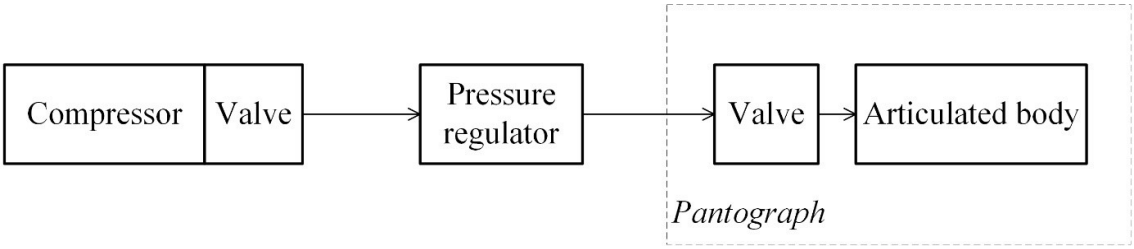


Figure 6.6.1. Schematic of flow of compressed air

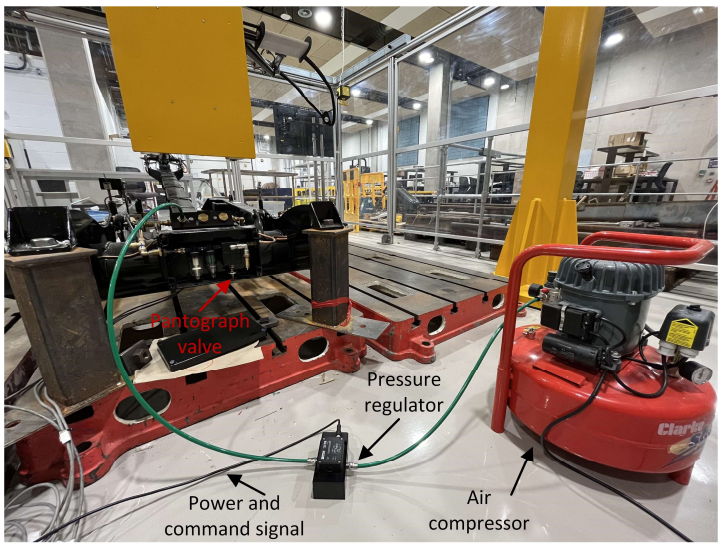


Figure 6.6.2. Flow of compressed air

The pressure regulator used for the active pantograph in the laboratory is a model TR-025-g10-s manufactured by Enfield Technologies. This regulator is one of the fastest and most accurate electronic regulators available on the market. It has a pressure range of 0–10 bar, which is enough for pantograph control (a typical pressure for a passive pantograph is about 5 bar). The pneumatic pressure is proportional to the command voltage supplied to the regulator, through which the pressure in the pantograph can be controlled by the test rig. For more information about the regulator, please refer to the product datasheet (Enfield Technologies, 2022).

For the original design of the pantograph, the pressure cannot be kept constant when the pantograph is moving (because of the airflow). Once a regulator is placed, it starts to maintain the pressure so the introduction of the electronic regulator changes the dynamics of the (passive) pantograph. In addition, the HIL behaviour may need to be included when designing a controller for the pantograph that interacts with the test rig. Therefore, linearisation of the whole open-loop system should be conducted for the active pantograph controller design.

As shown in Figure 6.6.3, the open-loop system starts with the pressure command, which will be sent to the electronic pressure regulator via a voltage signal. The time-varying pressure of the compressed air will excite the pantograph to interact with the contact bar, and the contact force can be obtained. The pressured command is constructed by Eqn. 6.6.1, where CF is the contact force result of the passive pantograph HIL experiment, 95 is the contact force set point, 5.22 is the passive pantograph pressure set point and 0.005 is the tentative controller gain. With the fabricated pressure command, the open-loop system can be excited, assuming there is a contact force controller.

$$Input = 0.005 \times (95 - CF) + 5.22 \tag{6.6.1}$$

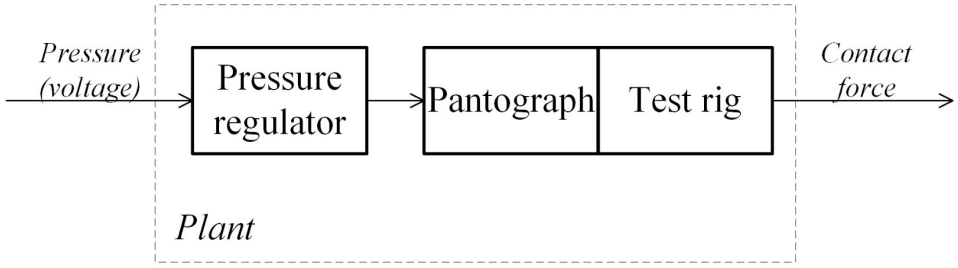


Figure 6.6.3. The open-loop system

With the system input and output signals, the open-loop system can be linearised. Compared to the system identification tasks for the pantograph and catenary models discussed in Chapters 6.3 and 6.4, this system identification aims to identify a black box rather than to conduct parameterisation. The system identification finds the best Autoregressive with Extra Input (ARX) model to match the input and output signals. The ARX model can be further converted to a continuous model for the controller design. For more information about the ARX model and identification, please refer to (Mathworks, 2022).

The input (pressure command) and output (contact force) of the open-loop system are presented in Figure 6.6.4. As it is suggested by Bruni et al. (2018) that the bandwidth of the lower-frame actuated scheme is limited to less than 2 Hz, the input and output signals will be pre-filtered by a low-pass filter of 5 Hz passband (it is also in line with the filter for the force feedback presented in (Facchinetti and Mauri, 2009)) for a better system identification result that is focused on the controller design.

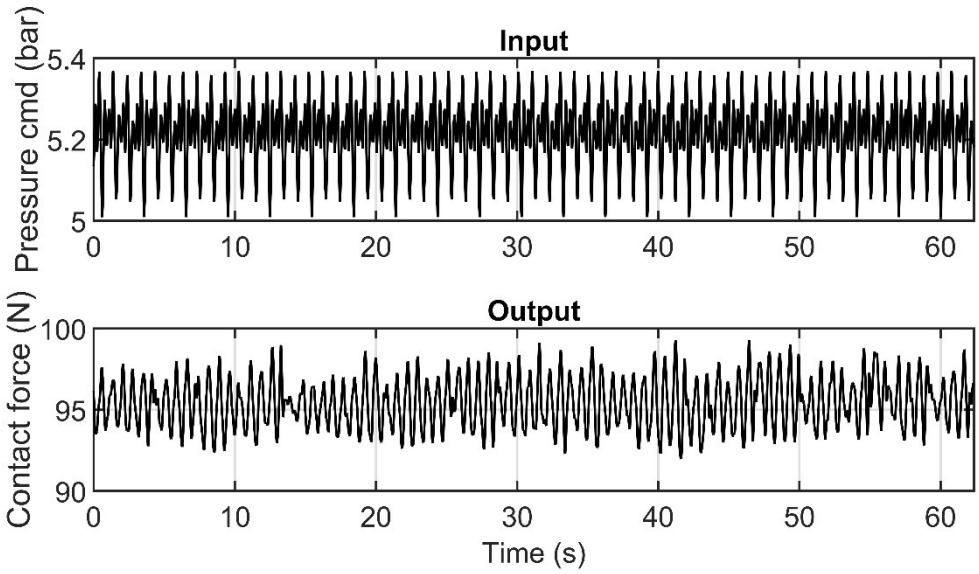


Figure 6.6.4. Data for plant identification

The optimised ARX model that fits the experiment result is derived, whose distribution of error is presented in Figure 6.6.5. The error distribution is close to normal with a mean of zero, although the absolute value of the error is large considering the output range. The model is then converted into a continuous linear model for the controller design. The transfer function and the frequency response of the identified plant model are presented in Eqn. 6.6.2 and Figure 6.6.6.

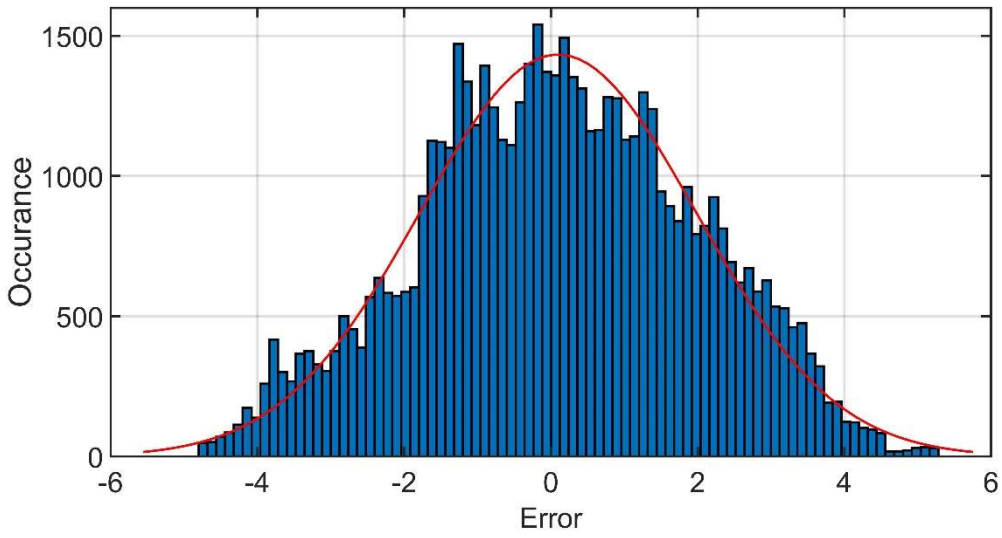


Figure 6.6.5. Distribution of model error

$$G(s) = \frac{1.151e^{-10}s^6 + 2.828e^{-7}s^5 + 0.0005209s^4 + 0.7074s^3 + 673.8s^2 + 4.044e^5 s + 1.156e^8}{s^6 + 6.727s^5 + 1362s^4 + 7281s^3 + 3.03e^5 s^2 + 7.079e^5 s + 6.323e^6} \quad (6.6.2)$$

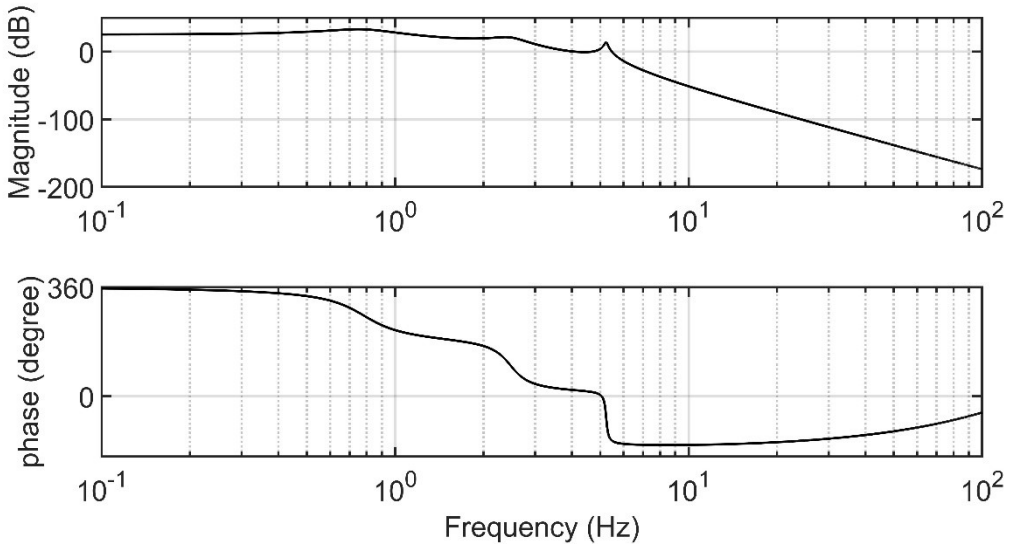


Figure 6.6.6. Frequency response of the estimated model

Based on the linearised model of the system, the controller can be designed to regulate the contact force. Considering the pros and cons of the controllers summarised in Chapter 5.6, a second-order phase-lead compensator is designed for the active pantograph because of its simple structure and effectiveness.

The design aim of the phase-lead controller is to attenuate the disturbance response at a frequency between 1 and 2 Hz (considering the capability of the actuator placed on the lower frame of the pantograph). The design also considers the hardware limitation of the pantograph and control actuator, where the air pressure is confined in 0–10 bar and cannot change greatly in a short time. The transfer function of the designed phase-lead compensator is shown in Eqn. 6.6.3. The controller increases 135 degrees at 1.44 Hz on the open-loop response. With the controller, the closed-loop disturbance rejection performance is presented in Figure 6.6.7. It is expected that the contact force variation from the HIL experiment would be attenuated by −0.1 dB at 1–2 Hz.

$$C(s) = \frac{0.03s^2 + 0.1093s + 0.0996}{s^2 + 90.2s + 2034.01} \tag{6.6.3}$$

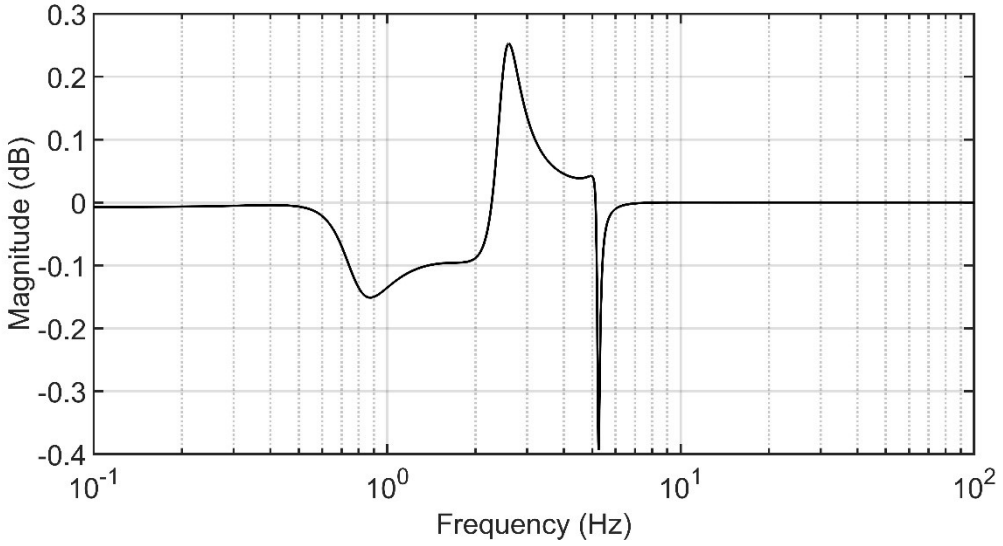


Figure 6.6.7. Disturbance rejection performance of the closed-loop system

The designed controller is first validated with the augmented disturbance in simulation. The controller is effective in reducing the disturbance impact on the contact force as analysed in the frequency domain in Figure 6.6.7. The result is presented and compared with the HIL result in Table 6.6.1.

The active pantograph HIL experiment is then conducted. The contact force between the pantograph and the contact bar is compared with the passive pantograph case in the time domain in Figure 6.6.8 and the frequency domain in Figure 6.6.9. The contact force metrics are presented in Table 6.6.1, where the results are measured for 60 seconds to reduce the influence of experimental errors. It can be seen from the results that the active controller can reduce contact force fluctuation, as expected in the mathematical analysis and shown in the simulation, although the improvement is not significant. The result in simulation is similar to the actual performance in the HIL experiment, although the difference exists due to the nonlinearity of the pantograph (which has also been shown in the passive pantograph case). The validation in

simulation is demonstrated to be a useful intermediate step between the controller design and validation in HIL.

The incapability to deliver better active pantograph performance will be discussed in the following section.

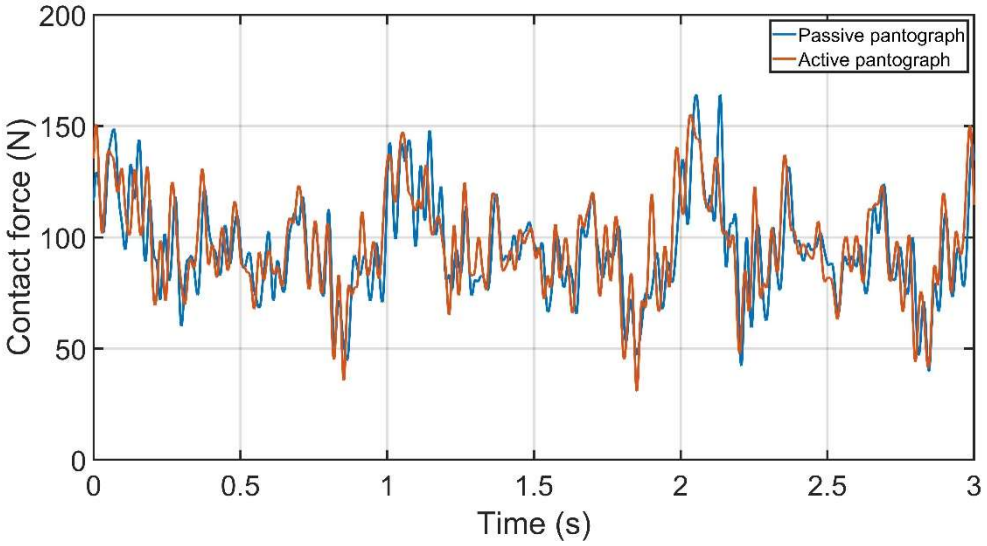


Figure 6.6.8. Contact force of the active pantograph in HIL

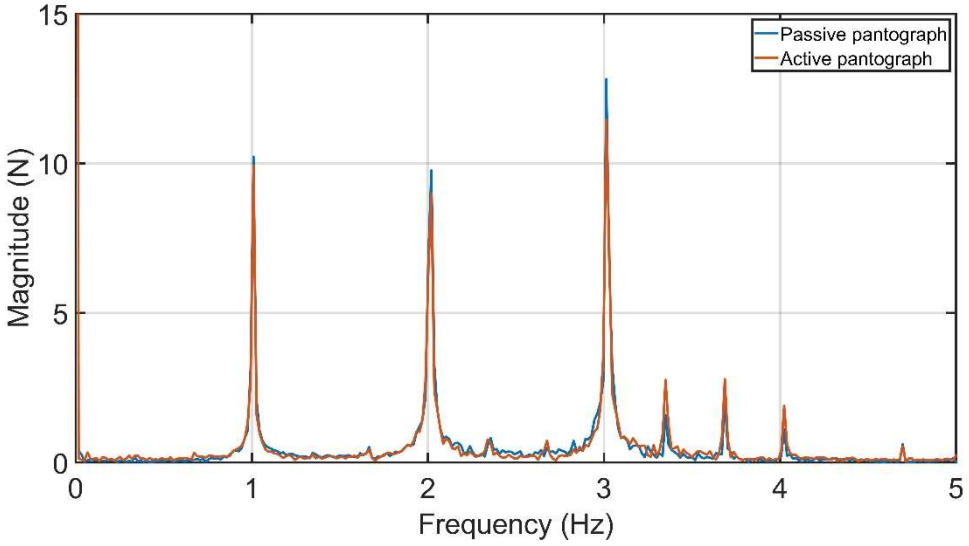


Figure 6.6.9. Contact force spectrum of the active pantograph in HIL

Table 6.6.1. Metrics of the contact force with the active pantograph

Contact force	Validation in simulation		Validation in HIL	
	Passive pantograph	Active pantograph	Passive pantograph	Active pantograph
Standard deviation (N)	23.99	23.85	22.08	21.40
Minimum (N)	39.50	39.43	27.41	30.89
Maximum (N)	166.40	166.14	175.83	172.93
Magnitude at 1 Hz (N)	20.11	19.81	10.13	9.71
Magnitude at 2 Hz (N)	10.54	10.43	9.92	8.99

6.7 Summary and conclusion

This chapter focused on the pantograph HIL experiment. To realise this experiment, the contact between the pantograph and contact wire was reproduced by a moving contact bar whose motion follows the dynamics of a catenary model. The virtual catenary was generated by means of the DO based on the pantograph–catenary simulation result. To ensure authentic pantograph–catenary dynamic behaviour can be obtained and thus used for the DO-based catenary design, the physical pantograph was identified in Chapter 6.2 as a lumped-mass model and simulated with an FE catenary model in Chapter 6.3. The HIL experiment result in Chapter 6.4 showed that the contact bar can well represent the dynamics of the designed virtual catenary.

The active pantograph was realised by placing an electronic pressure regulator between the pantograph and the supply of compressed air. The pressure in the pantograph can then be changed based on the real-time contact force. To design an active controller based on the system model, the whole system was linearised by system identification and then a phase-lead compensator was designed, to attenuate the disturbance response for the frequency of 1–2 Hz.

Comparing the HIL results of the designed active pantograph with that of the passive pantograph, the spectrum of the contact force between 1–2 Hz was found to be reduced as expected.

It has been shown that a model-based and frame-actuated active pantograph has been designed and tested in the HIL laboratory experiment. However, although the active controller was effective in reducing contact force fluctuation, as expected in the mathematical analysis and the validation in simulation, the improvement is limited. The limited actuator bandwidth and modelling error are suspected to be the most important factors in limiting the active pantograph performance.

The use of an electronic pneumatic pressure regulator can retain the original mechanism and safety functions of the pantograph. However, its control bandwidth has a very limited effect on reducing the standard deviation of variations in contact force, considering that the contact force fluctuation is dominated by the dropper-passing frequnecy (at around 10 Hz). As the pantograph has strong nonlinear characteristics, the effect of control input (air pressure) on the output is nonlinear. Therefore, when the whole open-loop system (consisting of the pantograph, pressure regulator and test rig) is linearised by the system identification, the model is subject to considerable errors. It is recommended that the model-based active pantograph design should be further studied with more accurate modelling methods, such as nonlinear ones. Meanwhile, other types of actuators (it is better if the actuator has a linear effect on the contact force) can be considered for the model-based active pantograph design.

CHAPTER 7 CONCLUSIONS

This chapter concludes the thesis by summarising the key research findings. It also proposes opportunities for future research, based on the findings and limitations of the study.

7.1 Summary of the findings

The proportion of electrified railways has been gradually increasing around the world because of their high energy efficiency and capability to use renewable energy sources. The high quality of the current collection for electric trains is realised via interrupted mechanical contact between conductors. The most popular electricity collection equipment is the pantograph, and contact quality between the pantograph and the overhead contact wire is essential for electric trains. However, as the pantograph relies upon an open-loop mechanism to perform its daily functions, the pantograph–catenary contact force fluctuates wildly, and contact may even be lost when the train moves at high speed or under external interference. Therefore, active pantograph design is widely studied to improve the robustness of the pantograph–catenary interaction.

The literature review has revealed that current active pantograph research has the issue that many of the proposed controllers are not properly validated. In addition, those that are tested in the laboratory are not designed using a model-based approach (which is favoured in this thesis). Specifically, the simple lumped-mass catenary model has led to many active pantographs being developed, but a controller validated with a lumped-mass catenary with time-varying parameters tends to produce over-optimistic results. Few active pantograph studies have been validated with accurate catenary models (such as FE catenary). Even so, most of them use PID controllers but are not tuned/designed based on the mathematical model of the pantograph–

catenary system. Furthermore, at the laboratory stage, only a very limited number of validation works regarding physical active pantographs have been carried out and tested using HIL. None of these has used a model-based design approach, and the active pantographs concerned were not frame-actuated.

Considering the above research gaps, a new design and complete test approach for the active pantograph has been proposed. The approach suggested follows the typical model-based control design process, which includes system modelling, controller design and validation (in simulation and the laboratory).

In the first part of the thesis, and prior to the discussion on the model-based design approach, a pantograph–catenary model and comprehensive simulation framework are developed and validated in Chapter 3; the results are used as a source of truth not only for the design of the lumped-mass catenary models, but also for the veracity evaluation of the DO-based model. The combination of the lumped-mass pantograph, FE-based catenary and penalty contact model is used for modelling as it has dominated modelling focusing on pantograph–catenary dynamics. The models are coded in Matlab-Simulink and simulated within a designed framework which can be executed to calculate the static and dynamic behaviours of the pantograph–catenary model. The simulation result has been validated against the European norm and a benchmark paper for pantograph–catenary study.

A novel DO-based catenary model for active pantograph validation has been proposed and compared with the often-used classic approach in Chapter 4. The DO-based catenary model was developed by using the DO to extract the dynamic information of the FE catenary and augmenting the information with the linear catenary model to reproduce the dynamic behaviour exhibited in the FE catenary. In the open-loop (passive pantograph) simulation, the DO-based

catenary model was found to deliver contact force results which were nearly identical to those obtained from the FE model (which was considered as the source of truth). This performance was a significant improvement on those for the classic time-varying lumped-mass model. The accuracy of the new model for predicting closed-loop performance was also evaluated with an active pantograph (using a PID controller tuned based on a linear system model). The control input and output results with the DO-based model were found to be similar to that with the FE catenary. Hence, it is concluded that the proposed DO-based catenary is a suitable model for active pantograph validation purposes.

In Chapter 5, the design and validation of a model-based active pantograph was presented. Simulation results were generated and examined from a variety of control methods ranging from the classical control method to the state-of-the-art DO-based SMC. It was shown that all the active controllers can reduce the pantograph–catenary contact force standard deviation as they are expected to at the design stage. It is concluded that the active pantograph designed based on the linearised pantograph–catenary model is effective in reducing contact force fluctuation when validated with accurate catenary models. This was verified by simulating each controller applied to the FE model, confirming that the system input and output changes with the DO-based catenary model are representative of those with the FE catenary, even with different control laws. Hence, the DO-based catenary model is confirmed to be an effective approach for active pantograph validation (on the condition that the magnitude of control input is practically reasonable). Considering the trade-off between effectiveness and complexity of the controller, the phase-lead/lag compensator was selected as the candidate for the model-based active pantograph design and implementation in the laboratory.

Chapter 6 was focused on the active pantograph HIL experiment. To realise this experiment, the pantograph test rig was used, allowing the contact between the pantograph and contact wire

to be reproduced by a moving contact bar whose motion follows the dynamics of a virtual catenary model. The virtual catenary was modelled by means of the DO based on the pantograph–catenary simulation. The active pantograph was realised by using an electronic pressure regulator to control the pressure within what was otherwise a standard passive pantograph. In order to design the active controller based on the linear system model, the whole system was linearised by system identification, and then using that model a phase-lead compensator was designed. Comparing the HIL results of the designed active pantograph with those of the passive pantograph, it was found that the spectrum of the contact force between 1–2 Hz is reduced (as expected at the design and simulation stages).

7.2 Discussions and recommendations for future work

It has been shown that the classic time-varying lumped-mass catenary is not sufficient to represent the system dynamics exhibited in the catenary system. Besides that, it is difficult for the classic lumped-mass catenary model to incorporate the external operational conditions, such as strong wind and carbody vibration. Instead, by virtue of using a DO, the DO-based model is able to demonstrate the complex catenary dynamics and it is possible to incorporate external disturbance. Moreover, the real-world contact force data can also be used to develop a DO-based catenary model for the simulation and HIL experiment to improve the authenticity. Therefore, the DO-based catenary model is recommended to replace the role of the classic lumped-mass catenary model for active pantograph validation.

A model-based and frame-actuated active pantograph has been designed and tested in the HIL laboratory experiment. However, its effectiveness in reducing contact force fluctuation is limited. The most probable factor that restricts the active pantograph's performance is believed to be the modelling error, in addition to the limited control bandwidth of the pneumatic

auctuator. As the pantograph has strong nonlinear characteristics, the effect of control input on the output through compressed air is nonlinear. Therefore, when the whole open-loop system is linearised by the system identification, the model is subject to considerable errors. It is recommended that the model-based active pantograph design should be further studied with more accurate modelling methods, such as nonlinear ones.

A further limitation on performance, was almost certainly the use of a pneumatic actuator built into the pantograph, which is difficult to model and control. Other types of actuators (it is better if the actuator has a direct and linear effect on the contact force) could be considered to control the pantograph actively.

Furthermore, the design and installation of active pantographs in this thesis are based on the conventional passive pantograph. However, since the pantograph is actively controlled to regulate the contact force, complete replacement of the original pantograph articulated structure and the pneumatic working mechanism might be considered. It is suggested that, in the future, new generations of pantographs specifically designed for active control should be extensively investigated.

LIST OF REFERENCES

ABBOTT, M. 1967. *A Numerical Method for Calculating the Dynamic Behaviour of a Simple Catenary Overhead Contact System for Electric Railway Traction*. Technical Report 67156. Royal Aircraft Establishment.

ABDULLAH, M. A., MICHITSUJI, Y., NAGAI, M. & MIYAJIMA, N. 2010. Integrated simulation between flexible body of catenary and active control pantograph for contact force variation control. *Journal of Mechanical Systems for Transportation and Logistics*, 3, 166-177.

ALLOTTA, B., PUGI, L. & BARTOLINI, F. 2008. Design and experimental results of an active suspension system for a high-speed pantograph. *IEEE/ASME Transactions on Mechatronics*, 13, 548-557.

AMBRÓSIO, J., POMBO, J., ANTUNES, P. & PEREIRA, M. 2015. PantoCat statement of method. *Vehicle System Dynamics*, 53, 314-328.

AMBRÓSIO, J., POMBO, J. & PEREIRA, M. 2013. Optimization of high-speed railway pantographs for improving pantograph-catenary contact. *Theoretical and Applied Mechanics Letters*, 3, 013006.

AMBRÓSIO, J., POMBO, J., PEREIRA, M., ANTUNES, P. & MÓSCA, A. 2012a. A computational procedure for the dynamic analysis of the catenary-pantograph interaction in high-speed trains. *Journal of Theoretical and Applied Mechanics*, 50, 681-699.

AMBRÓSIO, J., POMBO, J., PEREIRA, M., ANTUNES, P. & MÓSCA, A. 2012b. Recent developments in pantograph-catenary interaction modelling and analysis. *International Journal of Railway Technology*, 1, 249-278.

AMBRÓSIO, J., POMBO, J., RAUTER, F. & PEREIRA, M. 2009. A memory based communication in the co-simulation of multibody and finite element codes for pantograph-catenary interaction simulation. *In:* BOTTASSO, C. L. (ed.) *Multibody Dynamics*. Computational Methods in Applied Sciences, vol 12. Springer.

ANDREWS, H. 1964. Third paper: Calculating the behaviour of an overhead catenary system for railway electrification. *Proceedings of the Institution of Mechanical Engineers, Part F: Journal of Rail and Rapid Transit*, 179, 809-846.

ANTUNES, P., AMBRÓSIO, J., POMBO, J. & FACCHINETTI, A. 2019. A new methodology to study the pantograph–catenary dynamics in curved railway tracks. *Vehicle System Dynamics*, 58, 425-452.

ANTUNES, P., MÓSCA, A., AMBRÓSIO, J., POMBO, J. & PEREIRA, M. 2012. Development of a computational tool for the dynamic analysis of the pantograph–catenary interaction for high-speed trains. Proceedings of the 11th International Conference on Computational Structures Technology. Civil-Comp Press, Stirlingshire.

ÅSTRÖM, K. J. & MURRAY, R. M. 2021. *Feedback Systems: An Introduction for Scientists and Engineers*. Princeton University Press.

BALDAUF, W., KOLBE, M. & KROETZ, W. 2005. Closed-loop controlled pantograph for high-speed applications; Geregelter Stromabnehmer fuer Hochgeschwindigkeitsanwendungen. *Elektrische Bahnen-EB*, 103, 225-230.

BALESTRINO, A., BRUNO, O., LANDI, A. & SANI, L. 2000. Innovative solutions for overhead catenary-pantograph system: Wire actuated control and observed contact force. *Vehicle System Dynamics*, 33, 69-89.

BAUTISTA, A., MONTESINOS, J. & PINTADO, P. 2016. Dynamic interaction between pantograph and rigid overhead lines using a coupled FEM—multibody procedure. *Mechanism and Machine Theory*, 97, 100-111.

BEMMENT, S. D., GOODALL, R. M., DIXON, R. & WARD, C. P. 2018. Improving the reliability and availability of railway track switching by analysing historical failure data and introducing

functionally redundant subsystems. *Proceedings of the Institution of Mechanical Engineers, Part F: Journal of Rail and Rapid Transit*, 232, 1407-1424.

BOSLEY, J. R., EDGAR, T. F., PATWARDHAN, A. A. & WRIGHT, G. T. 1992. Model-based control: A survey. *In:* NAJIM, K. & DUFOUR, E. (eds.) *Advanced Control of Chemical Processes 1991*. Pergamon, Amsterdam.

BROSILOW, C. & JOSEPH, B. 2002. *Techniques of Model-Based Control*. Prentice Hall Professional, New Jersey.

BRUNI, S., AMBROSIO, J., CARNICERO, A., CHO, Y. H., FINNER, L., IKEDA, M., KWON, S. Y., MASSAT, J.-P., STICHEL, S., TUR, M. & ZHANG, W. 2015. The results of the pantograph–catenary interaction benchmark. *Vehicle System Dynamics*, 53, 412-435.

BRUNI, S., BUCCA, G., CARNEVALE, M., COLLINA, A. & FACCHINETTI, A. 2018. Pantograph–catenary interaction: Recent achievements and future research challenges. *International Journal of Rail Transportation*, 6, 57-82.

BRUNI, S., BUCCA, G., COLLINA, A., FACCHINETTI, A. & MELZI, S. 2004. Pantograph-catenary dynamic interaction in the medium-high frequency range. Proceedings of the 18th IAVSD Symposium, Kanagawa, Japan, 2003, pp. 697-706.

BRUNI, S., BUCCA, G., COLLINA, A., FACCHINETTI, A. 2012. Numerical and hardware-in-the-loop tools for the design of very high speed pantograph-catenary systems. *Journal of Computational and Nonlinear Dynamics*, 7, 041013.

BSI. 2012. *EN 50367 2012 Railway Applications — Current Collection Systems — Technical Criteria for the Interaction between Pantograph and Overhead Line*. BSI Standards Limited, London.

BSI. 2018. *EN 50318 2018 Railway Applications — Current Collection Systems — Validation of Simulation of the Dynamic Interaction between Pantograph and Overhead Contact Line*. British Standards Institution, London.

BUCCA, G., CARNEVALE, M., COLLINA, A., FACCHINETTI, A., DRUGGE, L., JÖNSSON, P.-A. & STICHEL, S. 2012. Adoption of different pantographs' preloads to improve multiple collection and speed up existing lines. *Vehicle System Dynamics*, 50, 403-418.

BUTCHER, L. 2017. *Rail Electrification* (briefing paper). House of Commons Library, London.

BYRD, R. H., GILBERT, J. C. & NOCEDAL, J. 2000. A trust region method based on interior point techniques for nonlinear programming. *Mathematical Programming*, 89, 149-185.

CAZZANI, A., CATTANI, M., MAURO, R. & STOCHINO, F. 2017. A simplified model for railway catenary wire dynamics. *European Journal of Environmental and Civil Engineering*, 21, 936-959.

CHO, Y. H. 2015. SPOPS statement of methods. *Vehicle System Dynamics*, 53, 329-340.

COLLINA, A. & BRUNI, S. 2002. Numerical simulation of pantograph-overhead equipment interaction. *Vehicle System Dynamics*, 38, 261-291.

COLLINA, A., BRUNI, S., FACCHINETTI, A. & ZUIN, A. 2015. PCaDA statement of methods. *Vehicle System Dynamics*, 53, 347-356.

COLLINA, A., FACCHINETTI, A., FOSSATI, F. & RESTA, F. 2004. Hardware in the loop test-rig for identification and control application on high speed pantographs. *Shock and Vibration*, 11, 445-456.

COLLINA, A., FACCHINETTI, A., FOSSATI, F. & RESTA, F. 2005. An application of active control to the collector of an high-speed pantograph: Simulation and laboratory tests. Proceedings of the 44th IEEE Conference on Decision and Control, 15-15 Dec. 2005, pp. 4602-4609.

CONWAY, S. 2016. *Lump Mass Models for Legacy Pantographs on GB Mainline* (T1105 Report). RSSB, London.

DEML, J., BALDAUF, W. & BAHN, A. D. 2001. A new test bench for examinations of the pantograph-catenary interaction. Proceedings of the World Congress on Railway Research (WCRR) 2001, pp. 25-29.

DIANA, G., FOSSATI, F. & RESTA, F. 1998. High speed railway: Collecting pantographs active control and overhead lines diagnostic solutions. *Vehicle System Dynamics*, 30, 69-84.

DOYLE, J., GLOVER, K., KHARGONEKAR, P. & FRANCIS, B. 1988. State-space solutions to standard H 2 and H∞ control problems. 1988 American Control Conference. IEEE, pp. 1691-1696.

DUAN, H., DIXON, R. & STEWART, E. 2022. A disturbance observer based lumped-mass catenary model for active pantograph design and validation. *Vehicle System Dynamics*, 1-18.

EDWARDS, C. & SPURGEON, S. 1998. *Sliding Mode Control: Theory and Applications*. CRC Press.

ELLIOTT, S. J. & SUTTON, T. J. 1996. Performance of feedforward and feedback systems for active control. *IEEE Transactions on Speech and Audio Processing*, 4, 214-223.

ENFIELD TECHNOLOGIES. 2022. *TR-Electronic-Pressure-Regulator-Datasheet* [Online]. Available: https://www.enfieldtech.com/site/Product-Documentation/TR-Electronic-Pressure-Regulator-Datasheet.pdf [Accessed 07/12/2022].

EPPINGER, S. D., O'CONNOR, D. N., SEERING, W. P. & WORMLEY, D. N. 1988. Modeling and experimental evaluation of asymmetric pantograph dynamics. *Journal of Dynamic Systems, Measurement, and Control*, 110, 168-174.

EVANS, J.R., JOHNSON, T. & CLARK, R.A. 1990. *Dewirement Dynamics - Final Report* (TM-VDY-045). British Rail Research; Source Railway Documentation and Drawing Services Ltd.

FACCHINETTI, A. & MAURI, M. 2009. Hardware-in-the-loop overhead line emulator for active pantograph testing. *IEEE Transactions on Industrial Electronics*, 56, 4071-4078.

FAIVELEY, L. 1960. *Current Collecting Device*. US patent application.

FINNER, L., POETSCH, G., SARNES, B. & KOLBE, M. 2015. Program for catenary–pantograph analysis, PrOSA statement of methods and validation according EN 50318. *Vehicle System Dynamics*, 53, 305-313.

FLIESS, M. & JOIN, C. 2013. Model-free control. *International Journal of Control*, 86, 2228-2252.

FLORES, P., MACHADO, M., SILVA, M. T. & MARTINS, J. M. 2011. On the continuous contact force models for soft materials in multibody dynamics. *Multibody System Dynamics*, 25, 357-375.

FRANKLIN, G. F., POWELL, J. D. & EMAMI-NAEINI, A. 2011. *Feedback Control of Dynamic Systems*. Pearson Education.

FU, Z.-F. & HE, J. 2001. *Modal Analysis*. Elsevier.

GAING, Z.-L. & CHANG, R.-F. 2009. Optimal PID controller for high-speed rail pantograph system with notch filter. TENCON 2009-2009 IEEE Region 10 Conference, IEEE, pp. 1-6.

GEVERS, M., BOMBOIS, X., CODRONS, B. T., SCORLETTI, G. & ANDERSON, B. D. 2003. Model validation for control and controller validation in a prediction error identification framework—Part I: Theory. *Automatica*, 39, 403-415.

GIL, J., GREGORI, S., TUR, M. & FUENMAYOR, F. 2022. Analytical model of the pantograph–catenary dynamic interaction and comparison with numerical simulations. *Vehicle System Dynamics*, 60, 132-155.

GILBERT, G. & DAVIES, H. 1966. Pantograph motion on a nearly uniform railway overhead line. *Proceedings of the Institution of Electrical Engineers*, 113, 485-492.

GINOYA, D., SHENDGE, P. & PHADKE, S. 2013. Sliding mode control for mismatched uncertain systems using an extended disturbance observer. *IEEE Transactions on Industrial Electronics*, 61, 1983-1992.

GLOVER, K. & DOYLE, J. C. 1988. State-space formulae for all stabilizing controllers that satisfy an H∞-norm bound and relations to relations to risk sensitivity. *Systems & Control Letters*, 11, 167-172.

GREGORI, S., GIL, J., TUR, M., TARANCÓN, J. & FUENMAYOR, F. 2020. Analysis of the overlap section in a high-speed railway catenary by means of numerical simulations. *Engineering Structures*, 221, 110963.

GREGORI, S., TUR, M., NADAL, E., AGUADO, J., FUENMAYOR, F. & CHINESTA, F. 2017. Fast simulation of the pantograph–catenary dynamic interaction. *Finite Elements in Analysis and Design*, 129, 1-13.

GREGORI, S., TUR, M., NADAL, E. & FUENMAYOR, F. J. 2018. An approach to geometric optimisation of railway catenaries. *Vehicle System Dynamics*, 56, 1162-1186.

GREGORI, S., TUR, M., PEDROSA, A., TARANCÓN, J. & FUENMAYOR, F. 2019. A modal coordinate catenary model for the real-time simulation of the pantograph-catenary dynamic interaction. *Finite Elements in Analysis and Design*, 162, 1-12.

HAYES, S., FLETCHER, D. I., BEAGLES, A. E. & CHAN, K. 2021. Effect of contact wire gradient on the dynamic performance of the catenary pantograph system. *Vehicle System Dynamics*, 59, 1916-1939.

HOU, Z.-S. & WANG, Z. 2013. From model-based control to data-driven control: Survey, classification and perspective. *Information Sciences*, 235, 3-35.

IKEDA, M. 2015. 'Gasen-do FE' statement of methods. *Vehicle System Dynamics*, 53, 357-369.

ISERMANN, R., SCHAFFNIT, J. & SINSEL, S. 1999. Hardware-in-the-loop simulation for the design and testing of engine-control systems. *Control Engineering Practice,* 7, 643-653.

JÖNSSON, P.-A., STICHEL, S. & NILSSON, C. 2015. CaPaSIM statement of methods. *Vehicle System Dynamics*, 53, 341-346.

KARAKÖSE, E. & GENÇOĞLU, M. T. 2012. Adaptive fuzzy control approach for dynamic pantograph-catenary interaction. Proceedings of 15th International Conference MECHATRONIKA, 5-7 Dec. 2012, pp. 1-5.

KHAN, I., RAJA, M. A. Z., SHOAIB, M., KUMAM, P., ALRABAIAH, H., SHAH, Z. & ISLAM, S. 2020. Design of neural network with Levenberg-Marquardt and Bayesian regularization backpropagation for solving pantograph delay differential equations. *IEEE Access*, 8, 137918-137933.

KIA, S. H., BARTOLINI, F., MPANDA-MABWE, A. & CESCHI, R. 2010. Pantograph-catenary interaction model comparison. IECON 2010 - 36th Annual Conference on IEEE Industrial Electronics Society, 7-10 Nov. 2010, pp. 1584-1589.

KNIGHT, S. 1998. Virgin's first West Coast tilt train 'on test by July 2000'. *Rail*, 345, 6-7.

KO, M. T., YOKOYAMA, M., YAMASHITA, Y., KOBAYASHI, S. & USUDA, T. 2016. Contact force control of an active pantograph for high speed trains. *Journal of Physics: Conference Series*, 744, 012151.

KOBAYASHI, S., STOTEN, D. P., YAMASHITA, Y. & USUDA, T. 2019. Dynamically substructured testing of railway pantograph/catenary systems. *Proceedings of the Institution of Mechanical Engineers, Part F: Journal of Rail and Rapid Transit*, 233, 516-525.

KULKARNI, S., PAPPALARDO, C. M. & SHABANA, A. A. 2017. Pantograph/catenary contact formulations. *Journal of Vibration and Acoustics*, 139, 011010.

KUMANIECKA, A. & PRĄCIK, M. 2003. Modelling and identification of catenary-pantograph system. *Journal of Theoretical and Applied Mechanics*, 41, 887-901.

LEE, J.-H., KIM, Y.-G., PAIK, J.-S. & PARK, T.-W. 2012. Performance evaluation and design optimization using differential evolutionary algorithm of the pantograph for the high-speed train. *Journal of Mechanical Science and Technology*, 26, 3253-3260.

LEVY, S., BAIN, J. A. & LECLERC, E. J. 1968. Railway overhead contact systems, catenary-pantograph dynamics for power collection at high speeds. *Journal of Engineering for Industry*, 90, 692-699.

LI, S., YANG, J., CHEN, W.-H. & CHEN, X. 2011. Generalized extended state observer based control for systems with mismatched uncertainties. *IEEE Transactions on Industrial Electronics*, 59, 4792-4802.

LIN, C.-H. & HSIAO, F.-Y. 2020. Proportional-integral sliding mode control with an application in the balance control of a two-wheel vehicle system. *Applied Sciences*, 10, 5087.

LIN, Y., SHIEH, N. & LIU, V. 2015. Optimal control for rail vehicle pantograph systems with actuator delays. *IET Control Theory & Applications*, 9, 1917-1926.

LIN, Y. C., LIN, C. L. & YANG, C. C. 2007. Robust active vibration control for rail vehicle pantograph. *IEEE Transactions on Vehicular Technology*, 56, 1994-2004.

LIU, L., TIAN, S., XUE, D., ZHANG, T. & CHEN, Y. 2019. Industrial feedforward control technology: A review. *Journal of Intelligent Manufacturing*, 30, 2819-2833.

LOPEZ-GARCIA, O., CARNICERO, A. & MARONO, J. 2007. Influence of stiffness and contact modelling on catenary–pantograph system dynamics. *Journal of Sound and Vibration*, 299, 806-821.

LU, X., LIU, Z., SONG, Y., WANG, H., ZHANG, J. & WANG, Y. 2018. Estimator-based multiobjective robust control strategy for an active pantograph in high-speed railways. *Proceedings of the Institution of Mechanical Engineers, Part F: Journal of Rail and Rapid Transit*, 232, 1064-1077.

LU, X., LIU, Z., ZHANG, J., WANG, H., SONG, Y. & DUAN, F. 2017. Prior-information-based finite-frequency H infinity control for active double pantograph in high-speed railway. *IEEE Transactions on Vehicular Technology*, 66, 8723-8733.

LU, X., ZHANG, H., LIU, Z., DUAN, F., SONG, Y. & WANG, H. 2021. Estimator-based H∞ control considering actuator time delay for active double-pantograph in high-speed railways. *Journal of Low Frequency Noise, Vibration and Active Control*, 40, 442-457.

MAIER, C. C., SCHIRRER, A. & KOZEK, M. 2018. Real-time capable nonlinear pantograph models using local model networks in state-space configuration. *Mechatronics*, 50, 292-302.

MANABE, K. 1992. Catenary-pantograph system for speedup of Shinkansen train. *Japanese Railway Engineering*, 30, 10-13.

MASSAT, J.-P., BALMES, E., BIANCHI, J.-P. & VAN KALSBEEK, G. 2015. OSCAR statement of methods. *Vehicle System Dynamics*, 53, 370-379.

MASSAT, J.-P., LAURENT, C., BIANCHI, J.-P. & BALMÈS, E. 2014. Pantograph catenary dynamic optimisation based on advanced multibody and finite element co-simulation tools. *Vehicle System Dynamics*, 52, 338-354.

MASSAT, J., LAINE, J. & BOBILLOT, A. 2006. Pantograph–catenary dynamics simulation. *Vehicle System Dynamics*, 44, 551-559.

MATHWORKS. 2022. *arx* [Online]. Available: https://uk.mathworks.com/help/ident/ref/arx.html#mw_df3ebcfb-d9ea-43c5-a370-14ff825bf8fd [Accessed 07/12/2022].

MULDER, W. 1996. A comparison between higher-order finite elements and finite differences for solving the wave equation. Proceedings of the Second ECCOMAS Conference on Numerical Methods in Engineering, 1996. John Wiley & Sons, Chichester, pp. 344-350.

NÅVIK, P., RØNNQUIST, A. & STICHEL, S. 2017. Variation in predicting pantograph–catenary interaction contact forces, numerical simulations and field measurements. *Vehicle System Dynamics*, 55, 1265-1282.

NEWMARK, N. M. 1959. A method of computation for structural dynamics. *Journal of the Engineering Mechanics Division*, 85, 67-94.

NISAR, K., SABIR, Z., RAJA, M. A. Z., IBRAHIM, A. A. A., ERDOGAN, F., HAQUE, M. R., RODRIGUES, J. J. P. C. & RAWAT, D. B. 2021. Design of Morlet wavelet neural network for solving a class of singular pantograph nonlinear differential models. *IEEE Access*, 9, 77845-77862.

O'CONNOR, D. N., EPPINGER, S. D., SEERING, W. P. & WORMLEY, D. N. 1997. Active control of a high-speed pantograph. *Journal of Dynamic Systems, Measurement, and Control*, 119, 1-4.

ORTEGA, M. & RUBIO, F. 2004. Systematic design of weighting matrices for the H∞ mixed sensitivity problem. *Journal of Process Control*, 14, 89-98.

PAIK, J.-S., PARK, C.-K., KIM, Y.-G. & KIM, K.-H. 2012. A study on the measuring system of contact force of pantograph for the high-speed train. *Journal of Advanced Mechanical Design, Systems, and Manufacturing*, 6, 140-148.

PAPPALARDO, C. M., PATEL, M., TINSLEY, B. & SHABANA, A. A. 2015a. Pantograph/catenary contact force control. ASME 2015 International Design Engineering Technical Conferences and Computers and Information in Engineering Conference. American Society of Mechanical Engineers, V006T10A028.

PAPPALARDO, C. M., PATEL, M. D., TINSLEY, B. & SHABANA, A. A. 2015b. Contact force control in multibody pantograph/catenary systems. *Proceedings of the Institution of Mechanical Engineers, Part K: Journal of Multi-body Dynamics*, 230, 307-328.

PARK, T.-J., HAN, C.-S. & JANG, J.-H. 2003. Dynamic sensitivity analysis for the pantograph of a high-speed rail vehicle. *Journal of Sound and Vibration*, 266, 235-260.

PISANO, A. & USAI, E. 2008. Contact force regulation in wire-actuated pantographs via variable structure control and frequency-domain techniques. *International Journal of Control*, 81, 1747-1762.

POETSCH, G., EVANS, J., MEISINGER, R., KORTÜM, W., BALDAUF, W., VEITL, A. & WALLASCHEK, J. 1997. Pantograph/catenary dynamics and control. *Vehicle System Dynamics*, 28, 159-195.

POMBO, J. & AMBRÓSIO, J. 2012. Influence of pantograph suspension characteristics on the contact quality with the catenary for high speed trains. *Computers & Structures*, 110-111, 32-42.

POMBO, J., AMBRÓSIO, J., PEREIRA, M., RAUTER, F., COLLINA, A. & FACCHINETTI, A. 2009. Influence of the aerodynamic forces on the pantograph–catenary system for high-speed trains. *Vehicle System Dynamics*, 47, 1327-1347.

POMBO, J., ANTUNES, P. & AMBRÓSIO, J. 2012. A study on multiple pantograph operations for high-speed catenary contact. Proceedings of the Eleventh International Conference on Computational Structures Technology, 2012.

RACHID, A. 2011. Pantograph catenary control and observation using the LMI approach. 2011 50th IEEE Conference on Decision and Control and European Control Conference, 12-15 Dec. 2011, pp. 2287-2292.

RAHMAN, F. A. A., KADIR, M. Z. A. A., OSMAN, M. & AMIRULDDIN, U. A. U. 2020. Review of the AC overhead wires, the DC third rail and the DC fourth rail transit lines: Issues and challenges. *IEEE Access*, 8, 213277-213295.

RAIB 2013. *Accident involving a pantograph and the overhead line near Littleport, Cambridgeshire, 5 January 2012*. Rail Accident Investigation Branch.

RAILTECHNOLOGYMAGAZINE. 2016. *Our holy grail is to provide a pantograph that reacts to the environment* [Online]. Cognitive Publishing Ltd. Available: https://www.railtechnologymagazine.com/Rail-Industry-Focus-/our-holy-grail-is-to-provide-a-pantograph-that-reacts-to-the-environment [Accessed 02/03/2023 2023].

RAMALHO, P., ANTUNES, P., AMBRÓSIO, J., MACEDO, A. & PISSARRA, S. 2022. Virtual pantograph-catenary environment for control development based on a co-simulation approach. *Multibody System Dynamics*, 55, 241-265.

RAUTER, F. G., POMBO, J., AMBRÓSIO, J., CHALANSONNET, J., BOBILLOT, A. & PEREIRA, M. S. 2007. Contact model for the pantograph-catenary interaction. *Journal of System Design and Dynamics*, 1, 447-457.

RAWLINGS, J. B., OGUNNAIKE, B. A., EATON, J. W., CACHE & AMERICAN INSTITUTE OF CHEMICAL ENGINEERS. 2002. *Chemical Process Control VI: Assessment and New Directions for Research; Proceedings of the Sixth International Conference on Chemical Process Control, Tucson, Arizona, January 7-12, 2001*. Cache.

RESTA, F., FACCHINETTI, A., COLLINA, A. & BUCCA, G. 2008. On the use of a hardware in the loop set-up for pantograph dynamics evaluation. *Vehicle System Dynamics*, 46, 1039-1052.

RITZBERGER, D., TALIC, E. & SCHIRRER, A. 2015. Efficient simulation of railway pantograph/catenary interaction using pantograph-fixed coordinates. *IFAC-PapersOnLine*, 48, 61-66.

RSSB. 2012. *Railway Technical Strategy 2012*. RSSB, London.

SAFONOV, M. G., LIMEBEER, D. & CHIANG, R. 1989. Simplifying the H∞ theory via loop-shifting, matrix-pencil and descriptor concepts. *International Journal of Control*, 50, 2467-2488.

SÁNCHEZ-REBOLLO, C., CARNICERO, A. & JIMÉNEZ-OCTAVIO, J. R. 2015. CANDY statement of methods. *Vehicle System Dynamics*, 53, 392-401.

SÁNCHEZ-REBOLLO, C., JIMENEZ-OCTAVIO, J. R. & CARNICERO, A. 2013. Active control strategy on a catenary–pantograph validated model. *Vehicle System Dynamics*, 51, 554-569.

SARIYILDIZ, E., MUTLU, R. & ZHANG, C. 2019a. Active disturbance rejection based robust trajectory tracking controller design in state space. *Journal of Dynamic Systems, Measurement, and Control*, 141, 061013.

SARIYILDIZ, E., OBOE, R. & OHNISHI, K. 2019b. Disturbance observer-based robust control and its applications: 35th anniversary overview. *IEEE Transactions on Industrial Electronics*, 67, 2042-2053.

SCHAUB, M. & SIMEON, B. 2001. Pantograph-catenary dynamics: An analysis of models and simulation techniques. *Mathematical and Computer Modelling of Dynamical Systems*, 7, 225-238.

SCHIRRER, A., ASCHAUER, G., TALIC, E., KOZEK, M. & JAKUBEK, S. 2017. Catenary emulation for hardware-in-the-loop pantograph testing with a model predictive energy-conserving control algorithm. *Mechatronics*, 41, 17-28.

SCHRÖDER, K., ECKE, W., KAUTZ, M., WILLETT, S., JENZER, M. & BOSSELMANN, T. 2013. An approach to continuous on-site monitoring of contact forces in current collectors by a fiber optic sensing system. *Optics and Lasers in Engineering*, 51, 172-179.

SCOTT, G. A. & Cook, M. 1996. Extending the limits of pantograph/overhead performance. *In: Better Journey Time -Better Business. IMechE Conference Transactions 1996-8*, vol. 8, pp. 207-218.

SCOTT, P. R. & ROTHMAN, M. 1974. Computer evaluation of overhead equipment for electric railroad traction. *IEEE Transactions on Industry Applications*, IA-10, 573-580.

SEO, J.-H., KIM, S.-W., JUNG, I.-H., PARK, T.-W., MOK, J.-Y., KIM, Y.-G. & CHAI, J.-B. 2006. Dynamic analysis of a pantograph–catenary system using absolute nodal coordinates. *Vehicle System Dynamics*, 44, 615-630.

SEO, J.-H., SUGIYAMA, H. & SHABANA, A. A. 2005. Three-dimensional large deformation analysis of the multibody pantograph/catenary systems. *Nonlinear Dynamics*, 42, 199-215.

SKOGESTAD, S. & POSTLETHWAITE, I. 2005. *Multivariable Feedback Control: Analysis and Design*. John Wiley & Sons.

SONG, Y. & LI, L. 2020. Robust adaptive contact force control of pantograph–catenary system: An accelerated output feedback approach. *IEEE Transactions on Industrial Electronics*, 68, 7391-7399.

SONG, Y., LIU, Z., OUYANG, H., WANG, H. & LU, X. 2017a. Sliding mode control with PD sliding surface for high-speed railway pantograph-catenary contact force under strong stochastic wind field. *Shock and Vibration*, 2017, 4895321.

SONG, Y., LIU, Z., XU, Z. & ZHANG, J. 2019. Developed moving mesh method for high-speed railway pantograph-catenary interaction based on nonlinear finite element procedure. *International Journal of Rail Transportation*, 7, 173-190.

SONG, Y., OUYANG, H., LIU, Z., MEI, G., WANG, H. & LU, X. 2017b. Active control of contact force for high-speed railway pantograph-catenary based on multi-body pantograph model. *Mechanism and Machine Theory*, 115, 35-59.

SONG, Y., RØNNQUIST, A. & NÅVIK, P. 2020. Assessment of the high-frequency response in railway pantograph-catenary interaction based on numerical simulation. *IEEE Transactions on Vehicular Technology*, 69, 10596-10605.

STOTEN, D., YAMAGUCHI, T. & YAMASHITA, Y. 2016. Dynamically substructured system testing for railway vehicle pantographs. *Journal of Physics: Conference Series*, 744, 012204.

SU, K., ZHANG, J., ZHANG, J., YAN, T. & MEI, G. 2022. Optimisation of current collection quality of high-speed pantograph-catenary system using the combination of artificial neural network and genetic algorithm. *Vehicle System Dynamics*, 61, 260-285.

SUNG, H.-K. & HARA, S. 1988. Properties of sensitivity and complementary sensitivity functions in single-input single-output digital control systems. *International Journal of Control*, 48, 2429-2439.

THOMPSON, A. & DAVIS, B. 1990. An active pantograph with shaped frequency response employing linear output feedback control. *Vehicle System Dynamics*, 19, 131-149.

TUR, M., BAEZA, L., FUENMAYOR, F. & GARCÍA, E. 2015. PACDIN statement of methods. *Vehicle System Dynamics*, 53, 402-411.

UIC. 2022. *RAILISA (RAIL Information System and Analyses)*. UIC, Paris.

UIC & IEA. 2017. *Railway Handbook 2017 Energy Consumption and CO2 Emissions*. UIC, Paris.

VO VAN, O., MASSAT, J.-P. & BALMES, E. 2017. Waves, modes and properties with a major impact on dynamic pantograph-catenary interaction. *Journal of Sound and Vibration*, 402, 51-69.

WALTERS, S. 2010. Simulation of fuzzy control applied to a railway pantograph-catenary system. *In:* SETCHI, R., JORDANOV, I., HOWLETT, R. J. & JAIN, L. C. (eds.) *Knowledge-Based and Intelligent Information and Engineering Systems*. Springer Berlin Heidelberg, pp. 322-330.

WANG, J., ZOLOTAS, A. C. & WILSON, D. 2007. Active suspensions: a reduced-order H∞ control design study. 2007 Mediterranean Conference on Control & Automation, 2007. IEEE, pp. 1-7.

WANG, X. 2016. Chapter 1 - Analysis of a single degree of freedom spring-mass-dashpot system using transfer function, integration, state space, and frequency response methods. *In:* WANG, X. (ed.) *Frequency Analysis of Vibration Energy Harvesting Systems*. Academic Press.

WEI, W., ZHIDONG, Y. & TING, G. 2013. The development of pantograph-catenary dynamics testing rig for high-speed railway. Proceedings of the 2013 International Conference on Mechatronic Sciences, Electric Engineering and Computer (MEC), 2013. IEEE, pp. 3535-3539.

WIBERG, D. M. 1971. *Theory and Problems of State Space and Linear Systems*. McGraw-Hill, New York.

WU, T. X. & BRENNAN, M. J. 1997. Active vibration control of a railway pantograph. *Proceedings of the Institution of Mechanical Engineers, Part F: Journal of Rail and Rapid Transit*, 211, 117-130.

XIN, T. 2019. *Non-Invasive Dynamic Condition Assessment Techniques for Railway Pantographs*. PhD thesis, University of Birmingham.

XIN, T., ROBERTS, C., WESTON, P. & STEWART, E. 2020. Condition monitoring of railway pantographs to achieve fault detection and fault diagnosis. *Proceedings of the Institution of Mechanical Engineers, Part F: Journal of Rail and Rapid Transit*, 234, 289-300.

YANG, J., CHEN, W.-H. & LI, S. 2011. Non-linear disturbance observer-based robust control for systems with mismatched disturbances/uncertainties. *IET Control Theory & Applications*, 5, 2053-2062.

YANG, J., LI, S. & YU, X. 2012. Sliding-mode control for systems with mismatched uncertainties via a disturbance observer. *IEEE Transactions on Industrial Electronics*, 60, 160-169.

YANG, J., PIAO, M., FANG, J., GAO, W., WU, R. & JIA, L. 2017. Dual coupling investigations of wheel-rail and pantograph-catenary for 400 KMH rolling stock. *In:* SPIRYAGIN, M., GORDON, T., COLE, C. & MCSWEENEY, T. (eds.) *The Dynamics of Vehicles on Roads and Tracks Vol 2*. CRC Press.

ZDZIEBKO, P., MARTOWICZ, A. & UHL, T. 2019. An investigation on the active control strategy for a high-speed pantograph using co-simulations. *Proceedings of the Institution of Mechanical Engineers, Part I: Journal of Systems and Control Engineering*, 233, 370-383.

ZEBIRI, H., MOURLLION, B. & BASSET, M. 2014. H∞-controller order reduction for active suspension system. 2014 European Control Conference (ECC), 2014. IEEE, pp. 2364-2369.

ZHANG, J., LIU, W. & ZHANG, Z. 2019a. Sensitivity analysis and research on optimisation methods of design parameters of high-speed railway catenary. *IET Electrical Systems in Transportation*, 9, 150-156.

ZHANG, J., ZHANG, H., SONG, B., XIE, S. & LIU, Z. 2019b. A new active control strategy for pantograph in high-speed electrified railways based on multi-objective robust control. *IEEE Access*, 7, 173719-173730.

ZHANG, W., LIU, Y. & MEI, G. 2006. Evaluation of the coupled dynamical response of a pantograph—catenary system: Contact force and stresses. *Vehicle System Dynamics*, 44, 645-658.

ZHANG, W., MEI, G., WU, X. & SHEN, Z. 2002. Hybrid simulation of dynamics for the pantograph-catenary system. *Vehicle System Dynamics*, 38, 393-414.

ZHONG, Y.-S. 2002. Robust output tracking control of SISO plants with multiple operating points and with parametric and unstructured uncertainties. *International Journal of Control*, 75, 219-241.

ZHOU, N., ZHANG, W.-H. & LI, R.-P. 2011. Dynamic performance of a pantograph-catenary system with the consideration of the appearance characteristics of contact surfaces. *Journal of Zhejiang University-SCIENCE A*, 12, 913-920.

ZHOU, N. & ZHANG, W. 2011. Investigation on dynamic performance and parameter optimization design of pantograph and catenary system. *Finite Elements in Analysis and Design*, 47, 288-295.

ZHU, B., REN, Z., XIE, W., GUO, F. & XIA, X. 2019. Active nonlinear partial-state feedback control of contacting force for a pantograph–catenary system. *ISA Transactions*, 91, 78-89.

ZIEGLER, J. G. & NICHOLS, N. B. 1942. Optimum settings for automatic controllers. *Transactions of the ASME*, 64, 759-765.

APPENDIX A THE FINITE ELEMENT MODELLING PROCEDURE FOR THE CATENARY WIRES

As described in Chapter 3.3.1, a wire in a catenary is subjected to tension, bending moment, damping and external force, as expressed in Eqn. A. 1. The dynamic behaviour of the wire can be written in the Lagrange equation as shown in Eqn. A. 2.

$$F_{joint} = F_{tensile} - F_{bending} - F_{damping} + F_{external} \tag{A. 1}$$

$$\rho A \frac{d^2w}{dt^2} = T \frac{d^2w}{dx^2} - EI \frac{d^4w}{dx^4} - c \frac{dw}{dt} + F(x,t) \tag{A. 2}$$

With boundary conditions, as shown in Figure A.1, the deflection of any position between Nodes 1 and 2 along a beam can be approximately represented by a cubic polynomial as Eqn. A. 3.

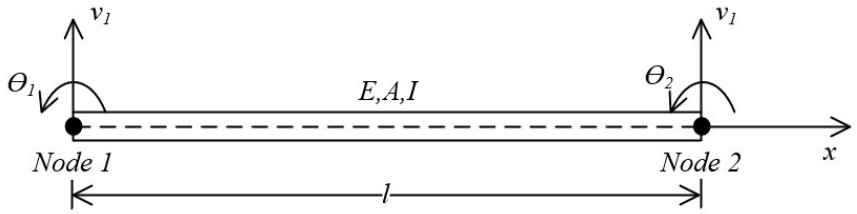


Figure A.1. Euler–Bernoulli beam element

$$w(x) = a_1 + a_2 x + a_3 x^2 + a_4 x^3 \tag{A. 3}$$

where

$$w(x=0) = v_1;\ w(x=l) = v_2;\ \dot{w}(x=0) = \theta_1;\ \dot{w}(x=l) = \theta_2$$

The deflection function can be calculated based on the boundary conditions (at Nodes 1 and 2). The function is the inner product of the so-called shape function and the node displacements.

$$w(x) = N * q^e \tag{A.4}$$

where

$$N = [1 - 3\delta^2 + 2\delta^3 \quad l(\delta - 2\delta^2 + \delta^3) \quad 3\delta^2 - 2\delta^3 \quad l(\delta^3 - \delta^2)]$$

$$\delta = \frac{x}{l}; q^e = [v_1 \quad \theta_1 \quad v_2 \quad \theta_2]^T$$

Therefore, this point's curvature can be obtained from the second derivative of the deflection function.

$$\frac{d^2w}{dx^2} = B(\delta) * q^e \tag{A.5}$$

where

$$B(\delta) = [\frac{1}{l^2}(12\delta - 6) \quad \frac{1}{l}(6\delta - 4) \quad -\frac{1}{l^2}(12\delta - 6) \quad \frac{1}{l}(6\delta - 2)]$$

Combining Eqns. A.2 to A.5, the tensile force on each node of a discretised beam can be obtained through the angle displacement.

$$F_{tensile} = T * \frac{1}{2}\int_0^l \frac{d^2w}{dx^2}dx = T * \frac{1}{2} * \begin{bmatrix} 0 & -1 & 0 & 1 \\ 0 & 0 & 0 & 0 \\ 0 & -1 & 0 & -1 \\ 0 & 0 & 0 & 0 \end{bmatrix} * q^e = \boldsymbol{T^e} * q^e \tag{A.6}$$

The strain energy of a bending beam follows Eqn. A.7, where σ is stress, ε is strain, V is volume, E is Young's modulus and I is seco nd moment of area. With the help of the strain

energy equation, the stiffness matrix can be obtained, based on which the force from a flexural beam against the bending moment can be calculated.

$$E_p = \int \frac{1}{2}\sigma\varepsilon dV = \int \frac{1}{2}E\varepsilon^2 dV = \frac{EI}{2}\int_0^l \left(\frac{d^2w}{dx^2}\right)^2 dx = \frac{1}{2}q^{eT}\boldsymbol{K^e}q^e \tag{A.7}$$

$$\boldsymbol{K^e} = EI\int_0^l B^T B\, dx = \frac{EI}{l^3}\begin{bmatrix} 12 & 6l & -12 & 6l \\ 6l & 4l^2 & -6l & 2l^2 \\ -12 & -6l & 12 & -6l \\ 6l & 2l^2 & -6l & 4l^2 \end{bmatrix} \tag{A.8}$$

$$F_{bending} = \boldsymbol{K^e} * q^e \tag{A.9}$$

Similarly, with the help of the kinetic energy equation, the mass matrix can be found as follows.

$$E_k = \frac{1}{2}m\dot{w}(x) = \frac{1}{2}\dot{q^e}^T\boldsymbol{M^e}\dot{q^e} \tag{A.10}$$

$$\boldsymbol{M^e} = \rho A\int_0^l N^T N\, dx = \frac{\rho Al}{420}\begin{bmatrix} 156 & 22l & 54 & -13l \\ 22l & 4l^2 & 13l & -3l^2 \\ 54 & 13l & 156 & -22l \\ -13l & -3l^2 & -22l & 4l^2 \end{bmatrix} \tag{A.11}$$

$$F_{joint} = \boldsymbol{M^e} * \ddot{q^e} \tag{A.12}$$

The wire's damping is modelled as Rayleigh damping, as shown in Eqn. A.13, which is a linear combination of element mass and stiffness, widely used for catenary wire modelling (Bruni et al., 2015). The damping matrix C^e is represented by Eqn. A.14, where α and β are the constants of proportionality.

$$\boldsymbol{C^e} = \alpha * \boldsymbol{M^e} + \beta * \boldsymbol{K^e} \tag{A.13}$$

$$F_{damping} = \boldsymbol{C^e} * \dot{q^e} \tag{A.14}$$

Now, all the terms, except the external force, in Eqn. A. 1 can be represented by the displacement of nodes. Combining Eqns. A. 1, A. 6, A. 9, A. 12 and A. 14, the dynamic equation of tensioned beams based on FEM can be found, which can be used to solve for the system's equilibrium states. $\boldsymbol{M^e}$, $\boldsymbol{C^e}$ and $\boldsymbol{K^e}$ are defined as the mass, damper and stiffness matrices for the FE model, respectively; F^e denotes the imposed external force.

$$\boldsymbol{M^e} * \ddot{q}^e + \boldsymbol{C^e} * \dot{q}^e + \boldsymbol{K^e} * q^e = F^e \tag{A. 15}$$

where

$$\boldsymbol{M^e} = \boldsymbol{M^e}, \boldsymbol{C^e} = \boldsymbol{C^e}, \boldsymbol{K^e} = \boldsymbol{K^e} - \boldsymbol{T^e}$$

APPENDIX B ANALYSIS OF PANTOGRAPH–CATENARY SIMULATION PARAMETERS

Some simulation parameters need to be defined before conducting the validation and it is also worthwhile discussing their impacts on the numerical results. In this section, the impact of FE meshing size, steady arm stiffness, simulation step size and the number of simulated and measured spans will be analysed.

Note that the analysis in the simulation that follows is all based on the single-pantograph operational case.

B.1 FE meshing size

Meshing size is one of the most critical parameters in FE modelling. A small meshing size can improve the modelling accuracy but this will result in a big number for the degrees of freedom and thus considerable computational time. Therefore, there is a trade-off between modelling accuracy and complexity.

In FE catenary modelling, meshing size also relates to another issue, the geometry of the catenary. The meshing of the wires should be small enough in order to integrate with the droppers at the right locations. For example, for the modelled pre-sag catenary geometry, the droppers are distributed at 4.5, 10.25, 16, 21.75, 27.5, 33.25, 39, 44.75 and 50.5 m from the masts along a span. The lowest common denominator of these numbers is 0.25, so the maximum fixed meshing size is 0.25 m. It is worthwhile mentioneing that besides the commonly used fixed meshing, a variable meshing method (Song et al., 2019) is proposed to improve the simulation efficiency.

The impact of the fixed meshing size on the contact force indicators is presented in Figure B.1.1 and Table B.1.1. It can be seen that compared to a meshing size of 0.25 m, the effect of a smaller mesh on the results is visible but small. Considering the doubled degrees of freedom and quadrupled computational cost, the advantage in accuracy is negligible. Therefore, a meshing size of 0.25 m is chosen for the simulation.

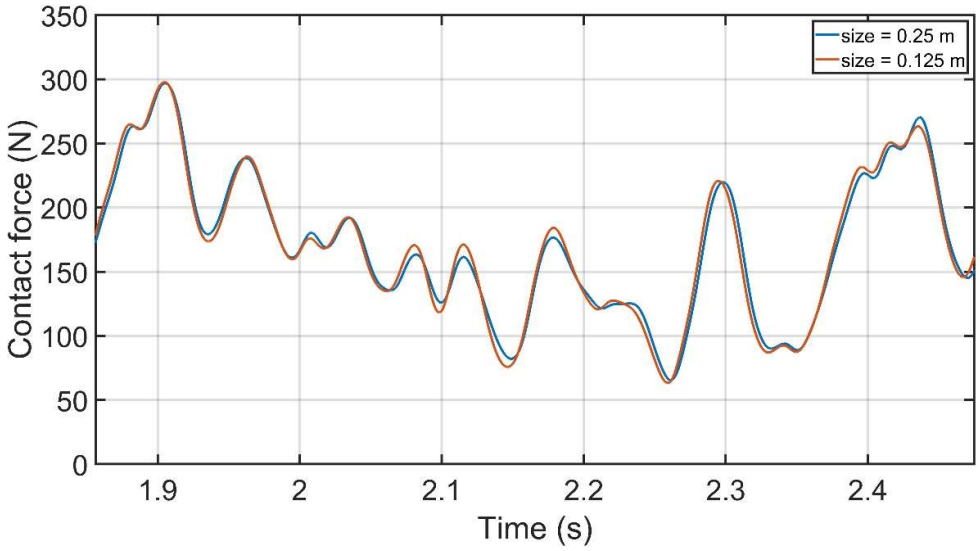


Figure B.1.1. Contact force results with the two meshing sizes

Table B.1.1. Numerical results with the two meshing sizes

Contact force result	Mesh size (m)	
	0.25	0.125
Mean (N)	168.4968	168.4909
Standard deviation (N)	53.9239	54.9238
Maximum (N)	326.3204	326.2461
Minimum (N)	65.4614	63.2868

B.2 Steady arm stiffness

The steady arm is the most significant modelling simplification in this thesis compared to the reference model. The rod-like steady arm is represented as a spring in the modelling, and the stiffness coefficient can be found based on experience or trial and error in the simulation. One approach to estimating the stiffness is comparing the static stiffness of the model with the referenced result. If the steady arm is approximately modelled, the static results (including stiffness and dropper length), not only at the mast position but also along a span, should meet the accuracy requirement.

Three values (200, 300 and 400 N/m) of the coefficient of the steady arm stiffness are simulated and analysed. In the static analysis, the 300 N/m model exhibits static stiffness of 4830.92 N/m, which is the closest result to the referenced value of 4854.37 N/m (BSI, 2018). As shown in Figure B.2.1, the two other steady arm values have noticeable effects on the static stiffness result at the steady arm position. The numerical effect is approximately equivalent to the difference in the coefficient of the steady arm stiffness.

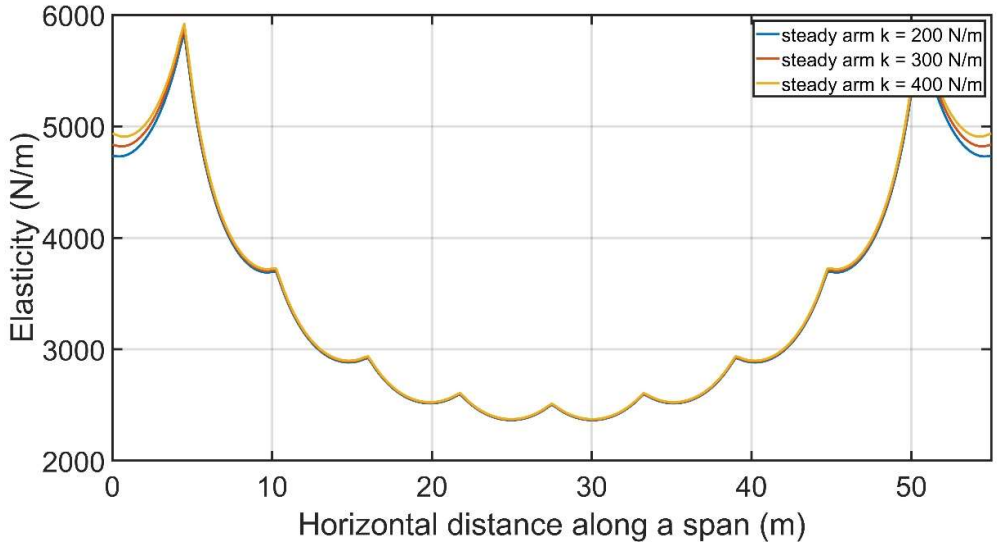


Figure B.2.1. Static stiffness results with the three steady arm stiffnesses

In the dynamic simulation, the time history and numerical results are presented in Figure B.2.2 (zoomed in for only one span). The numerical contact force results for the whole measured span are compared in Table B.2.1. It can be seen that the steady arm stiffness has a minor impact on the contact force results in the single-pantograph case, which might be due to the steady arm being mainly responsible for wave reflection and absorption, and it is not critical in the dynamic result in the single-pantograph case. In any case, the value of 300 N/m will be chosen for the steady arm stiffness as it can meet the standard result with the required accuracy.

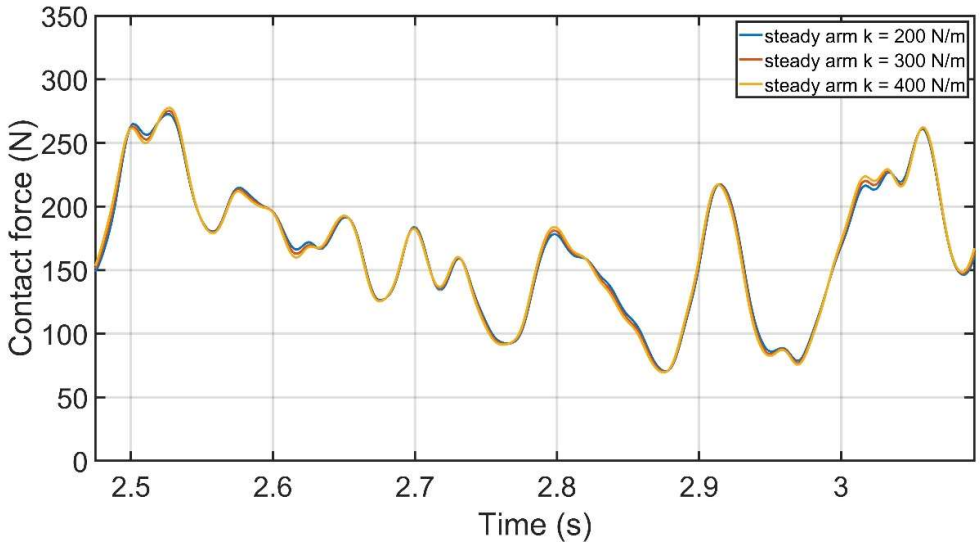


Figure B.2.2. Contact force results with the three steady arm stiffnesses

Table B.2.1. Numerical results with the three steady arm stiffnesses

Contact force result	Steady arm stiffness (N/m)		
	200	300	400
Mean (N)	168.1076	168.1223	168.1295
Standard deviation (N)	55.9915	56.2687	56.5462
Minimum (N)	42.8061	43.7494	44.7908
Maximum (N)	331.7534	326.2222	323.0506

B.3 Simulation step size

The simulation step size is related to the accuracy of the time integration of the pantograph and catenary models. Generally, a small step size makes the simulation more accurate, but the computational time has to be increased. Three values (0.0001, 0.0005 and 0.001 s) of step size are chosen to be simulated and analysed. The 0.0001 s step size is regarded as a superfast step size rate, whose result is considered as the accurate one. The contact force time histories with the three step size values are compared in Figure B.3.1 (zoomed in for only one span) and the numerical contact force results for the whole measured span are compared in Table B.3.1.

It can be seen that the contact force result is changed with the increase of step size. This error is not only visible in the contact force time history but also reflected in the metrics of the results. Although a smaller step size can generate more accurate results, a reasonable step size value is beneficial considering the time consumed for the simulation. Comparing the step size of 0.0005 s with 0.0001 s, the discrepancy in results is negligible, but the time consumed for the simulation is reduced by five times. Therefore, the step size of 0.0005 s will be chosen.

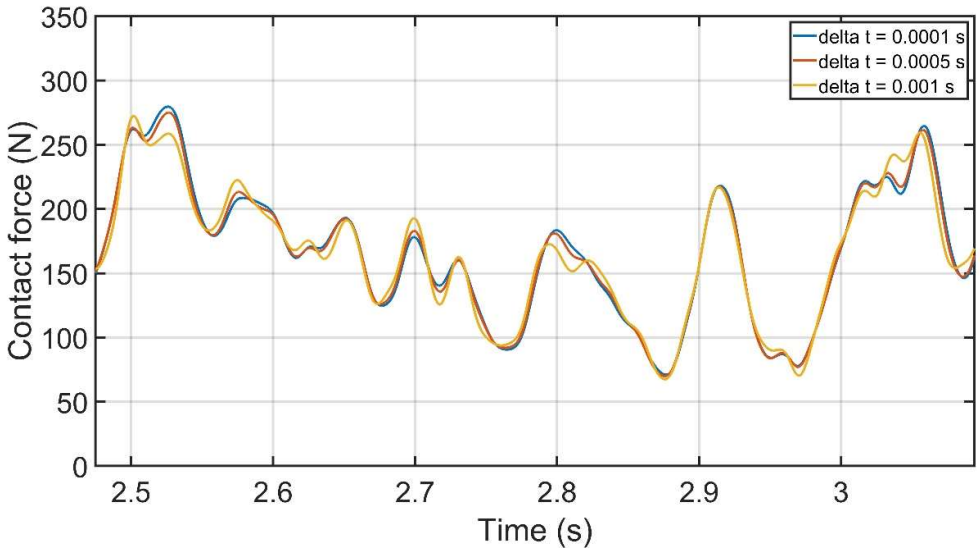


Figure B.3.1. Contact force results with the three simulation step sizes

Table B.3.1. Numerical results with the three simulation step sizes

Contact force result	Simulation step size (s)		
	0.0001	0.0005	0.001
Mean (N)	168.2811	168.1223	167.7891
Standard deviation (N)	56.6486	56.2687	55.7961
Minimum (N)	42.2223	43.7494	50.5267
Maximum (N)	324.7784	326.2222	346.8040

B.4 Number of simulated spans and measured spans

Although it is advised that the measured section should be at least 10 spans long (BSI, 2018), due to the limited RAM capacity of the PC, the simulated and measured section is constrained. In this thesis, a 10-span catenary structure is used for the simulation, which creates 8800 degrees of freedom (with an FE length of 0.25 m). The model ensures a reasonable computational time, but consequently reduces the measurable section in the middle spans.

To reduce the end effect of the catenary structure and the settling effect of the pantograph, the middle seven spans are measured for the numerical results in the single-pantograph case, and the middle three spans are measured in the double-pantograph case additionally considering the effect of wave propagation.

To analyse the effect of the simulated spans, catenary models with 8 and 12 spans are simulated (the single-pantograph case will be discussed here only). The contact force time history signals of the simulations are presented in Figure B.4.1. Since the three signals overlap most of the time in the graph, it is worthwhile pointing out that the signal of the 8-span case ends at t = 3.71 s and the signal of the 10-span case ends at t = 4.95 s. Only at areas close to the above two time points, simulations with a relatively small number of total spans produce slightly different results. This is because, for a shorter catenary structure, the simulation near the last span starts to be affected by wire wave reflection. Therefore, the chosen number of spans should depend on how many spans are supposed to be analysed and measured for the numerical metrics.

The numerical results for the three simulations all measured from the start of the 3rd span until the start of their last span (to avoid the reflection sections) are compared in Table B.4.1. When the model has 10 spans, the simulation results are very similar to those with 12 spans. Due to the transient effect, which will be discussed later, the simulation with 8 spans has a clear difference in the minimum value compared to the 12-span result. However, all results are consistent with the benchmark study. It can be concluded that even without the measurement of a total of 10 spans, the current framework (measuring 7 spans) and results can still be used for validation and further analysis.

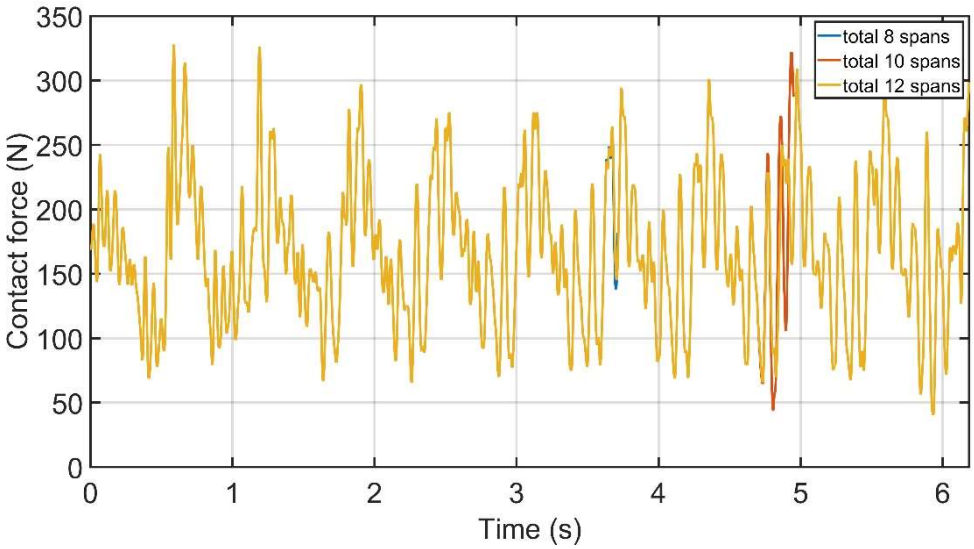


Figure B.4.1. Contact force results with 8-, 10- and 12-span cases

Table B.4.1. Contact force results with 8-, 10- and 12-span cases

Contact force result	Number of spans		
	8	10	12
Mean (N)	167.8354	168.1223	167.8618
Standard deviation (N)	53.5822	56.2687	55.9977
Minimum (N)	65.4673	43.7494	40.3248
Maximum (N)	326.2588	326.2222	326.1978

Another point worth discussing is whether it is reasonable to measure from the start of the 3rd span, considering the fact that in the first few spans of the simulation, the wires are not well excited by the wave propagation. As the catenary is lightly damped, the wire vibration ahead of a train might be important to the pantograph–catenary interaction behaviour. To analyse the impact of the excited vibration, the contact force results are measured for the spans after the

pantograph has reached the 3rd span and 7th span (which is believed to be reliable, as analysed in the later paragraph).

Table B.4.2. Contact force results measured from 3rd and 7th span cases

Contact force result measurement	From 3rd span	From 7th span
Mean (N)	168.1223	168.5225
Standard deviation (N)	56.2687	59.9488
Minimum (N)	43.7494	43.7494
Maximum (N)	326.2222	322.0850

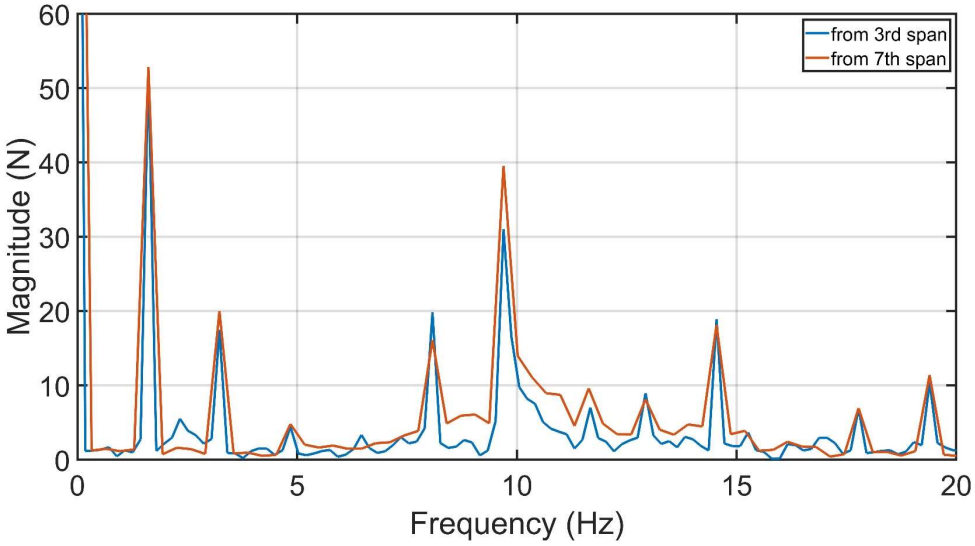


Figure B.4.2. Contact force results measured from 3rd and 7th span cases (spectrum)

Table B.4.2 indicates that overall, there is no such significant difference between from 3rd and 7th span results (both of them meet the reference range). One can observe in Table B.4.2 and Figure B.4.2 that passing more spans before measurement will result in higher contact force fluctuations, specifically around 10 Hz. It is true that before the vehicle passes the measurement point, more waves transmitted to the catenary can cause more fluctuated behaviour. The small

differences are further insignificant in terms of the relative performance of the different pantograph solutions. For the use of comparing different active and passive pantograph performance, the comparison is like for like.

It is believed that the from 7th span result is reliable from the perspective of the wave propagation/vibration by comparing the steady arm uplift time history with the benchmark study. The steady arm displacement after a 5-span excitation (i.e., from the start of the 2nd span to the end of the 6th span) is compared with those that are 'fully' excited in Figure B.4.2. In the figure, the train passes by the steady arm at t = 3.09 s; the vibrations of the steady arm when the train is approaching and leaving show a good agreement between the simulation from the thesis (black line) and other research codes (colourful lines). It is shown that from 7th span, the steady arm (wire) is well excited, and thus the measurement is reliable.

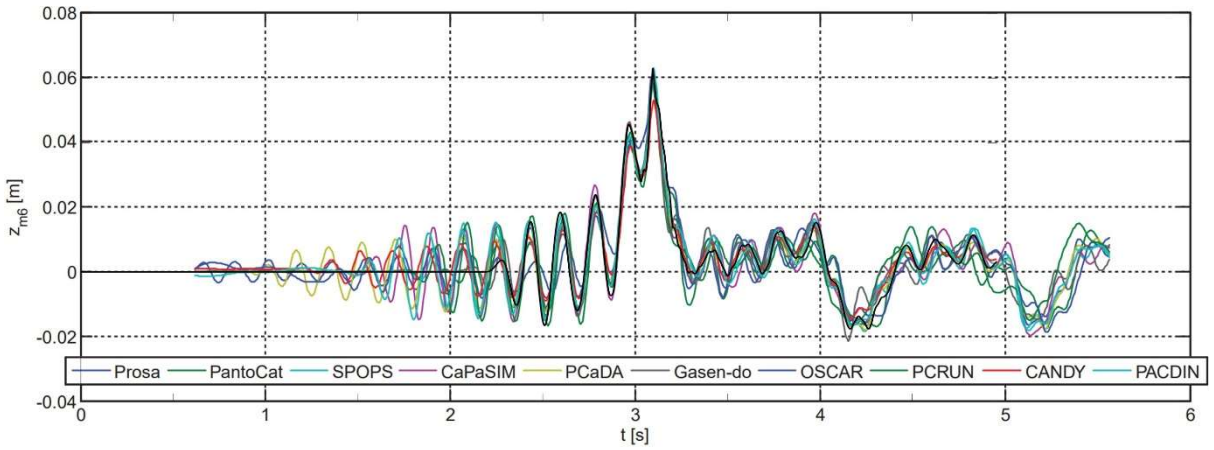


Figure B.4.2. The time history of the uplift of a steady arm

Nevertheless, although the current simulation configuration is acceptable, a more-span catenary system might need to be simulated for higher accuracy or for other research purposes, such as a study on double- or triple-pantograph cases. As it is sometimes difficult to include too many

spans in the simulation in the traditional way, a sliding window method is proposed, which can limit the effective ‘live’ spans in simulation (Kobayashi et al., 2019).

APPENDIX C PUBLISHED PAPERS

Papers that have been published during the course of the PhD study.

1. DUAN, H., DIXON, R. & STEWART, E. 2022. A disturbance observer based lumped-mass catenary model for active pantograph design and validation. Vehicle System Dynamics, 1-18. (The paper mainly covers the content of Chapters 3 and 4)
2. DUAN, H., DIXON, R., STEWART, E. & OLABY, O. Disturbance Observer-Based Sliding Mode Controller for Regulating Pantograph–Catenary Contact Force (accepted by IFAC World Congress 2023) (The paper mainly covers the content of Chapters 5.5)